

# Simulating the Transient Freezing in cooled Non-eutectic Molten Salt Channel Flow

**Master Thesis**

Celeke Bus



# Simulating the Transient Freezing in cooled Non-eutectic Molten Salt Channel Flow

**Master Thesis**

by

Celeke Bus

to obtain the degree of Master of Science  
at the Delft University of Technology,  
to be defended publicly on Friday July 8, 2022 at 11:00 AM.

Student number: 4572173  
Project duration: November 1, 2021 – June 30, 2022  
Thesis committee: dr. ir. M. Rohde, TU Delft, supervisor  
dr. ir. D. Lathouwers, TU Delft  
dr. S.R. de Roode, TU Delft

An electronic version of this thesis is available at <http://repository.tudelft.nl/>.



# Highlights

The most notable contributions of the current research to existing literature are

- *The development of a novel lattice Boltzmann model by adding the source-based enthalpy method, the immersed boundary scheme and the entahlpy-porosity method to a filter-matrix double distribution function*
- *The ability to correctly simulate experimentally and analytically found solutions for transient freezing in laminar convective flow*
- *Tracking the evolution of the mushy layer in cooled non-eutectic laminar flow as function of velocity and temperature*
- *Developing new expressions for the Nusselt number under the presence of a mushy layer*

# Abstract

The fluctuous nature of renewable power generation calls for support of a stable energy supply. Nuclear reactors could meet this demand but fear of major accidents and proliferation often counters its application. A new generation nuclear reactors is developed under the Generation IV International Forum (GIF) of which the molten salt fast reactor (MSFR) is one of the designs. Under stringent safety criteria, all potential risks should be thoroughly examined. This research aims to contribute to a better understanding of one of these potential risks: molten salt freezing in the piping system. To this end, the transient development of salt augmentation under convective flow is modeled to find the effect of freezing on thermal flow properties.

A double distribution filter-matrix lattice Boltzmann (DDF FMLB) fluid dynamics model is combined with the source-based enthalpy method to simulate freezing under convection. Adaptive grid refinement techniques are implemented to track the frozen layer both accurately and efficiently. The immersed boundary scheme and enthalpy porosity method are separately implemented to impose a no-slip condition on the moving phase interface. The model is validated by comparison to two experimental studies on water: cooling by constant heat removal and an isothermal wall. Simulations of the first case can well capture the linearity in measured ice growth. Ice grow rate dependencies on inlet velocity and temperature are similar to the ones found by experiments. The quantitatively found ice grow rates deviate less than 20% from measurements in several flow case studies. During this benchmark study it was found that a maximum lattice Boltzmann velocity of  $u_{\max, \text{LB}} = 0.01$  should be incorporated to maintain stability and that convective boundary conditions can better converge temperature and thus have smaller effect on the rate of solidification. Free convection processes intrinsically present in the experimental set-up could explain discrepancies between the DDF FMLB model and measurements. In the second study, the ice layer profile formed by an isothermally cooled wall is compared to analytically and experimentally found solutions. There is strong agreement between the analytical solution and the lattice Boltzmann simulation (less than 8% deviation). However, these profiles deviated more than 20% from measurements. The discrepancy probably comes from the fact that the experimental set-up cannot fully impose a uniform constant temperature on the boundary. To use this benchmark in the future, it is recommended to test if a convectively cooled boundary better matches the results.

The agreement with the constant heat removal experiment and the analytical solution have proved the performance of the model. An extension to non-eutectic materials is made by introduction of a mushy layer. Thermophysical properties are adjusted and the immersed boundary and enthalpy-porosity method are tested on treatment of the non-Newtonian behaviour present in a mushy layer. Comparison to measurements of heat transfer coefficients in ice slurries gave a first indication that the enthalpy-porosity method might be better suited to describe the slug flow in the mushy region. However, a quantitative comparison of the immersed boundary and enthalpy-porosity scheme to known velocity profiles in non-Newtonian fluids must further confirm this claim. Freezing in laminar salt flow of non-eutectic pseudo-binary system LiF-ThF<sub>4</sub>-UF<sub>4</sub> and eutectic LiF-ThF<sub>4</sub> are simulated under various velocity and temperature conditions. The ice front and mushy layer are found closer to the wall with decreased width for increasing inlet velocity, inlet and wall temperature. A higher pressure drop is found under non-eutectic conditions compared to eutectic freezing. All combined studies led to an estimation of the Nusselt relation as function of ice thickness, showing different dependencies on  $\tilde{x}^{-b}$  in the presence of a mushy layer. The coefficient was found to be  $b = 0.21 \pm 0.05$  for non-eutectic and  $b = 0.32 \pm 0.02$  for eutectic transient freezing. It is recommended that the current study is extended to more flow cases, different types of non-eutectic and eutectic systems and the turbulent regime to get a more grounded and complete picture of the heat transfer properties of molten salts under freezing. It is desired that the found Nusselt relations will be compared to experimental results.

# Nomenclature

$A_{\text{mush}}$	Mushy constant	$\text{kg/m}^3/\text{s}$	<b>Greek symbols</b>	
$B$	weight factor		$\alpha_k^\pm, \beta_k^\pm$	solution vectors
$c_i$	discrete lattice speed		$\alpha$	thermal diffusivity $\text{m}^2/\text{s}$
$C_p$	specific heat	$\text{J/kg/K}$	$\delta$	ice thickness $\text{m}$
$c_s$	speed of sound		$\delta_T$	thermal boundary layer $\text{m}$
$D$	hydraulic diameter	$\text{m}$	$\Delta x, \Delta t$	lattice spatial and time resolution
$E_{ik}, E_{ki}$	filter matrices		$\epsilon$	mushy zone $\text{K}$
$F$	force	$\text{N}$	$\lambda$	thermal conductivity $\text{W/m/K}$
$f_i, g_i$	particle distribution function		$\nu$	kinematic viscosity $\text{m}^2/\text{s}$
$f_l$	liquid fraction		$\Omega$	collision operator
$H$	enthalpy	$\text{J/kg}$	$\rho$	density $\text{kg/m}^3$
$h$	heat transfer coefficient	$\text{W/m}^2/\text{K}$	<b>Subscripts</b>	
$L$	latent heat	$\text{J/kg}$	0	initial
$Nu$	Nusselt number		$b$	boundary
$P$	pressure	$\text{N/m}^2$	$f$	freezing
$Pr$	Prandtl number		$i$	direction in lattice
$q''$	heat flux	$\text{W/m}^2$	$l$	liquid
$Re$	Reynolds number		$m$	mushy
$S_{x,y}$	momentum sink		$s$	solid
$T$	temperature	$\text{K}$	<b>Abbreviations</b>	
$t$	time	$\text{s}$	DDF	double distribution function
$u$	velocity	$\text{m/s}$	FM	filter-matrix
$w_i$	weight coefficient		LBM	lattice Boltzmann method
			MSFR	molten salt fast reactor
			RMSE	root mean squared error
			RRMSE	relative root mean squared error

# Contents

1	Introduction	1
1.1	Molten Salt Fast Reactor	1
1.1.1	Design	2
1.1.2	Freezing risk	3
1.2	Review on existing literature	3
1.2.1	Convective freezing studies	3
1.2.2	Numerical methods	4
1.3	Thesis goals	5
1.3.1	Research questions	5
1.3.2	Outline	5
2	Theory	6
2.1	Fluid Dynamics	6
2.1.1	Continuity equation	6
2.1.2	Momentum equations	6
2.2	Thermodynamics	7
2.2.1	Equation for internal energy	7
2.2.2	Melting and Solidification	7
2.3	Kinetic Theory	9
2.3.1	Boltzmann equation	9
3	Numerical Method	11
3.1	Lattice Boltzmann method	11
3.1.1	Bhatnagar-Gross-Krook operator	12
3.1.2	Multiple-relaxation-time operator	12
3.1.3	Filter-matrix LB method	13
3.2	Thermal Lattice Boltzmann method	13
3.2.1	Double distribution function	14
3.2.2	Modelling Phase Change	14
3.2.3	Phase interface	15
3.3	Boundary conditions	17
3.3.1	Walls	17
3.3.2	In- and outlet	17
3.4	Conversion parameters	18
3.5	Adaptive mesh refinement	19
3.5.1	Refinement	19
3.5.2	Adaptivity	20
3.6	Numerical implementation	20
4	Validation by analytical solutions & experimental results	22
4.1	Validation of model components	22
4.1.1	Forced Convection	22
4.1.2	Stefan Problem	26
4.2	Experimental benchmark cases	27
4.2.1	Grid convergence and energy conservation	27
4.2.2	Constant heat flux	28
4.2.3	Isothermal wall	35

5	Molten salt: Non-eutectic vs. Eutectic	42
5.1	Mushy layer treatment	42
5.2	Effect of mushy layer on thermal flow properties	48
5.2.1	Velocity & temperature dependence	50
5.2.2	Pressure drop	52
5.2.3	Nusselt relation	53
6	Conclusion and Recommendations	57
6.1	Simulation of experimental freezing studies	57
6.2	Effect of mushy layer on thermal flow properties	58
6.3	Recommendations	58
A	Thermophysical dependences	60
A.1	Kinematic viscosity	60
A.1.1	Water	60
A.1.2	Molten salt	60
A.2	Thermal diffusivity	60
A.2.1	Water	60
A.2.2	Molten salt	60
A.3	Thermal conductivity	60
A.3.1	Water	60
A.3.2	Copper	60
A.4	Specific heat	60
A.4.1	Water	60
A.4.2	Carrier liquid 10.6% ethanol	60
A.4.3	Copper	61
B	Figures & Data	62
B.1	Linearity in ice growth under constant heat removal	62
B.2	Mushy zone versus inlet and wall temperature	63
B.3	Nusselt relation for various flow cases	65
B.4	Coefficients that optimise the Nusselt equation fit	66
C	Numerical model	67
	Bibliography	68

# 1

## Introduction

The effect of climate change is noticeable worldwide. Heat waves, rainfall, drought and/or cyclones have become more frequent and intense in every region on earth. In their sixth assessment report, the Intergovernmental Panel on Climate Change (IPCC) stated that human influence is the unequivocal driver of global warming. So far the global surface temperature has risen with 1.1 °C compared to 1850-1900. Unless deep reductions in greenhouse gas emissions occur in the coming decades, temperatures are expected to further increase above the 1.5 °C and 2.0 °C fixed in the Paris agreement [1]. Approximately 75% of these emissions comes from energy use or generation [2]. Driven by population and economic growth, the Energy Information Administration (EIA) expects global energy demand to increase even further with 47% in the next 30 years [3]. The contribution of fossil fuels to this global energy supply should be minimized and replaced by green alternatives. However, rising natural renewable energy sources as solar, wind and hydro power are not yet at their full capacity to cover all energy that is needed. Moreover, their power supply is fluctuous in nature, so advanced and large scale energy storage systems are necessary to stabilize the grid. Even though much research is dedicated to enhance the capacity and lifetime of these storage systems, most technologies are still in their infancy and progress has to be made in terms of cost reduction and efficiency. It is therefore expected that future renewable power generation will still need support of nuclear power plants, as nuclear reactors are stable and low-emitting power sources.

Public fear for major accidents and proliferation often counters the application of nuclear resources. The Generation IV International Forum (GIF) was created to come up with a new generation (Gen IV) nuclear reactors that will use fuel more efficiently, minimise nuclear waste, be economically competitive, and meet stringent standards of safety and proliferation resistance. GIF is a collaboration between 13 countries and the European Union coordinating research on and development of these systems. Six reactor technologies are selected based on their potential to meet the design criteria. One of the selected types of reactor is the molten salt fast reactor (MSFR) [4]. Delft University of Technology (TU Delft) is part of the SAMOSAFER consortium (Severe Accident Modeling and Safety Assessment for Fluid-fuel Energy Reactor), aiming to "develop and demonstrate new safety barriers for more controlled behaviour of MSFRs in severe accidents" [5]. The design of a MSFR is solely conceptual and based on numerical modelling. All potential safety risks should be considered before construction of a new plant is started. This research will focus on developing a new simulation model, validated with experiments, to demonstrate and examine one of the potential safety issues in an MSFR: pipe blockage due to frozen salt augmentation in cold flow channels.

This chapter will give an introduction into MSFR concepts in section 1.1, together with potential safety risks related to freezing. A short overview of recent studies on transient freezing and existing numerical computational fluid dynamic models is given in 1.2. The research questions and the thesis outline are discussed in 1.3.

### 1.1. Molten Salt Fast Reactor

The MSFR design comes from the earlier developed thermal molten salt reactor (MSR), a graphite-moderated liquid-fueled fission reactor where fluid molten salt mixture acts both as fuel and coolant. The potential ad-

vantage over solid-fuel based designs are more practical fuel fabrication and adjustment, better resource utilization, fuel homogeneity and faster heat transfer. By removing the graphite moderator, a fast spectrum MSR is created (MSFR), suitable for thorium-based breeding. Also, cleansing of the molten salt is needed less frequently in MSFRs than in MSRs [6]. These non-moderated reactors are driven by lithium fluoride (LiF) fuel salt, serving as a solvent for fertile thorium fluoride (ThF<sub>4</sub>) and fissile uranium fluoride (UF<sub>4</sub>). Molten salt fluorides remain liquid without pressurization for temperatures typical for MSFRs under operation. This property offers unique and advanced safety features not present in other reactor types: (1) the thermal expansion and Doppler effect ensure a strongly negative reactivity coefficient; and (2) salt from the primary vessel can be drained to emergency tanks underneath the reactor core, connected by a freeze plug which will melt under excessive temperatures [7]. These safety mechanisms ensure passive control during an incident and makes that the MSFR is the prominent research topic of Gen IV reactors in Europe.

### 1.1.1. Design

The reactor design assumed under the SAMOSAFER project has thermal power of 3 GW, operating at a maximum temperature of 1023 K. The 18 m<sup>3</sup> fuel salt is circulated through the core and 16 surrounding heat exchangers in the primary fuel circuit [8]. Heat generated by fission reaction is transferred to the coolant salt in the intermediate circuit and electrical power is eventually generated in the turbine driven energy conversion system. Thick reflectors must protect the core structure and heat exchangers by strongly absorbing the escaping neutron flux. The LiF-based blankets near the edge of the core increase the breeding ratio as concentrated thorium will produce <sup>233</sup>U. During reactor operation fission products are continuously removed from the fuel salt inventory by gas and pyrochemical processing [9].

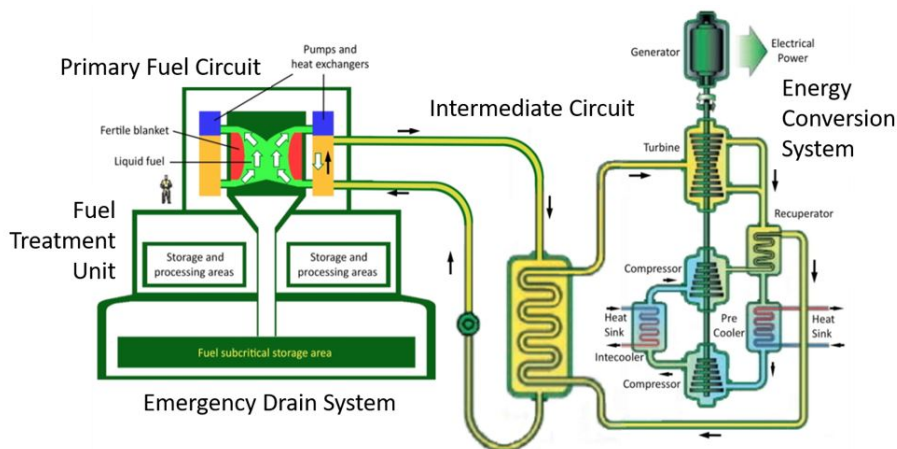


Figure 1.1: Schematic overview of the circuits in the MSFR [5]

The little fuel supply and high desired power density make that the dimensions of the heat exchanger are limited. Preliminary analysis of heat exchanger design is performed in [8]. The design options given are of the order  $D = 1 - 10$  mm per channel. Most metals have a critical velocity above which the protective film is destructed [10] so in order to protect contact materials from erosion the maximum salt velocity of the primary and intermediate loop is limited to  $v = 5$  m/s. The Reynolds number is thus in the range of

$Re_D = 10^2 - 10^5$ . For both the advanced heat exchange designs analysed in [8], the critical Reynolds number which differentiates laminar and turbulent flow is of the order  $10^3$  [11, 12]. This means that inside the heat exchanger the molten fuel salt flow could either be laminar or turbulent. However, this research will only focus on laminar flow conditions.

### 1.1.2. Freezing risk

The beneficial characteristics of salt fluorides come at a potential cost: due to their high melting temperatures they are prone to freezing. Emergency systems in MSFRs are designed on the concept of natural circulation such that decay heat is removed passively with as little as possible need for human intervention and/or power supply. Solidification of salt in the piping system is extremely undesirable for two reasons: (1) it can damage reactor components through volumetric expansion; and (2) it can completely block the flow preventing fluid circulation for cooling [13]. Examples of potential bottle necks are the primary and intermediate heat exchangers and the drainage pipes under the core region. Under normal operation, all temperatures within the MSFR are above the melting temperatures of both the fuel and coolant salts. However, under transient conditions like the start-up or shut-down of the reactor, freezing might be induced. A more dangerous situation would occur in the sudden event of a power outage or depressurisation of the steam generator. In the last case, the lowering of the water boiling point will cause a temperature drop in the intermediate loop which can result in solidification of the coolant salt and clogging of the pipe system. Once frozen, shutting down the energy conversion system is required to remelt the salt in the flow channels [14]. To prevent such undesirable events, correctly modelling and understanding freezing processes is of significant importance to the safety assessment of MSFRs. In the rest of this chapter, literature on transient freezing in cooled channel flow and existing numerical methods to simulate this process will be reviewed.

## 1.2. Review on existing literature

The problem of solidification of liquids inside cold channels finds its application in much more engineering practises than just the MSFR. For that, numbers of studies have been performed to predict the heat transfer rates and frozen profiles under cooled forced convection experimentally, analytically and numerically. This section will give a short overview on existing literature relevant to the present research. A distinction is made between experimental and/or theoretical studies on convective freezing and existing computational fluid dynamics models to predict transient ice formation.

### 1.2.1. Convective freezing studies

The first work on steady-state freezing was performed by Zerkle, Sunderland and Lee [15, 16]. Both experimental and analytical studies were done on steady-state ice formation under the assumption of fully developed laminar flow in a tube or between parallel plates, and uniform wall temperature below the freezing temperature. The investigation aimed at finding temperature and pressure distributions in the presence of solidification at the wall surface. The discrepancy between their experimental and mathematical model came from the negligence of free convection. Multiple follow-up studies were performed under adjusted experimental conditions in order to obtain better results from which more accurate theoretical models could be developed [17, 18, 19].

In these studies no measurements were made on ice thickness and profile. A theoretical model on the transient evolution of the ice interface was developed by Özisik and Mulligan [20] but several simplifying assumptions were needed, restricting the range of applicability. Moreover, they focused on fluid flow in circular tubes rather than through a cooled two dimensional channel, which is the geometry relevant to the current research. Sproston [21] developed a mathematical model to find the steady-state interfaces for a range of boundary conditions other than present in circular tubes. Further research was performed by Kikuchi et al. [22] where ice profiles in laminar flow between cooled parallel plates were found experimentally and compared to analytical solutions. An important contribution to the existing steady-state solutions for ice profiles was done by Weigand and Beer [23] by finding an analytical solution for the transient freezing in laminar flow through parallel plates.

Little experimental research is performed on tracking the ice interface during solidification mainly caused by the difficulty in accurate measuring. One of the few that were able to deliver experimental results on transient freezing were: (1) Savino and Siegel [24] who found the transient growth of a frozen layer formed when convective warm liquid is in contact with one side of a chilled plate; (2) the research of Seki [25] where transient ice transition profiles were found under asymmetric cooling of laminar and turbulent flow between

a parallel plate channel; and (3) Ismail and Padilha [26] who imposed super-cooling on the walls of a parallel plate channel through which water flows laminarily. Temperature and ice thickness were tracked in time. The most recent work of (4) Voulgaropoulos [14] and (5) Kaaks [27] consists of laminar channel flow where walls are cooled by a constant heat flux or an isothermal wall and the resulting ice layer and changing velocity profile are tracked. The last two studies will be discussed more elaborately in the rest of this thesis for their relevance to the current research.

None of the cases above further developed their models to count for ternary systems like molten salts. Tano et al. [28] applied a multi-phase, multi-component phase-field model to simulate the solidification process of coolant salt LiF–KF–NaF (FLiNaK). Where phase-field models are useful in describing microstructures, we are more interested in macrostructures. Moreover, a eutectic process is assumed where molten salts are mostly non-eutectic of nature. A more macroscopic treatment is performed in [29] where the cold filling process of molten salts is studied numerically with a finite volume solver. The non-eutectic nature of molten salts is translated in a mushy constant. A similar method is applied by [30] on laminar tube flow with internal solidification of a binary mixture other than molten salt. This research aims at contributing to the existing literature on freezing of molten salts under laminar flow by developing a new computational model.

### 1.2.2. Numerical methods

The problem of transient freezing has been treated numerically by a range of computational fluid dynamics (CFD) models. Existing CFD models can be subdivided into conventional and particle based solvers. The conventional methods directly solve the governing equations by some sort of approximation whereas particle based solvers follow a more bottom-down approach by micro- or mesoscopic fluid description [31]. Examples of both and their application to transient freezing problems are reviewed here.

#### Conventional solvers

The first conventional method is the finite difference (FD) approach where physical space is divided into a regular mesh and values of the flow field at grid points are calculated by discretising the governing equations. Wei and Güçeri [32] developed an FD model for transient laminar flow freezing in tubes. The downside of such a scheme that comes to light here is that complicated modifications are needed to make the FD method suitable for solving the set of coupled equations underlying the physical problem. Another disadvantage is that FD models are not suitable for complex irregular boundary problems.

A different form of a conventional solver is the finite elements (FE) method. The domain is divided into small finite-sized elements of geometrically simple shapes. Partial differential equations (PDEs) describing the necessary physics are formulated for each element. The functions in each element are of prescribed form and are found by solving the integral form of the PDEs. Kaaks [27] applied the discontinuous Galerkin FE method to freezing in channel flow. The advantage above the FD approach is that complex geometries can easily be handled as the grid is allowed to be unstructured. However, the integral functions can be hard to solve on such grids and simplifications might be necessary, like [33] where the velocity profile is assumed to retain its parabolic profile and is not calculated by the FE model directly.

The last method falling under conventional solvers is the finite volume (FV) model. A simulated volume is divided into smaller volumes which may differ in shape and size. Conservation laws are applied to find flow variables at discrete points within these cells. The FV method has been applied to solidification in laminar tube [34] and channel convection [35], validated by experimental and analytical results respectively. Just as FE models, complex geometries are captured well by the FV approach. Additional to the other conventional solvers, FV models are fundamentally conservative to their control volume formulation. Again, the difficulty of FV implementation comes from the intrinsic complexities of the governing equations. A problem particle based solvers might be able to solve.

#### Lattice Boltzmann method

Typically, microscopic particle-based models are highly impractical for CFD as they follow the motion of individual particles, which is an overly detailed method for calculating macroscopic phenomena. For that, particle based solvers mainly focus on the field of mesoscopic tracking. A method that has received increasing interest over the last two decades is the lattice Boltzmann method (LBM). It treats fluid as ensembles of particles of which the state is defined by local distribution functions. These distribution functions are tracked in space and time. Non-linear terms from the governing equations are defined locally. This property is beneficial for computational performance as parallel computing on advanced computational means like GPUs is possible. Moreover, it makes LBM based models transcend conventional solvers in terms of simplicity.

LBM frameworks have already extended their application to multi-phase thermal flows and are therefore of significant interest in this study. Numerous lattice Boltzmann (LB) studies have been performed on natural convection of melt in a cavity [36, 37], heat transfer in porous media [38, 39] and dendritic crystal growth [40]. However, freezing under forced convection conditions has, to the writer's knowledge, not been simulated yet with the LBM. For a more elaborate review on existing LB models the reader is referred to [41] and [42]. Explanation of existing thermal LB models and ways to include phase change relevant to the present study will be given in chapter 3 together with a justified choice for the model developed in this study.

### 1.3. Thesis goals

This study aims to contribute to a better prediction of the transient freezing of molten salts in the MSFR piping system through a numerical study. The lattice Boltzmann technique is promising in terms of efficiency and simplicity to perform this study. As it is a relatively new CFD solver and it has not been applied to freezing under forced convection, this research will also contribute to the extension of LB model applications and the definition of limiting factors within the chosen model. No numerical study is performed to compare the chosen LB model to other existing LB models as the choice is based on literature recommendation. For that, the focus will first be on finding suitable techniques and boundary conditions to accurately describe freezing under convective flow (methodology). These choices are validated by analytical and experimental results on freezing in water. Hereafter, adjustments are made to make the model suitable for molten salts and to be able to find the influence of various flow conditions on solidified salt layer development and thermal flow properties.

#### 1.3.1. Research questions

1. **Methodology:** *How can the implementation of existing (lattice Boltzmann) techniques best resemble analytical and experimental results for transient freezing of water flowing laminarily through cooled parallel plates?*
  - (a) *What are the limiting factors on input parameters and boundary conditions?*
  - (b) *To what extent can these techniques improve efficiency while maintaining accurate results?*

The validated model will be able to answer the following research questions and their sub-questions.

2. **Solid layer development:** *How and to what extent is the thickness and profile of a solidified salt layer in a laminar molten salt flow through a cooled channel affected by imposed thermal boundary condition and fuel salt inflow properties?*
  - (a) *How will the thickness of the solidified salt layer as a function of location and time depend on different thermal boundary conditions on the wall?*
  - (b) *How will the salt layer evolve for different inlet velocities and inlet temperatures?*
3. **Thermal flow properties:** *How will the augmentation of solidified fuel salt influence the molten salt fast reactor thermal flow properties?*
  - (a) *What will be the effect on the velocity/temperature profile and pressure drop in the fuel salt?*
  - (b) *How will the local Nusselt number depend on salt augmentation? What is the influence of the mushy zone on this relationship?*

#### 1.3.2. Outline

This chapter has given a description of the MSFR design, the need for numerical modelling of transient freezing, a review on existing literature, an introduction on the LBM and the research goals of this study. Chapter 2 will cover the governing equations underlying the physics of phase change in forced convective flow. The choice of lattice Boltzmann model and options for phase change methods to correctly translate the governing equations to a numerical model are explained in Chapter 3. Individual components of the model are validated by comparison to analytical solutions in Chapter 4. The combination of these individual components form the final LB model to simulate transient freezing in laminar convective flow. Its results are discussed and compared to two experimental studies in the same chapter. Modifications to deal with molten salt flow are made and validated in Chapter 5 together with a numerical study on the transient salt augmentation growth to answer the second and third research question. Finally, Chapter 6 will present the conclusions and give recommendations on future research.

# 2

## Theory

The problem of melting and solidification under forced convection is part of the field of fluid- and thermodynamics. This chapter will provide understanding of the fundamental physics underlying such problems. It is divided into two parts, starting with equations governing fluid dynamics in section 2.1, followed by the field of thermodynamics in 2.2. Phase change processes will be discussed in the last, where extra attention is paid to molten salts. As the lattice Boltzmann method has its origin in kinetic theory, 2.3 will describe its basic concepts.

### 2.1. Fluid Dynamics

Fluid dynamics is related to the macroscopic properties of fluid motion. Fluids obey the continuum assumption [43]: at macroscopic scale atomic behaviour can be averaged out so that its properties like density, pressure and velocity are well-defined and continuous everywhere. Assuming continuity, conservation laws for mass and momentum can be derived. The resulting Navier-Stokes equations are given here.

#### 2.1.1. Continuity equation

Considering a fluid element with dimensions much larger than the molecule size and the typical distance between them, we can consider it as macroscopic and its properties as continuous. Mass will flow in- and out this fluid element and without fluid sources or sinks, the fluid mass is conserved. This is valid for all choices of fluid element dimensions, resulting in the continuity equation [44]

$$\frac{\partial \rho}{\partial t} + \nabla \cdot (\rho \mathbf{u}) = 0, \quad (2.1)$$

$\mathbf{u}$  being the fluid velocity and  $\rho$  the density. In case of an incompressible fluid (2.1) reduces to

$$\nabla \cdot \mathbf{u} = 0. \quad (2.2)$$

#### 2.1.2. Momentum equations

Following the analogy given for the continuity equation, also the momentum within a fluid element is conserved. For a simple ideal fluid, changes in momentum come from in- and outflow of momentum, pressure gradients  $\nabla P$  and external forces  $\mathbf{F}$ , forming the Euler equation

$$\frac{\partial(\rho \mathbf{u})}{\partial t} + \nabla \cdot (\rho \mathbf{u} \otimes \mathbf{u}) = -\nabla P + \mathbf{F}. \quad (2.3)$$

The Euler equation does not yet include internal friction which transfers momentum between neighbouring fluid elements. A more general form is the Cauchy momentum equation

$$\frac{\partial(\rho \mathbf{u})}{\partial t} + \nabla \cdot (\rho \mathbf{u} \otimes \mathbf{u}) = \nabla \cdot \boldsymbol{\sigma} + \mathbf{F} \quad (2.4)$$

containing a viscous stress tensor  $\boldsymbol{\sigma} = -P\mathbf{I} + \boldsymbol{\tau}$ . Expressing the shear tensor  $\boldsymbol{\tau}$  as a Newtonian fluid in viscosity  $\nu$  and velocity gradients and assuming constant density (incompressible limit) so that  $\nabla \cdot \mathbf{u} = 0$ , the Cauchy momentum equation reduces to the Navier-Stokes equations [44]

$$\rho \left( \frac{\partial \mathbf{u}}{\partial t} + \nabla \cdot (\mathbf{u} \otimes \mathbf{u}) \right) = -\nabla P + \rho \nabla \cdot (\nu \nabla \mathbf{u}) + \mathbf{F}. \quad (2.5)$$

In general, these equations are difficult to solve and analytical solutions are found only in simple cases. An example of such is the steady-state, body-force driven Poiseuille flow.

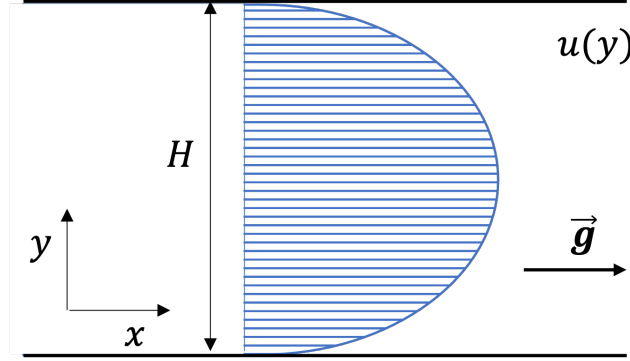


Figure 2.1: Flow profile of Poiseuille flow between two parallel plates with no slip boundary conditions.

As the flow is steady-state, the left-hand side of (2.5) is equal to zero. The body-force  $\mathbf{F} = \rho \mathbf{g}$  is known and no pressure gradient is present. Assuming  $u(0, H) = 0$  on the boundaries, the solution is found analytically as [45]

$$u(y) = -\frac{\mathbf{g}}{2\nu} y(y - H). \quad (2.6)$$

## 2.2. Thermodynamics

Another macroscopic variable that is conserved is total energy, consisting of internal and mechanical energy. Together with the Navier-Stokes equations the equation for internal energy forms a closed set of equations, enabling to solve for density, velocity and temperature. The internal energy equation and its modifications to deal with phase change are given here.

### 2.2.1. Equation for internal energy

As for the continuity and momentum equations, again the internal equation comes from balancing energy in a fluid element. Assuming an incompressible fluid where  $\rho = \text{constant}$  and neglecting viscous dissipation, the so-called heat equation is given as

$$\rho C_p \frac{\partial T}{\partial t} + \rho C_p \mathbf{u} \cdot \nabla T = \rho C_p \nabla \alpha \nabla T + Q \quad (2.7)$$

where  $C_p$ ,  $\alpha$  and  $Q$  are the specific heat, thermal diffusivity and a heat source or sink. Making the replacements

$$\rho \mathbf{u} \rightarrow \rho C_p T, \quad \rho \mathbf{u} \cdot \nabla \mathbf{u} + \nabla P \rightarrow \rho C_p \mathbf{u} \cdot \nabla T, \quad \nu \rightarrow \alpha, \quad \mathbf{F} \rightarrow q \quad (2.8)$$

the analogy with the Navier-Stokes equations is apparent.

### 2.2.2. Melting and Solidification

Phase change processes are defined by a change in enthalpy and it is therefore more convenient to work in terms of enthalpy  $H$  instead of temperature when treating phase change problems. The enthalpy normally consists of internal energy and a work term due to the pressure. In the present study the pressure can be assumed to be approximately constant and change in enthalpy comes only from the internal energy. At molecular level, bonds are either formed or broken during phase change. The energy released or required in this process, is the latent heat. The other term describing the internal energy in enthalpy is the sensible heat, related to change in temperature. For that, the enthalpy is defined as

$$H = C_p T + f_l L \quad (2.9)$$

where  $f_l$  is the volume-liquid fraction and  $L$  the latent heat. The region undergoing phase change is defined as the mushy region, here the liquid fraction lies between 0 and 1. During melting and solidification  $Q$  becomes either a heat sink (solid  $\rightarrow$  liquid) or source (liquid  $\rightarrow$  solid) and is described by the change in enthalpy [46]

$$Q = -\frac{\partial(\rho\Delta H)}{\partial t} = -\frac{\partial(\rho L f_l)}{\partial t} \quad (2.10)$$

for a pure material. The heat equation can now be written in two forms when dealing with phase change. We can either replace  $Q$  directly into (2.7), leading to

$$\frac{\partial T}{\partial t} + \mathbf{u} \cdot \nabla(T) = \nabla(\alpha \nabla T) - \frac{L}{C_p} \frac{\partial f_l}{\partial t}, \quad (2.11)$$

if  $\rho$  is constant. When the source term (2.10) is combined with the transient term  $C_p \partial T / \partial t$  to form the total change in enthalpy  $\partial H / \partial t$ , the heat equation can be rewritten as

$$\frac{\partial(H)}{\partial t} + C_p \mathbf{u} \cdot \nabla T = C_p \nabla \alpha \nabla T. \quad (2.12)$$

The temperature and the liquid fraction follow from the total enthalpy

$$T = \begin{cases} H / C_{p,s} & H < H_s \\ T_s + \frac{H - H_s}{H_l - H_s} (T_l - T_s) & H_s \leq H \leq H_l \\ T_l + (H - H_l) / C_{p,l} & H > H_l \end{cases} \quad (2.13)$$

$$f_l = \begin{cases} 0 & H < H_s \\ \frac{H - H_s}{H_l - H_s} & H_s \leq H \leq H_l \\ 1 & H > H_l \end{cases} \quad (2.14)$$

The phase interface is naturally tracked by updating the liquid fraction. The solidus and liquidus temperatures ( $T_s, T_l$ ) and enthalpies ( $H_s = C_{p,s} T_s, H_l = H_s + C_{p,ref} (T_l - T_s) + L$ ) define the boundaries of the mushy region. For pure or eutectic materials, the change in enthalpy due to solidification or liquidification happens at a single temperature  $T_s = T_l = T_f$ , while for non-eutectic mixtures, it follows a phase trajectory in the mushy zone  $\epsilon = T_l - T_s$ . In the last case, the enthalpy change during phase transition does not only come from latent heat but also partly from sensible heat. A reference specific heat  $C_{p,ref} = \frac{2C_{p,cl}C_{p,s}}{C_{p,cl} + C_{p,s}}$  is introduced to capture the combined solid and liquid effects on this change in sensible heat.

Molten salts are typically non-eutectic mixtures. Special care should be taken in defining physical parameters within the mushy region as two phases are mutually present. The substance might become non-Newtonian here, making the viscosity and thermal diffusivity locally dependent. Examples of such will be discussed in 5.1

Again, only for simple cases an analytical solution can be found. Conduction-induced melting of a pure substance in a semi-infinite space known as the Stefan problem has such an analytical solution. Figure 2.2 gives a schematic overview of this one-dimensional problem. At  $t = 0$  the domain is at a uniform temperature  $T_0$  smaller than the freezing/melting temperature  $T_f = T_m$ . At  $t > 0$  the left wall ( $x = 0$ ) is heated with a temperature  $T_b > T_f$  and the solid will liquify. The right wall is assumed to be far away from the left wall such that temperature change is not felt. To find a solution the velocity should be zero everywhere.

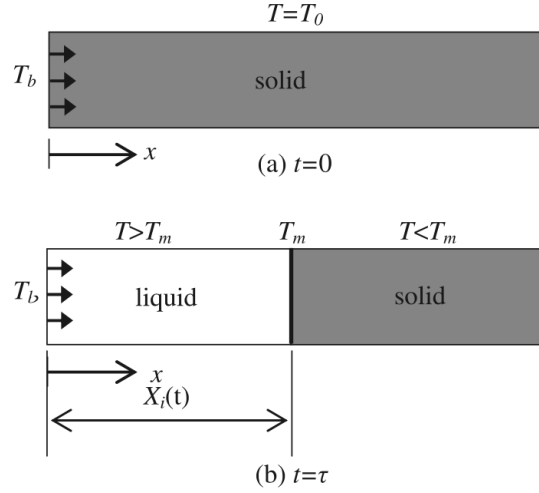


Figure 2.2: Schematic overview of the Stefan problem including the initial and boundary conditions [46].

This problem is defined by its melting front  $X_i(t)$  with temperature  $T_m = T_f$

$$X_i(t) = 2k\sqrt{\alpha t}. \quad (2.15)$$

In some cases it might be necessary to distinguish physical parameters in solid and liquid phase. In that case the analytical solution for the temperature becomes [47]

$$T(x, t) = \begin{cases} T_b - \frac{(T_b - T_m) \operatorname{erf}\left(\frac{x}{2\sqrt{\alpha_l t}}\right)}{\operatorname{erf}(k)} & 0 < x < X_i(t), t > 0 \\ T_0 + \frac{(T_m - T_0) \operatorname{erfc}\left(\frac{x}{2\sqrt{\alpha_s t}}\right)}{\operatorname{erfc}(k\sqrt{\alpha_l/\alpha_s})} & x > X_i(t), t > 0 \end{cases} \quad (2.16)$$

with parameter  $k$

$$\frac{e^{-k^2}}{\operatorname{erf}(k)} + \frac{\lambda_s}{\lambda_l} \left(\frac{\alpha_l}{\alpha_s}\right)^{1/2} \frac{T_m - T_0}{T_m - T_b} \frac{e^{-k^2(\alpha_l/\alpha_s)}}{\operatorname{erfc}(k\sqrt{\alpha_l/\alpha_s})} = \frac{kL\sqrt{\pi}}{C_{p,l}(T_m - T_b)}. \quad (2.17)$$

## 2.3. Kinetic Theory

Kinetic theory is most commonly applied to dilute gases and gives a description on a mesoscopic scale: the distribution of particles is followed rather than the motion of individual particles (microscopic scale) or macroscopic quantities like density, velocity and temperature. The most important variable in kinetic theory is the particle distribution function  $f(\mathbf{x}, \boldsymbol{\xi}, t)$  which is a function of particle position  $\mathbf{x}$ , velocity  $\boldsymbol{\xi}$  and time  $t$ . The distribution function is connected to the macroscopic variables density and velocity through

$$\rho(\mathbf{x}, t) = \int f(\mathbf{x}, \boldsymbol{\xi}, t) d^3 \boldsymbol{\xi} \quad (2.18)$$

and

$$\rho(\mathbf{x}, t) \mathbf{u}(\mathbf{x}, t) = \int \boldsymbol{\xi} f(\mathbf{x}, \boldsymbol{\xi}, t) d^3 \boldsymbol{\xi}. \quad (2.19)$$

When the gas will be left alone for a long time, it can be assumed that  $f(\mathbf{x}, \boldsymbol{\xi}, t)$  converges to an equilibrium  $f^{\text{eq}}(\mathbf{x}, \boldsymbol{\xi}, t)$ .

### 2.3.1. Boltzmann equation

The evolution of the distribution function  $f(\mathbf{x}, \boldsymbol{\xi}, t)$  is given by the Boltzmann equation

$$\frac{\partial f}{\partial t} + \boldsymbol{\xi}_{x,y} \frac{\partial f}{\partial x_{x,y}} + \frac{F_{x,y}}{\rho} \frac{\partial f}{\partial \xi_{x,y}} = \Omega(f). \quad (2.20)$$

The first two terms are related to the particle velocities while the third term consists of forces changing these velocities. The collision operator  $\Omega$  on the right-hand side represents a source term describing the redistribution of  $f$  due to collisions with

$$\Omega(f) = -\frac{1}{\tau} (f - f^{eq}) \quad (2.21)$$

and was invented by and named after Bhatnagar, Gross and Krook (BGK). It shows the convergence towards the equilibrium distribution with a certain relaxation parameter  $\tau$ . The Boltzmann equation can be transformed to the fluid and thermodynamic governing equations by multiplying it with functions of  $\xi$ , integrating over velocity space and applying a technique called the Chapman-Enskog expansion as described in [31]. By doing so it can be shown that the solution to the Boltzmann equation equals the solution of the Navier-Stokes equations (under some conditions). The numerical approach to find the solution to the Boltzmann equation turns out to be quite simple. How the Boltzmann equation and BGK collision operator can be translated to the lattice Boltzmann method will be explained in chapter 3.

# 3

## Numerical Method

The lattice Boltzmann method is used to find solutions to the governing equations given in the previous chapter. There exist multiple LB schemes, of which some will be discussed here. First a decision for the collision operator is made in 3.1. In 3.2 the thermal LB method is introduced together with the adjustments needed to deal with phase change. The boundary treatment is discussed in 3.3. The concrete steps taken to build the final LB model proposed in this chapter are given in the final sections 3.4, 3.5 and 3.6.

### 3.1. Lattice Boltzmann method

Solving the Boltzmann equation numerically gives rise to the discrete-velocity distribution functions  $f_i(\mathbf{x}, t)$ , describing particle distributions with velocity  $\mathbf{c}_i$  at position  $\mathbf{x}$  and time  $t$ . The velocity together with their corresponding weights form the velocity set  $\{\mathbf{c}_i, w_i\}$ , usually denoted by DdQq. Here  $d$  is the dimension number and  $q$  the number of velocities. Subscript  $i$  refers to the direction in which the particle distributions can stream. Figure 3.1 gives the directions in the D2Q9 scheme, the one that will be used throughout this thesis. Each velocity set comes with constant  $c_s$ , relating density to pressure through  $p = c_s^2 \rho$  and therefore represents the model's speed of sound. As with equation (2.18) and (2.19), the macroscopic variables density and momentum can be derived from the particle distribution with

$$\rho(\mathbf{x}, t) = \sum_i f_i(\mathbf{x}, t), \quad \rho \mathbf{u}(\mathbf{x}, t) = \sum_i \mathbf{c}_i f_i(\mathbf{x}, t) \quad (3.1)$$

The particle distributions themselves are found by solving the Boltzmann equation, discretized in velocity, space and time:

$$f_i(\mathbf{x} + \mathbf{c}_i \Delta t, t + \Delta t) = f_i^*(\mathbf{x}, t) + \Omega_i(\mathbf{x}, t). \quad (3.2)$$

Equation (3.2) represents distribution  $f_i(\mathbf{x}, t)$  colliding and streaming to position  $\mathbf{x} + \Delta \mathbf{x}$  in the next time step  $t + \Delta t$ . The operator  $\Omega_i$  models the collision by redistributing particles among  $f_i$  at each node. There are many ways to model the collision operator  $\Omega_i$ . Three of which are discussed in the next sections. The collision-streaming process can best be pictured with Figure 3.1. This process is repeated in each time step. The most common choice for the time step and lattice spacing are lattice units, such that  $\Delta t = 1$  and  $\Delta x = 1$ . These units can be converted to physical units to simulate an equivalent physical system as will be further explained in 3.4.

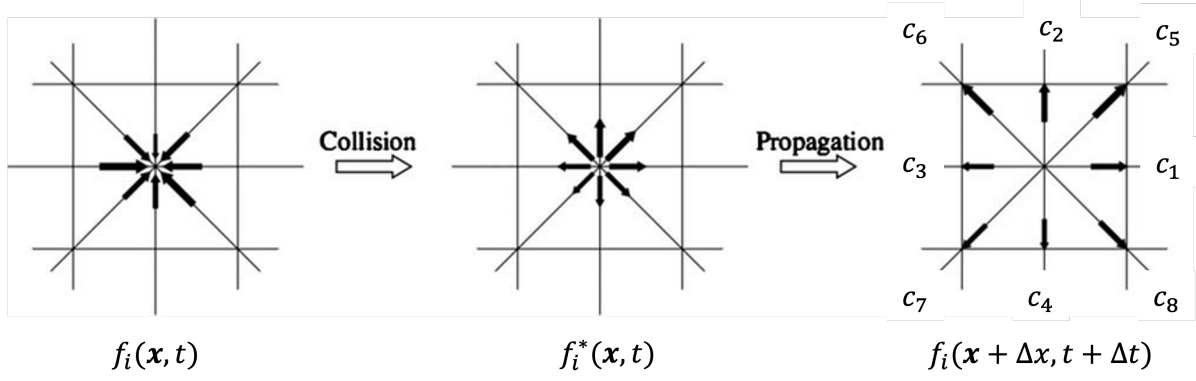


Figure 3.1: Schematic overview of the colliding and streaming process of distributions  $f_i$ .

### 3.1.1. Bhatnagar-Gross-Krook operator

The BGK collision operator was already discussed in 2.3.1. In discretized form it looks like

$$\Omega_i(f) = -\frac{f_i - f_i^{\text{eq}}}{\tau} \Delta t \quad (3.3)$$

with discrete equilibrium distribution

$$f_i^{\text{eq}}(\mathbf{x}, t) = w_i \rho \left( 1 + \frac{\mathbf{u} \cdot \mathbf{c}_i}{c_s^2} + \frac{(\mathbf{u} \cdot \mathbf{c}_i)^2}{2c_s^4} - \frac{\mathbf{u} \cdot \mathbf{u}}{2c_s^2} \right). \quad (3.4)$$

In the D2Q9 set,  $c_s = 1/\sqrt{3}$ . Through the Chapman-Enskog analysis, the relaxation time  $\tau$  is related to the viscosity  $\nu$  with

$$\nu = c_s^2 \left( \tau - \frac{\Delta t}{2} \right) \quad (3.5)$$

This comes with a stability criterion  $\tau/\Delta t > 1/2$  as the viscosity cannot be negative.

The BGK operator is the collision operator in its most simple and efficient form. However, this comes at the cost of stability. For small values of viscosity i.e. large Reynolds numbers  $\tau \rightarrow 0.5$  and the use of the BGK operator is limited. Moreover, the accuracy of simulations depends on  $\tau$ . A problem that can be solved with the multiple-relaxation-time (MRT) collision operator as it incorporates more tunable free parameters to stabilise the solution for  $\tau$  much closer to 0.5 [31].

### 3.1.2. Multiple-relaxation-time operator

The MRT method performs collisions in momentum space. Therefore the particle distributions are mapped to momentum space, collide and are then transformed back to their original space. The mapping is done through matrix multiplication  $\mathbf{m} = \mathbf{M}\mathbf{f}$  resulting in  $q$  moments  $\mathbf{m} = \{m_0, \dots, m_{q-1}\}$  coming from the populations  $\mathbf{f} = \{f_0, \dots, f_{q-1}\}$ . To perform the collision step (3.7), these moments are relaxed with individual rates. The relaxation parameters for the different moments are contained in diagonal matrix  $\mathbf{S}$ .

$$\mathbf{S} = \begin{pmatrix} \frac{1}{\tau_0} & 0 & \dots & 0 \\ 0 & \frac{1}{\tau_1} & \dots & 0 \\ \vdots & \vdots & \ddots & \vdots \\ 0 & 0 & \dots & \frac{1}{\tau_{q-1}} \end{pmatrix} \quad (3.6)$$

$$f_i(\mathbf{x} + \mathbf{c}_i \Delta t, t + \Delta t) = f_i^*(\mathbf{x}, t) - \mathbf{M}^{-1} \mathbf{S} [\mathbf{m}(\mathbf{x}, t) - \mathbf{m}^{\text{eq}}(\mathbf{x}, t)] \Delta t. \quad (3.7)$$

The free parameters should be chosen carefully and only after thorough stability analysis (e.g. Von Neumann analysis) the optimum parameters can be selected. For more complex problems, this becomes fairly cumbersome. Especially when the double distribution method is incorporated (more on that in 3.2.1), choosing the right parameters will be highly impractical and time consuming. A method that keeps the advantages of MRT in terms of accuracy and stability while overcoming the difficulty of selecting appropriate parameters is the filter-matrix lattice Boltzmann scheme (FMLB) and will be used throughout this thesis.

### 3.1.3. Filter-matrix LB method

The FMLB method was first introduced by [48] utilizing a staggered formulation of the collision operator

$$f_i \left( \mathbf{x} + \frac{\mathbf{c}_i \Delta t}{2}, t + \frac{\Delta t}{2} \right) - f_i \left( \mathbf{x} - \frac{\mathbf{c}_i \Delta t}{2}, t - \frac{\Delta t}{2} \right) = \Delta t \Omega_i. \quad (3.8)$$

The solution for the density distribution function is improved by [49] and given as

$$f_i = f_i^{\text{eq}} - \rho w_i \nu \left( \frac{(\mathbf{c}_i \cdot \nabla)(\mathbf{c}_i \cdot \mathbf{u})}{c_s^4} - \frac{\nabla \cdot \mathbf{u}}{c_s^2} \right). \quad (3.9)$$

The equilibrium distribution  $f_i^{\text{eq}}$  is the same as for the BGK method in (3.4). The particle distributions half a time step before and after the collisions are constructed with the matrix multiplication

$$f_i \left( \mathbf{x} \pm \frac{\mathbf{c}_i \Delta t}{2}, t \pm \frac{\Delta t}{2} \right) = \sum_k w_i \mathbf{E}_{ik} \alpha_k^\pm. \quad (3.10)$$

The reverse operation gives the solution vectors  $\alpha_k^\pm$

$$\alpha_k^\pm = \sum_i \mathbf{E}_{ki} f_i \left( \mathbf{x} \pm \frac{\mathbf{c}_i \Delta t}{2}, t \pm \frac{\Delta t}{2} \right). \quad (3.11)$$

In the D2Q9 model the reversible matrices  $w_i \mathbf{E}_{ik} = \mathbf{E}_{ki}^{-1}$  and the solution vectors are given by

$$\mathbf{E}_{ik} = \left[ 1, 3c_{ix}, 3c_{iy}, \frac{3c_{ix}^2 - 1}{2}, 3c_{ix}c_{iy}, \frac{3c_{iy}^2 - 1}{2}, \frac{3c_{ix}(3c_{iy}^2 - 1)}{2}, \frac{3c_{iy}(3c_{ix}^2 - 1)}{2}, \frac{(3c_{ix}^2 - 1)(3c_{iy}^2 - 1)}{2} \right], \quad (3.12)$$

$$\mathbf{E}_{ki} = \left[ 1, c_{ix}, c_{iy}, 3c_{ix}^2 - 1, 3c_{ix}c_{iy}, 3c_{iy}^2 - 1, c_{ix}(3c_{iy}^2 - 1), c_{iy}(3c_{ix}^2 - 1), \frac{(3c_{ix}^2 - 1)(3c_{iy}^2 - 1)}{2} \right]^T \quad (3.13)$$

and

$$\alpha_k^\pm = \begin{bmatrix} \rho \\ \rho u_x \pm \frac{\Delta t}{2} f_x \\ \rho u_y \pm \frac{\Delta t}{2} f_y \\ 3\rho u_x u_x + \rho(-6\nu \pm \Delta t) \frac{\partial u_x}{\partial x} \\ 3\rho u_x u_y + \frac{\rho(-6\nu \pm \Delta t)}{2} \left( \frac{\partial u_x}{\partial y} + \frac{\partial u_y}{\partial x} \right) \\ 3\rho u_y u_y + \rho(-6\nu \pm \Delta t) \frac{\partial u_y}{\partial y} \\ T_1^\pm \\ T_2^\pm \\ F^\pm \end{bmatrix}. \quad (3.14)$$

The third and fourth order terms  $T_1^\pm, T_2^\pm, F^\pm$  are generally small and can be set to 0. The numerical implementation of the filter-matrix method will be discussed in 3.6.

## 3.2. Thermal Lattice Boltzmann method

There are three ways in which heat transfer can be incorporated into the LB model: The multi-speed (MS) model, the hybrid model and the double distribution function (DDF). In MS models, energy is considered as an additional velocity component so that the mass, momentum and energy equations are described with a single distribution function [50]. The hybrid approach solves the mass and momentum equations with the LBM while the temperature is found through a FV or FD scheme [51]. The respective major drawbacks of these models are possible violence of Galilean invariance and inconsistencies due to coupling between two different numerical approaches. The DDF model is considered to be the most successful thermal LB model because of its stability, accuracy and applicability for parallelization [41]. Following the recommendation of [52] the DDF approach is included in the current LB model. The working principle, the implementation in a filter-matrix model and the treatment of phase change are explained and derived in the next sections.

### 3.2.1. Double distribution function

In section 2.2.1 the similarities between the Navier-Stokes and heat equations were already pointed out. It turns out the heat equation can be solved with the lattice Boltzmann method as well leading to the double distribution function approach. A DDF LB model involves two distribution functions, one for the flow field ( $f_i$ ) and the other for the temperature field ( $g_i$ ). Similar to the flow field, the streaming and collision step can be denoted with the BGK collision operator

$$g_i(\mathbf{x} + \mathbf{c}_i \Delta t, t + \Delta t) = g_i^*(\mathbf{x}, t) - \frac{1}{\tau} (g_i - g_i^{\text{eq}}) \quad (3.15)$$

where a simple equilibrium distribution is assumed

$$g_i^{\text{eq}} = w_i T \left( 1 + \frac{\mathbf{c}_i \cdot \mathbf{u}}{c_s^2} \right) \quad (3.16)$$

and where  $\tau$  is now a relaxation time related to thermal diffusivity  $\alpha$  instead of viscosity

$$\alpha = c_s^2 \left( \tau - \frac{\Delta t}{2} \right). \quad (3.17)$$

Once the particle distribution is known, the local temperature can be derived with

$$T(\mathbf{x}, t) = \sum_i g_i(\mathbf{x}, t). \quad (3.18)$$

Eggels and Somers [53] first extended the FMLB model to a scalar transport formulation and thereby proved that the DDF approach is valid for the filter-matrix method. Again the collision operator is formed by a staggered formulation of the temperature distribution functions

$$g_i \left( \mathbf{x} + \frac{\mathbf{c}_i \Delta t}{2}, t + \frac{\Delta t}{2} \right) - g_i \left( \mathbf{x} - \frac{\mathbf{c}_i \Delta t}{2}, t - \frac{\Delta t}{2} \right) = \Delta t \Omega_i. \quad (3.19)$$

The temperature distribution function for the incompressible limit [49] is defined as

$$g_i = g_i^{\text{eq}} - w_i T \alpha \frac{\mathbf{c}_i \cdot \nabla T}{c_s^2} \quad (3.20)$$

Similarly to section 3.1.3, the temperature distributions and the solution vectors can be found with

$$g_i \left( \mathbf{x} \pm \frac{\mathbf{c}_i \Delta t}{2}, t \pm \frac{\Delta t}{2} \right) = \sum_k w_i \mathbf{E}_{ik} \beta_k^\pm \quad (3.21)$$

and

$$\beta_k^\pm = \sum_i \mathbf{E}_{ki} g_i \left( \mathbf{x} \pm \frac{\mathbf{c}_i \Delta t}{2}, t \pm \frac{\Delta t}{2} \right), \quad (3.22)$$

where the solution vectors are now

$$\beta_k^\pm(\mathbf{x}, t) = \left[ T, u_x T + \frac{-6\alpha \pm \Delta t}{6} \frac{\partial T}{\partial x}, u_y T + \frac{-6\alpha \pm \Delta t}{6} \frac{\partial T}{\partial y}, S_1^\pm, S_2^\pm, S_3^\pm, T_1^\pm, T_2^\pm, F^\pm \right]^T. \quad (3.23)$$

The second, third and fourth order terms are again set to 0.

### 3.2.2. Modelling Phase Change

In [42] several suggestions are made to include phase change in a DDF LB model. These are classified into two major categories: a phase-field model and an enthalpy-updating scheme. As phase-field models suffer from computational constraints when solving for solid-liquid interfaces [51], the enthalpy-updating scheme is more commonly used in the latest research on LB simulations of solid-liquid phase change. A series of enthalpy-based DDF LB models was developed by [40, 54, 39]. These models had to deal with latent heat in an iterative manner which greatly increased the computational cost and reduced the model efficiency. To overcome this drawback, Huang et al. [46] proposed that the temperature field and the liquid-phase fraction can be determined by enthalpy, avoiding iterations or solving a group of linear equations in numerical simulations. As, to the writer's knowledge, the enthalpy-updating scheme with or without iterations has not been implemented in a DDF FMLB model and therefore models for both will be derived and tested on accuracy and efficiency.

**Iterative scheme**

The iterative method relies on the heat equation of the form (2.11). The scheme proposed in [47] is modified to obey the filter-matrix method. The iteration steps that should be followed are

1. Calculate the temperatures according to (3.18):  $T^k(\mathbf{x}, t) = \sum_i g_i \left( \mathbf{x} - \frac{c_i \Delta t}{2}, t - \frac{\Delta t}{2} \right)$
2. Define the total enthalpies with (2.9), using the liquid fractions from the previous iteration  $k-1$ :  $H^k = C_p T^k + f_l^{k-1} L$
3. Calculate the new liquid fraction  $f_l^k$  with (2.14)
4. Modify the collision operation (3.19):
 
$$g_i \left( \mathbf{x} + \frac{c_i \Delta t}{2}, t + \frac{\Delta t}{2} \right) = \Delta t \Omega_i - \Delta t w_i \frac{L}{C_p} \left( \frac{f_l^k(t+\Delta t) - f_l(t)}{\Delta t} \right) + g_i \left( \mathbf{x} - \frac{c_i \Delta t}{2}, t - \frac{\Delta t}{2} \right)$$
5. Perform the streaming step:  $g_i \left( \mathbf{x} + \frac{c_i \Delta t}{2}, t + \frac{\Delta t}{2} \right) \rightarrow g_i \left( \mathbf{x} - \frac{c_i \Delta t}{2}, t - \frac{\Delta t}{2} \right)$
6. The temperatures for the next iteration step  $k+1$  can now be calculated. Steps 1-4 are repeated until  $f_l$  is converged:

$$\min \left( \left| \frac{f_l^k - f_l^{k-1}}{f_l^{k-1}} \right| \right) < 10^{-8} \quad (3.24)$$

**Combined transient-source term**

To let (3.15) correspond to the macroscopic equation of (2.12), the equilibrium distribution should be modified by [46]

$$g_i^{\text{eq}} = \begin{cases} L f_l + \omega_i C_p T & i = 0 \\ \omega_i C_p T \left[ 1 + \frac{c_i \cdot \mathbf{u}}{c_s^2} \right] & i \neq 0 \end{cases} \quad (3.25)$$

such that

$$H = \sum_i g_i \quad (3.26)$$

The latent heat is added to the zeroth order moment of the energy distribution function. The same can be done for the filter-matrix method. The solution for temperature distribution (3.20) is transformed to an energy distribution function with

$$g_i = \begin{cases} L f_l + \omega_i C_p T & i = 0 \\ \omega_i C_p \left[ T + T \frac{c_i \cdot \mathbf{u}}{c_s^2} - \alpha \frac{c_i \nabla T}{c_s^2} \right] & i \neq 0 \end{cases} \quad (3.27)$$

The solution vectors  $\beta_k^\pm$  are slightly modified by putting a factor  $C_p$  in front of all terms. This modification is justified because the specific heat is approximately constant in each separate phase. As of the staggered formulation of the collision operator, the latent heat term does not influence the collision step. Therefore it can be subtracted from the energy distribution  $g_0 \left( \mathbf{x} - \frac{c_i \Delta t}{2}, t - \frac{\Delta t}{2} \right)$  before the collision step and added to  $g_0 \left( \mathbf{x} + \frac{c_i \Delta t}{2}, t + \frac{\Delta t}{2} \right)$  afterwards<sup>1</sup>. Once the total enthalpy is known, the temperature and liquid fraction will follow from (2.13) and (2.14).

**3.2.3. Phase interface**

The velocity should be zero within the ice. This no-slip velocity condition on the moving interface can be imposed by two methods: the immersed boundary method and the enthalpy-porosity method. Both treat the interface as a mushy zone where the liquid fraction  $f_l$  is between 0 and 1.

<sup>1</sup>Method first introduced in the MSc thesis of T. Besseling <https://www.tudelft.nl/tnw/over-faculteit/afdelingen/radiation-science-technology/research/research-groups/reactor-physics-and-nuclear-materials/publications/msc-theses>

### Immersed boundary method

In [55] the collision operator is modified to deal with the moving interface. This modified collision operator can be implemented in the filter-matrix method by introducing a special post-collision distribution function  $f_i^S$  that remains unchanged in liquid ( $f_l = 1$ ) but will impose zero velocity in the solid region ( $f_l = 0$ ) and a no-slip condition on the ice interface:

$$f_i^S \left( \mathbf{x} + \frac{\mathbf{c}_i \Delta t}{2}, t + \frac{\Delta t}{2} \right) = f_i \left( \mathbf{x} - \frac{\mathbf{c}_i \Delta t}{2}, t - \frac{\Delta t}{2} \right) - (1 - B) \Omega_i + B \Omega_i^S \quad (3.28)$$

where  $\Omega_i$  is calculated by (3.8) in which  $f_i \left( \mathbf{x} + \frac{\mathbf{c}_i \Delta t}{2}, t + \frac{\Delta t}{2} \right)$  is the post-collision distribution function obtained through normal matrix multiplication (3.10).  $B$  is a weight factor depending on the fluid fraction and a small term  $\varepsilon$  to avoid division by zero

$$B = \frac{(1 - f_l) \varepsilon}{f_l + \varepsilon}, \quad (3.29)$$

and the additional collision term  $\Omega_i^S$  is

$$\Omega_i^S = f_j \left( \mathbf{x} - \frac{\mathbf{c}_i \Delta t}{2}, t - \frac{\Delta t}{2} \right) - f_i \left( \mathbf{x} - \frac{\mathbf{c}_i \Delta t}{2}, t - \frac{\Delta t}{2} \right) + f_i^{\text{eq}}(\rho, \mathbf{u}_s) - f_j^{\text{eq}}(\rho, \mathbf{u}), \quad (3.30)$$

which will bounce back the non-equilibrium part of the distribution function. The solid velocity  $\mathbf{u}_s = 0$  and  $j$  is the opposite of  $i$ . Once  $f_i^S \left( \mathbf{x} + \frac{\mathbf{c}_i \Delta t}{2}, t + \frac{\Delta t}{2} \right)$  is found, it will be streamed to neighbouring sites to obtain  $f_i \left( \mathbf{x} - \frac{\mathbf{c}_i \Delta t}{2}, t - \frac{\Delta t}{2} \right)$ .

### Enthalpy-porosity method

The enthalpy-porosity method treats the mushy zone as a porous medium and a Darcy momentum sink ( $S_x, S_y$ ) is added to the Navier-Stokes equations [56]

$$\rho \left( \frac{\partial u_x}{\partial t} + u_x \nabla \mathbf{u} \right) = -\frac{\partial P}{\partial x} + \rho \nabla (v \nabla u_x) - S_x u_x \quad (3.31)$$

$$\rho \left( \frac{\partial u_y}{\partial t} + u_y \nabla \mathbf{u} \right) = -\frac{\partial P}{\partial y} + \rho \nabla (v \nabla u_y) - S_y u_y. \quad (3.32)$$

The momentum sinks are related to a mushy constant  $A_{\text{mush}}$  and the liquid fraction according to

$$S_{x,y} = A_{\text{mush}} \frac{(1 - f_l)^2}{f_l^3 + \varepsilon}. \quad (3.33)$$

The mushy constant is associated with the Cozeny-Kármán equation, describing flow through packed beds. Its official definition is  $A_{\text{mush}} = \frac{180}{d^2} \rho v$  where  $d$  is the diameter of the particles, reflecting the structure of the melting front. It is now more common to set it to  $10^4 - 10^8 \text{ kg/m}^3/\text{s}$ , which has become a more universal rather than material-dependent requirement [57]. Chakraborty and Chatterjee implemented the enthalpy-porosity method in a hybrid lattice-Boltzmann method where the collision step was performed by the BGK operator [51]. To the writer's knowledge this thesis describes the implementation of the enthalpy-porosity method in a DDF filter-matrix LB model for the first time. Adjustments of the Navier-Stokes equations can be translated to the filter-matrix method by modifying the solution vectors  $\alpha_k^\pm$ :

$$\alpha_{1,2}^\pm = \left( \rho \mp \frac{\Delta t}{2} S_{x,y} \right) u_{x,y} \pm \frac{\Delta t}{2} f_{x,y}. \quad (3.34)$$

Velocities are thus found by

$$u_{x,y} = \frac{\alpha_{1,2}^- + \frac{\Delta t}{2} f_{x,y}}{\rho + \frac{\Delta t}{2} S_{x,y}} \quad (3.35)$$

and translation between solution vectors is done according to

$$\alpha_{1,2}^+ = \alpha_{1,2}^- - \Delta t S_{x,y} u_{x,y} + \Delta t f_{x,y} \quad (3.36)$$

### 3.3. Boundary conditions

In general, LB boundary conditions can be divided into two groups: the link-wise and the wet-node family in which the boundary lies on the lattice links and lattice nodes respectively. The boundary conditions implemented throughout this thesis follow the bounce-back scheme for which link-wise lattice points are better suited [31]. The bounce-back approach is chosen over other types of boundary methods for its simple implementation. In some cases, treatment of the boundaries differ from the bounce-back method. Those methods will also be described in this section.

#### 3.3.1. Walls

Solid boundaries are described with a no-slip boundary condition and modeled with the bounce-back method: populations are reflected back to where they came from at the wall. For a link-wise boundary with bounce-back halfway between nodes this can be illustrated with Figure 3.2.

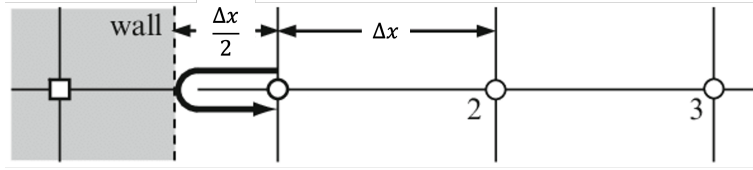


Figure 3.2: Time evolution of particle distributions during a time step  $\Delta t$  for the halfway bounce-back scheme. The dotted line denotes the boundary between the solid and fluid.

Implementation in an LB model looks like Figure 3.3. Distributions leaving the boundary node meet the surface at  $t + \Delta t/2$ , are reflected back with velocity  $\mathbf{c}_j = -\mathbf{c}_i$  and arrive at the boundary at  $t + \Delta t$ . Note that the inversion of the particle takes place solely during the streaming step. The velocity distribution function reflecting from the interface and streaming towards the boundary node are defined as

$$f_j \left( \mathbf{x}_b, t - \frac{\Delta t}{2} \right) = f_i \left( \mathbf{x}_b, t + \frac{\Delta t}{2} \right). \quad (3.37)$$

To ensure the boundary nodes feel the temperature imposed on the wall, the streaming step for the thermal distribution function at the boundary obeys an anti-bounce-back scheme [58]. There are two types of imposing the temperature on the wall. First, for the Dirichlet boundary condition, the temperature is constant at the wall and the distribution function that is reflected is determined as

$$g_j \left( \mathbf{x}_b, t - \frac{\Delta t}{2} \right) = -g_i \left( \mathbf{x}_b, t + \frac{\Delta t}{2} \right) + 2w_i(C_p)T_w. \quad (3.38)$$

The specific heat is between brackets because it is left out when dealing with phase change in the iterative scheme. When a constant heat flux is assumed, the temperature gradient is imposed on the wall resulting in a Neumann type boundary condition. Again (3.38) can be applied but the temperature on the wall  $T_w$  should be estimated. Examples of such estimation will be discussed in chapter 4.

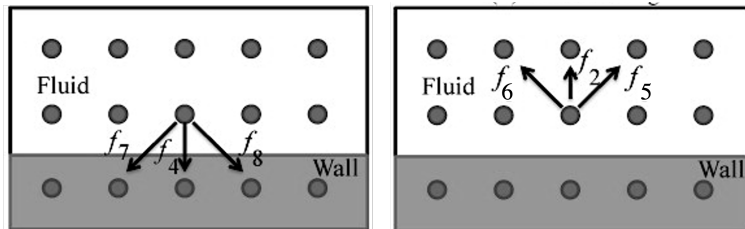


Figure 3.3: Schematic overview of the streaming step of the particle distribution on the boundary node. Left is pre-streaming and right is post-streaming. The arrows stand for the direction of the particles.

#### 3.3.2. In- and outlet

The simulation is set up such that the velocity entrance profile  $\mathbf{u}_{in}$  is known. Such a moving wall is quite simple to implement by a small correction to the solid wall bounce-back and anti-bounce-back formulas [31]

$$f_j(\mathbf{x}_b, t - \frac{\Delta t}{2}) = f_i(\mathbf{x}_b, t + \frac{\Delta t}{2}) - 2w_i\rho_0 \frac{\mathbf{c}_i \cdot \mathbf{u}_{in}}{c_s^2}, \quad (3.39)$$

$$g_j\left(\mathbf{x}_b, t - \frac{\Delta t}{2}\right) = -g_i\left(\mathbf{x}_b, t + \frac{\Delta t}{2}\right) + 2w_i(C_p)T_{in}. \quad (3.40)$$

The outflow conditions are somewhat harder to formulate as it is not known beforehand what the velocity, pressure or temperature is at the outlet. Multiple suggestions are made in literature to deal with such open boundaries. Three will be discussed here and alternately implemented in the numerical models, depending on the simulation case.

- One of the most popular outlet boundary condition in finite difference and finite volume models is the **Neumann boundary condition** where it is assumed the temperature and velocity profile do not change much in the  $x$ -direction [59]. This type of boundary condition can be translated to the LBM by copying the post collision distribution functions and macroscopic variables of the last layer  $N - 1$  to the outlet layer  $N$ . Examples for the density distribution function and velocity are given but can be extended to the thermal distribution function and other macroscopic variables.

$$f_i\left(N, t - \frac{\Delta t}{2}\right) = f_i\left(N - 1, t - \frac{\Delta t}{2}\right) \quad (3.41)$$

$$\mathbf{u}(N, t) = \mathbf{u}(N - 1, t) \quad (3.42)$$

- Another type of outflow boundary extensively used in computational fluid dynamics is the **convective boundary condition** which assumes  $\frac{\partial}{\partial t} + U\frac{\partial}{\partial x} = 0$  at the domain exit. The velocity term  $U$  can best be taken as the mean of the existing velocity profile in the lateral direction. To conserve momentum, the mean is taken at the entrance. The convective boundary condition in discretised form is then [60]

$$f_i\left(N, t - \frac{\Delta t}{2}\right) = \frac{f_i\left(N, t + \frac{\Delta t}{2}\right) + Uf_i\left(N - 1, t - \frac{\Delta t}{2}\right)}{1 + U}. \quad (3.43)$$

No further modification of the macroscopic variables is necessary.

- A different way to treat open boundaries is with **periodic boundary conditions**. These conditions can only be applied when the flow system is cyclic. Additional layers are added before and after  $x_0$  and  $x_N$  as virtual nodes. Before the streaming step,  $f_i$  and  $g_i$  from the opposite edge of the domain are copied into these nodes to ensure that fluid leaving the domain on one side enters directly on the other side.

$$f_i\left(N, t - \frac{\Delta t}{2}\right) = f_i\left(0, t + \frac{\Delta t}{2}\right) \quad (3.44)$$

### 3.4. Conversion parameters

LB simulations are mostly performed in dimensionless lattice units. Conversion parameters between physical and lattice units must therefore be predefined, taking into account intrinsic restrictions on the LB scheme. This section proposes a conversion scheme to help the reader understand and implement the LB model developed in this thesis. Conversion factors are found by dividing the physical quantity by the same quantity in lattice units. The last is denoted with an asterisk \* in this section for clarity, but is left out in the rest of the report. It is convenient to set  $\Delta x^*$ ,  $\Delta t^*$  and the reference lattice density  $\rho_0^*$  to unity. The maximum velocity  $U^*$  should not exceed 0.1 or even 0.035 in more complex cases if accurate results are desired [31]. From this, all necessary conversion factors can be derived

$$C_l = \frac{\Delta x}{\Delta x^*} = \Delta x, \quad C_p = \rho, \quad C_u = \frac{U}{U^*} \rightarrow C_t = \frac{C_l}{C_u} \quad (3.45)$$

Other conversion factors follow from the law of similarity: dimensionless numbers ( $Re, Pr$ ) must be identical in both unit systems.

$$1 = \frac{C_l C_u}{C_v} \rightarrow C_v = C_l C_u, \quad C_v = C_\alpha \quad (3.46)$$

No stability criterion is imposed on the temperature so no conversion is needed for  $T$  and thus follows directly from LB simulations in the correct units. Conversion factors for enthalpy  $H$ , specific heat  $C_p$  and latent heat  $L$  are the same and found based on their dimensions

$$C_h = C_u^2. \quad (3.47)$$

The above procedure to find all conversion factors, is followed in the same order for every case discussed in this study.

### 3.5. Adaptive mesh refinement

Existing multiphase LB models are usually performed on a uniform Cartesian grid which simplifies model implementation and reduces numerical complexity. However, it greatly increases computation time when dealing with a large domain or small grid spacing to improve the accuracy of the model. Especially the last is necessary in multiphase fluid simulations as it includes a moving interface across which fluid properties may change sharply. An adaptive, non-uniform mesh where the grid is refined locally and dynamically is introduced to deal with the icelayer both accurately and efficiently.

#### 3.5.1. Refinement

The technique of [61] is used to apply grid refinement. The domain is divided into two parts: a fine grid and a coarse grid. The phase interface lies fully in the fine grid. These grids have different time and space scales and are connected through the level of refinement  $n$ . This will affect the lattice parameters on the fine grid as some conversion factors will differ. New conversion factors on the fine grid can be found using the procedure described in 3.4 with  $\Delta t_c^* = n\Delta t_f^*$  and  $\Delta x_c^* = n\Delta x_f^*$ .

On both grids the collision and streaming operations are performed according to the filter-matrix LB method. However, care should be taken in particle distributions streaming from the fine to the coarse grid or the other way around (dashed lines in Figure 3.4). The communication between the coarse and fine grid starts with a collision step on both grids. The particles that do not cross the interface can be streamed directly to their neighbouring sites (solid lines in Figure 3.4). The particles that do cross the interface need some modification to correctly simulate the communication step between the coarse and the fine grid.

- A) **Fine**  $\rightarrow$  **coarse**: As one time step on the coarse grid corresponds to  $n$  timesteps on the fine grid, the particle distributions crossing the interface are only  $\frac{1}{n}$  of the total communication step.
- B) **Coarse**  $\rightarrow$  **fine**: The density distribution functions in a refined cell should be the same as the distribution function in the original coarse cell. Therefore, the distribution functions in the coarse grid can be redistributed over  $(n \times n)$  refined cells, located in the original coarse cell. The distributions in the bottom row of this refined grid with velocity directions  $c_i$  pointing towards the fine grid can then be streamed towards the fine grid in the standard way.

After the initial collision and streaming step on both grids, collision and streaming are performed  $(n - 1)$  times on the fine grid only, including the communication step between the two grids (A and B). Since  $(n \times n)$  particle distributions have streamed towards the coarse grid in the communication step, they must be summed with corresponding weights  $\frac{1}{n^2}$  to get the incoming particle distribution functions for the coarse grid. For more details on the implementation of this refinement technique, the reader is referred to [61].

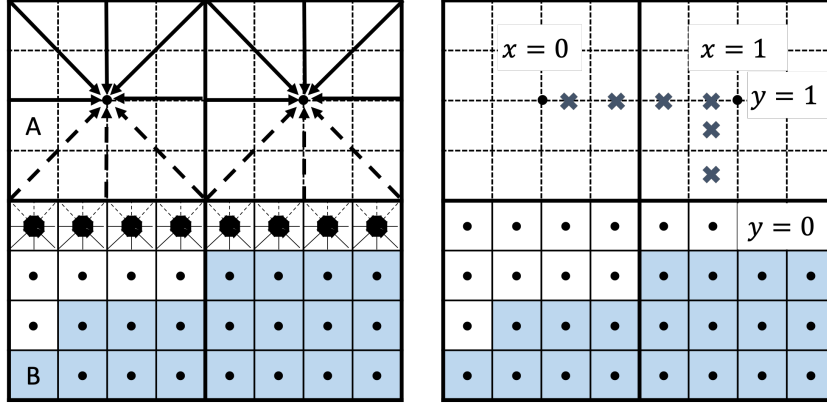


Figure 3.4: Schematic overview of: (left) the communication between the fine (B) and the coarse (A) grid, level of refinement  $n = 4$ ; (right) the interpolation method.

### 3.5.2. Adaptivity

The fine grid should move along with the growing ice layer. Once the distance between the phase interface and the boundary between the coarse and the fine grid reaches a critical value, the fine grid should be expanded. In [62] interpolation of flow variables is used to transform coarse cells into fine cells. Note that it is not necessary to interpolate the distribution functions  $f_i$  (and  $g_i$ ) as they can be derived from the macroscopic variables. In the filter-matrix method this translates to interpolating the solution vectors  $\alpha_k$  (and  $\beta_k$ ) linearly with (3.48) and calculate the density and thermal distribution functions with (3.10) and (3.21).

$$\alpha_k = \alpha_k(0)(1 - x, y) + \alpha_k(1)(x, y) \quad (3.48)$$

## 3.6. Numerical implementation

The numerical procedure to perform the collision and streaming of the density and energy distribution functions and calculate macroscopic variables is shown schematically in Figure 3.5. The steps taken are:

- Initialisation of  $\alpha_k^-$  and  $\beta_k^-$  by constructing the vectors (3.14) and (3.23) with initial values for  $\rho_0, \mathbf{u}_0, f_{l0}$  and  $T_0$ . Initial guesses can be made for  $f_i \left( \mathbf{x} - \frac{c_i \Delta t}{2}, t - \frac{\Delta t}{2} \right)$  and  $g_i \left( \mathbf{x} - \frac{c_i \Delta t}{2}, t - \frac{\Delta t}{2} \right)$  with (3.10).
- The density and velocities follow directly from the solution vectors  $\alpha_k^-$ . Other macroscopic variables should be updated by (3.26), (2.13) and (2.14). It is useful to introduce parameters  $G = \frac{-6v+1}{-6v-1}$  and  $\bar{G} = \frac{-6\alpha+1}{-6\alpha-1}$  as they help transform  $\alpha_k^-, \beta_k^-$  into  $\alpha_k^+, \beta_k^+$ . For example

$$\alpha_4^+ = G(\alpha_4^- - 3\rho u_x u_y) + 3\rho u_x u_y \quad (3.49)$$

$$\beta_{2,3}^+ = \bar{G}(\beta_{2,3}^- - u_{x,y} T) + u_{x,y} T \quad (3.50)$$

The velocities derived from  $\alpha_k^\pm$  are given as input to create solution vector  $\beta_k^\pm$ . Note that  $v$  and  $\alpha$  might be locally dependent on liquid fraction or temperature.

- Once  $\alpha_k^+$  and  $\beta_k^+$  are known,  $f_i \left( \mathbf{x} + \frac{c_i \Delta t}{2}, t + \frac{\Delta t}{2} \right)$  and  $g_i \left( \mathbf{x} + \frac{c_i \Delta t}{2}, t + \frac{\Delta t}{2} \right)$  are calculated with (3.10) and (3.21). The phase interface is treated according to (3.28) or (3.34).
- If the velocity and temperature profiles are converged, the boundary conditions should be dropped below the melting point of the fluid.
- The distributions  $f_i \left( \mathbf{x} + \frac{c_i \Delta t}{2}, t + \frac{\Delta t}{2} \right)$  and  $g_i \left( \mathbf{x} + \frac{c_i \Delta t}{2}, t + \frac{\Delta t}{2} \right)$  are streamed towards their neighbouring sites to get  $f_i \left( \mathbf{x} - \frac{c_i \Delta t}{2}, t - \frac{\Delta t}{2} \right)$  and  $g_i \left( \mathbf{x} - \frac{c_i \Delta t}{2}, t - \frac{\Delta t}{2} \right)$ . If the phase interface is less than  $n$  grid points away from the coarse grid, the adaptive mesh refinement (AMR) technique should be applied before proceeding to the next step.
- The solution vectors  $\alpha_k^-$  and  $\beta_k^-$  are calculated with (3.11), (3.22). The process goes back to step b), repeating itself for the predefined number of time steps.

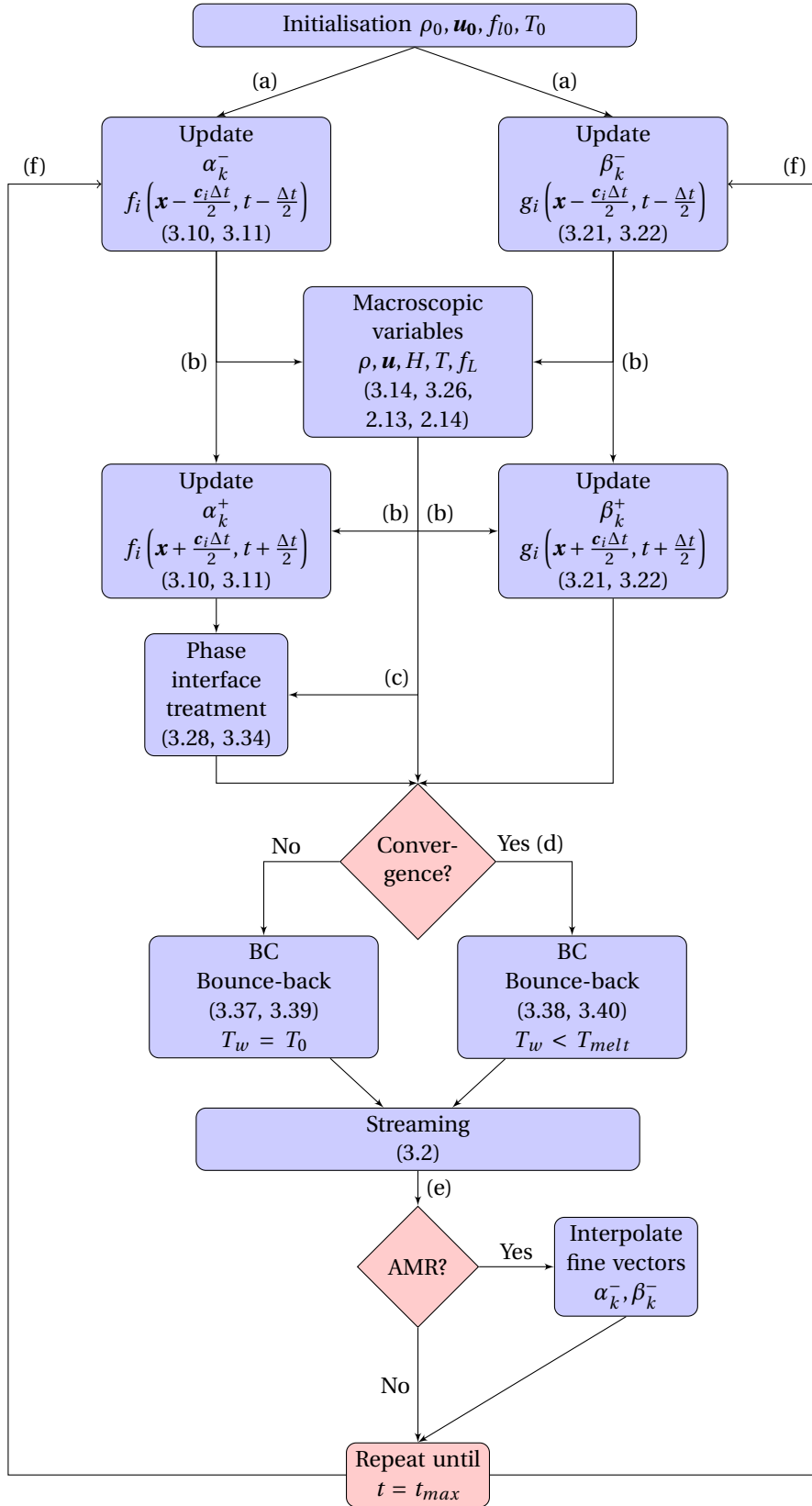


Figure 3.5: Schematic overview of the numerical algorithm.

# 4

## Validation by analytical solutions & experimental results

The goal of this research is to correctly simulate freezing in molten salt flows in order to find the effect of the transient growing salt augmentation on the heat transfer processes present in an MSFR. To justify the results for molten salts found by the numerical model, it should be able to accurately simulate benchmark cases of which the solution is known analytically or found experimentally. The lattice Boltzmann model build for the current research is a double distribution filter matrix (DDF FMLB) model that treats phase change through the source based enthalpy method. The three different elements the model is build of (two distribution functions and the phase change method) are validated and optimised separately in 4.1 by comparing them with known analytical solutions. Hereafter, they are put together to form the complete phase change DDF FMLB model and are tested on two experimental benchmark cases in 4.2. This section will first check the grid convergence and energy conservation of the model, followed by treatment of two test cases differing only in the definition of the thermal boundary on the wall: cooling is either imposed by constant heat removal or an isothermal wall below the freezing temperature. Conditions of both experimental studies are translated to the LB model and simulations will be compared and discussed.

### 4.1. Validation of model components

The physics behind fluid dynamic processes has been studied extensively in literature which has lead to analytical solutions of some specific cases. These solutions are perfect benchmark cases in order to test if numerical models are working correctly. Throughout this section three of these benchmark cases are tested on the build DDF FMLB model. First, the performance of the velocity distribution function is tested by simulating Poiseuille flow. The addition of an extra thermal distribution function, forming the basis of the DDF model, is tested by finding the Nusselt relation in heated convective flow. Finally, the implementation of phase change is validated by the Stefan problem. In order to judge the model performance quantitatively, deviations from analytical or experimental results throughout this chapter are calculated by means of the Root Means Squared Error (RMSE) and the Relative Root Mean Squared Error (RRMSE)

$$\text{RMSE} = \sqrt{\frac{1}{N} \sum_{i=0}^N (y_i - \tilde{y}_i)^2} \quad (4.1)$$

$$\text{RRMSE} = \sqrt{\frac{1}{N} \sum_{i=0}^N \left( \frac{y_i - \tilde{y}_i}{y_i} \right)^2} \quad (4.2)$$

where the analytical results  $y_i$  are compared to the solutions following from the LB simulations  $\tilde{y}_i$ , with solution index  $i$  and number of data points  $N$ .

#### 4.1.1. Forced Convection

The end goal is to simulate freezing in laminar convective flow through a two-dimensional parallel plate geometry which is cooled from one side. For that, flow, temperature and phase change should all be modeled

correctly. In this section the convective part of the model is validated. First, the benchmark case of Poiseuille flow is compared to the velocity field computed with a single-distribution function FMLB model. To also validate the treatment of thermal flows with a DDF FMLB model, the Nusselt relation from the LB simulation is compared to the approximate analytical solution. Throughout this section a distinction will be made between the velocity and thermal entrance and developed region. The definition of these regions is best visualised with Figure 4.1.

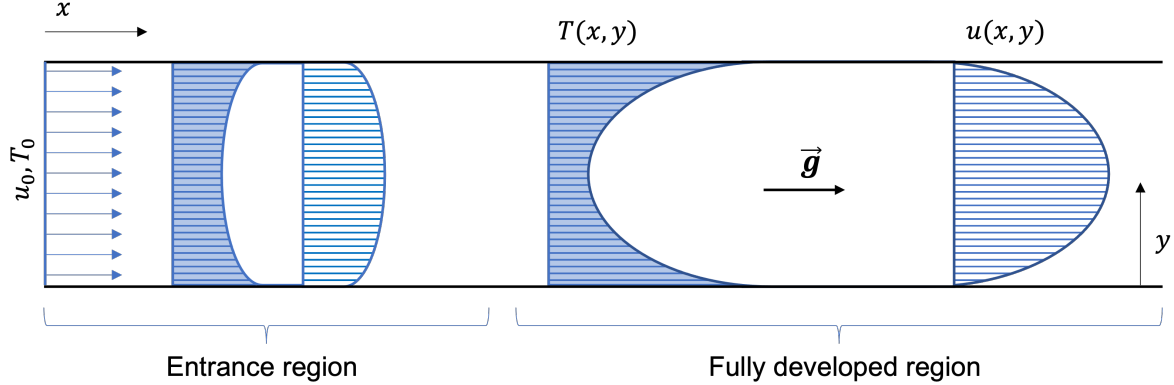


Figure 4.1: Schematic overview of the entrance and fully developed region of velocity and temperature.

### Poiseuille flow

Physically, a two-dimensional parallel plate geometry is assumed through which water flows lamarily, driven by a body-force. No-slip boundary conditions on the walls cause the resulting flow profile of a Newtonian fluid, given by (2.6). In the LB simulation, a Poiseuille flow can be created by imposing a body force  $f_x = \rho g_x$  in (3.14). The inlet velocity profile is flat and is modeled by the inlet condition (3.39). The outflow boundary obeys the Neumann condition. The viscosity is assumed to be uniform throughout the domain. Note that a single distribution function will solve the problem as no thermal treatment is needed. The non-adaptive grid refinement technique is also tested. The numerical and physical parameters are given in Table 4.1.

Table 4.1: Parameter definition for the simulation of Poiseuille flow and physical parameters water

Variable	Description	Value
$W \times H$	Length and height of the channel	$25 \times 5$ mm
$N_{x,c} \times N_{y,c}$	Number of coarse grid points	$100 \times 17$
$N_{x,f} \times N_{y,f}$	Number of fine grid points	$400 \times 12$
$f_x$	Body force	$8.3e-3$ N
$u_{in}$	Inlet velocity	$1.74$ cm/s
$\nu$	Viscosity	$1.5$ mm <sup>2</sup> /s
$C_u$	Velocity conversion factor	1
$n$	Level of refinement	4

As the velocity profile is uniform at the entrance, it takes some travel distance to become fully developed. Only then, the results from the LB simulation can be compared to the analytical solution. This so-called entrance region depends on channel geometry and fluid flow properties. The analytical solution assumes a uniform density throughout the domain. However, friction on the wall will cause a pressure gradient. In an LB simulation, pressure and density are related, thus also a density gradient along the flow direction will rise. Therefore the mass flux  $\rho(x, t) u_x(x, t)$  is compared to the analytical solution rather than the velocity profile in Figure 4.2.

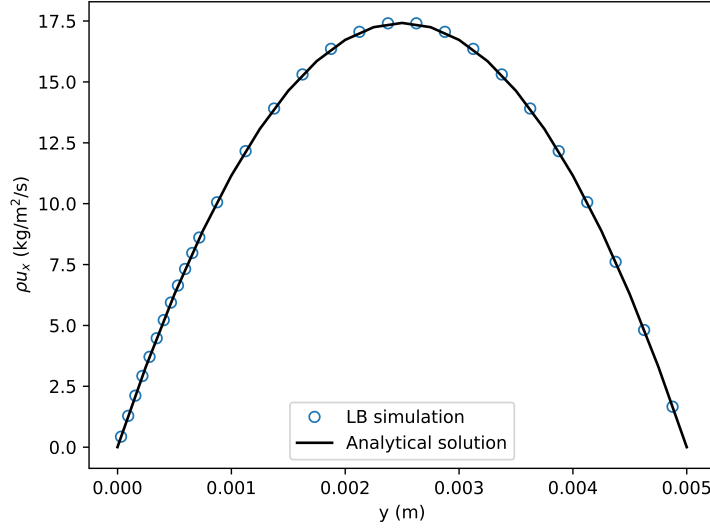


Figure 4.2: Comparison between LB simulation and the analytical result for Poiseuille flow. Level of refinement  $n = 4$ .

The numerical result matches the analytical solution perfectly. It can be concluded that the refined FMLB model is capable of modeling convective laminar flow between parallel plates for the given input parameters. In the next section an extra distribution function is added to form a DDF FMLB model to simulate thermal flows.

### Nusselt relation

A way to test the combined velocity and thermal distribution function is deriving the Nusselt relation from simulations and compare it to the approximate analytical solution for the Nusselt number of laminar flow between parallel plates. The local Nusselt number  $Nu(x)$  depends on heat transfer according to

$$h(x) = \frac{Nu(x)\lambda}{D} = \frac{q''(x)}{T_w - T_{\text{bulk}}(x)}. \quad (4.3)$$

where  $h(x)$  is the local heat transfer coefficient,  $\lambda$  the thermal conductivity in the fluid,  $q(x)$  the local heat flux at the wall and  $D$  the hydraulic diameter which is two times the distance  $H$  between the parallel plates. The bulk temperature is defined as [63]

$$T_{\text{bulk}}(x) = \frac{\int_0^H \rho C_p \mathbf{u} T dy}{\int_0^H \rho C_p \mathbf{u} dy}. \quad (4.4)$$

The Nusselt relation for the thermal entrance region in laminar flow between heated parallel plates is analytically approximated by [64]

$$Nu(x) = 3.12\tilde{x}^{-1/3} \quad (4.5)$$

where  $\tilde{x} = \frac{x\alpha}{UD^2}$  in which  $U$  is the average velocity. A similar relation is aimed to be found by the DDF FMLB model. As this approximate solution for the local Nusselt number is only valid in the thermal entrance region where  $\tilde{x} < 0.1$ , the simulation dimensions are chosen such that the entire domain is in the thermal entrance region. A fully developed Poiseuille flow with uniform temperature  $T_0$  is given as inlet velocity by (3.39) and (3.40). No body force is applied. First, the temperature on the walls is kept at  $T_w = T_0$  in order to converge the velocity and temperature. Once values for velocity and temperature are fully converged, a temperature  $T_w > T_0$  is imposed on the walls by the anti-bounce back scheme of (3.38). While the thermal profile is still developing in the thermal entrance region, it can be assumed to change smoothly such that Neumann boundary conditions are suitable for both the velocity as temperature distribution functions at the outlet [65]. All temperatures are kept above the freezing temperature so we do not have to deal with phase

change yet. The physical properties are assumed to be constant throughout the domain and are summarised together with numerical parameters in Table 4.2.

Table 4.2: Parameter definition of thermal laminar flow between parallel plates

Variable	Description	Value
$W \times H$	Length and height of the channel	$20 \times 10$ cm
$N_x \times N_y$	Number of grid points	$150 \times 75$
$u_{\max, \text{in}}$	Maximum velocity of the Poiseuille profile	1 mm/s
$T_0$	Inlet temperature	280 K
$T_w$	Wall temperature	282 K
$\nu$	Viscosity	$1.5 \text{ mm}^2/\text{s}$
$\alpha$	Thermal diffusivity	$0.13 \text{ mm}^2/\text{s}$
$\lambda$	Thermal conductivity	$0.57 \text{ W/m/K}$
$C_u$	Velocity conversion factor	1

Once the heating of the parallel plates starts, the  $Nu(x)$  can be determined if  $T_{\text{bulk}}(x)$  and  $q''(x)$  are known. The heat flux follows directly from  $\beta_2^\pm$  in the solution vector as

$$q''(x) = -\lambda \left. \frac{dT(x)}{dy} \right|_{y=0}. \quad (4.6)$$

The resulting Nusselt number as function of  $\tilde{x}$  is compared to the approximate analytical solution in Figure 4.3. There is reasonable agreement between the solutions as the RMSE = 25 and the RRMSE 18%. The  $\tilde{x}^{-1/3}$  dependence is also clearly visible. However, there is some discrepancy between the analytical approximation and the LB simulation. This can be clarified by assumptions made in the analytical approach. The velocity profile is assumed to be linear in the thermal boundary layer which is only valid if the temperature field change is limited to a region close to the wall. This assumption might be accurate at the beginning of the entrance region where the thermal boundary layer is small but becomes less precise with increasing thickness of the thermal boundary layer along  $x$ , which could explain the deviation from  $\tilde{x} > 0.0001$ . The numerical determination of  $Nu$  is sensitive to fluctuations in  $T_{\text{bulk}}(x)$  and  $q''(x)$ . Local velocity or temperature could deviate from their physical values (often the case near domain boundaries), influencing the Nusselt number calculation. This effect will be less significant in finer grids. In the next section the source-based enthalpy method will be tested on conduction induced freezing in the absence of convective flow.

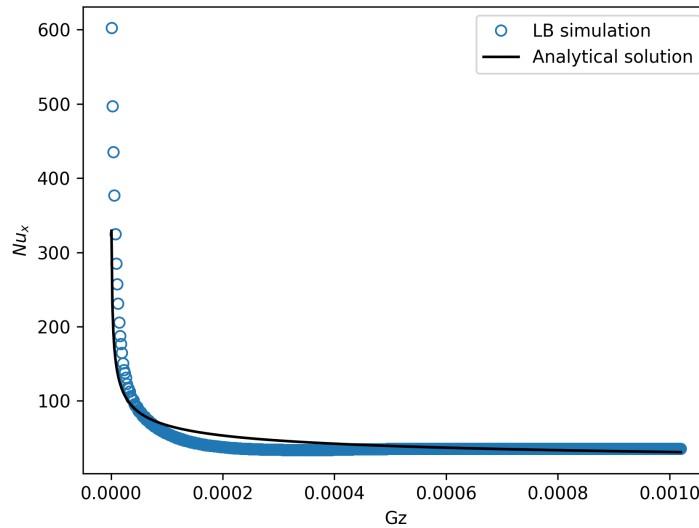


Figure 4.3: The Nusselt number  $Nu$  as function of  $\tilde{x}$  in the thermal entrance region

### 4.1.2. Stefan Problem

The Stefan problem has been discussed in 2.2.2 and will be used as a benchmark case to prove the enthalpy-based method is correctly implemented in the FMLB model, and to examine the differences in accuracy and efficiency between the transient-source and iterative scheme. Water is initially at  $T_0 > T_f$ , at  $t = 0$  a temperature  $T_b < T_f$  is imposed on the wall, such that water will freeze and a moving ice front forms. To simulate a semi-infinitesimal domain, adiabatic boundary conditions and periodic boundary conditions are applied on the right wall and top and bottom walls respectively. Adiabatic conditions are imposed by replacing  $T_w$  in (3.38) by the temperature of the grid point closest to the wall. The velocity and gravitation are set to zero as there is no convection. Therefore, only a single distribution function is needed, either for energy or temperature depending on the chosen phase change model. The parameters that define the problem are summarised in Table 4.3. The thermal diffusivity and specific heat are locally dependent as they are different for ice and water, but are assumed to be uniform within the same phase.

Table 4.3: Parameter definition of the Stefan problem and physical parameters water

Variable	Description	Value
$H$	Length of the channel	6 cm
$T_f$	Freezing temperature	273.15 K
$T_0$	Initial temperature	273.2 K
$T_b$	Cold wall temperature	250 K
$L$	Latent heat	334 kJ/kg
$\alpha_{s/l}$	Thermal diffusivity (solid/liquid)	(0.131 / 1.18) mm <sup>2</sup> /s
$C_{p,s/l}$	Specific heat (solid/liquid)	(2.0 / 4.2) kJ/kg/K

The ice front will be  $0.5\Delta x$  in front of the last index where  $f_l = 0$ . The deviations from the analytical solution and computation times for both methods are summarised in Table 4.4. Simulation solutions for the moving ice interface and temperature distributions are compared to the analytical solution in Figure 4.4. Both agree well but the iterative scheme delivers slightly better results in terms of accuracy. What is remarkable is that the computation time for the iterative scheme is not that much higher than for the combined transient-source term method. It could be that the convergence criterion (3.24) is easily met for the Stefan problem such that not many iterations are needed to get good results. For more complex phase change problems the iterative scheme might become less efficient and therefore the combined transient-source scheme is implemented throughout the rest of this thesis.

Table 4.4: Comparison of the accuracy metrics and computation times for the combined transient-source term method and the iterative scheme.

Metric	Transient-source		Iterative	
	$\delta$ (m)	$T$ (K)	$\delta$ (m)	$T$ (K)
RMSE	5.8e-5	[0.19, 0.24, 0.12, 0.11]	5.7e-5	[0.13, 0.20, 0.12, 0.11]
RRMSE (%)	0.48	[0.07, 0.09, 0.04, 0.04]	0.46	[0.05, 0.08, 0.04, 0.04]
$t_{\text{comp}}$ (s)		4.9		5.1

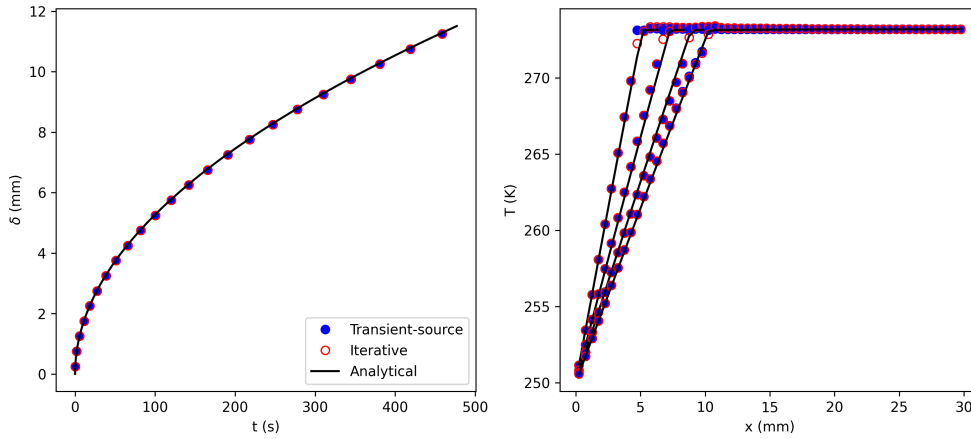


Figure 4.4: Left: the ice thickness  $\delta$  growing in time  $t$ . Right: the temperature distribution along  $x$  for  $t = 100, 200, 300, 400$  s.

## 4.2. Experimental benchmark cases

All elements that build up the phase change DDF FMLB model are now validated by comparing their individual simulations to analytically known results of fluid dynamic processes. They are merged together to form a model that can deal with freezing in thermal laminar flow through a two-dimensional cooled channel. To prove that the current model is reliable and will generate correct predictions under various conditions, its grid convergence and energy conservation are tested in 4.2.1. It is desired to also make a comparison with experimental findings. However, not much research has been done on transient freezing in convective flow due to its complex nature. Only some papers have found experimental or analytical values for the transient ice thickness under flux or isothermal boundary conditions on the wall. Examples of such will be given in 4.2.2 and 4.2.3 together with their translation to the developed LB model. In every case, a comparison between experimental or analytical results and the LB simulation is made and discussed. Found limitations are mostly related to the definition of the boundaries and will be discussed parallel to the comparison.

### 4.2.1. Grid convergence and energy conservation

Before the model can be compared to experimental cases, it must be checked on grid convergence and energy conservation. In a grid convergence study, the spatial dimension is refined multiple times until results do not change upon further refinement. To test both distribution functions, the maximum velocity and outlet temperature are monitored under spatial refinement. Their input values are  $u_{\max, \text{in}} = 1$  cm/s and  $T_0 = 278.15$  K respectively. The domain is assumed to have constant height  $H = 5$  cm and length  $W = 8$  cm. Time step  $\Delta t$  is dependent on  $\Delta x$  and thus the number of time steps after which  $u_{\max}$  and  $T_{\text{out}}$  are checked, must increase upon refinement. Both velocity and temperature converge to an approximately unchanged constant in Figure 4.6a, indicating grid convergence.

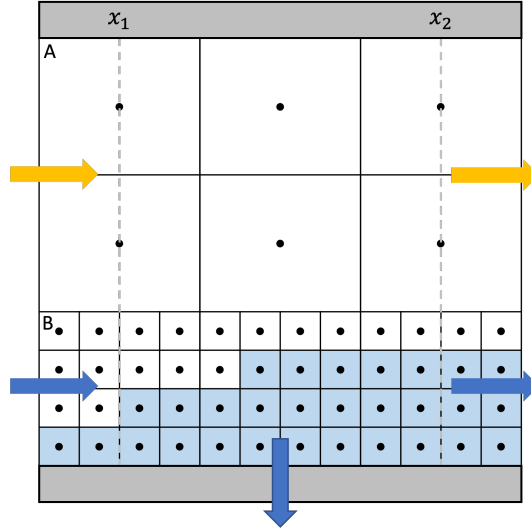


Figure 4.5: Schematic overview of energy flowing in and out a control volume. A separation is made between the orange flows through the coarse (A) and blue flows through the fine (B) grid. A hypothetical ice layer is present in the fine grid.

Another important aspect of a numerical model is that it should conserve energy. This can be checked by setting up a thermal energy balance over a control volume. In the current model, this looks like Figure 4.5. Under transient conditions the change in thermal energy is determined by

$$\int_0^H \int_{x_1}^{x_2} \rho \frac{\partial H}{\partial t} dx dy = \int_0^H \rho C_p \mathbf{u} T dy \Big|_{x_1} - \int_0^H \rho C_p \mathbf{u} T dy \Big|_{x_2} - \int_{x_1}^{x_2} \lambda \frac{\partial T}{\partial y} dx \Big|_{y=0}. \quad (4.7)$$

Phase change is incorporated in the total enthalpy term on the left hand side. The difference between the left and right hand side is determined in each time step from the moment cooling starts. The result of one of the cases elaborated in this chapter is given in Figure 4.6b. The difference is given as percentage of the largest term in (4.7): the energy flux entering the control volume. The energy difference converges to 0% for increasing time steps. The fluctuations at the start are the result of the initiation of solidification. Together with grid convergence, the conservation of energy is a good indication that the model is correctly simulating physical processes. However, comparison with experimental benchmark cases must further validate this claim.

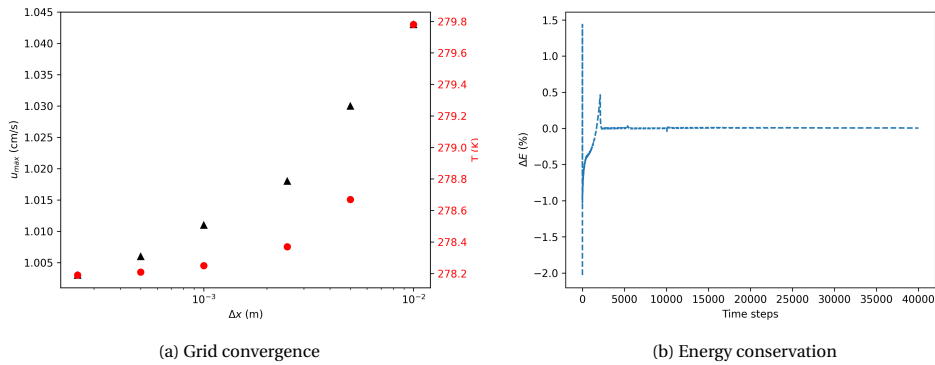


Figure 4.6: Results of the grid convergence (left) and energy conservation (right) study.

### 4.2.2. Constant heat flux

The transient ice growth in water flowing laminarly through a rectangular channel is examined experimentally in [14]. The water is cooled by constant heat removal. This section will shortly explain the experiment performed and how the conditions in the experiment are translated to the numerical conditions. Hereafter, results of both will be compared and differences will be discussed.

### Experiment

The details of the test section are given schematically in Figure 4.7. The channel is made of Perspex and has height  $H = 6$  mm in the  $y$ -direction. A section of the top part of the channel is cut out and replaced by a copper plate with thickness  $d = 1$  mm along  $y$ . The plate has smaller dimensions in  $x$  and  $z$  than the channel to avoid faster solidification along the sides. Boiling liquid nitrogen (76 K) is poured over the copper plate such that a constant heat flux is imposed, the water is cooled and solidification is induced. The dimensions are chosen such that the quasi-two-dimensional assumption holds. The laser is put in the middle of the section to minimise the boundary effects along  $z$  (see bottom Figure 4.7). The ice thickness and velocity field are tracked simultaneously for different flow conditions. The flow rates  $Q_0$  and inlet temperatures  $T_0$  are varied from 3 to 50 L/h and 7 to 33 °C, respectively. The measurements are taken towards the end of the copper plate ( $x \approx 35H$ ) to ensure the ice profile is approximately uniform.

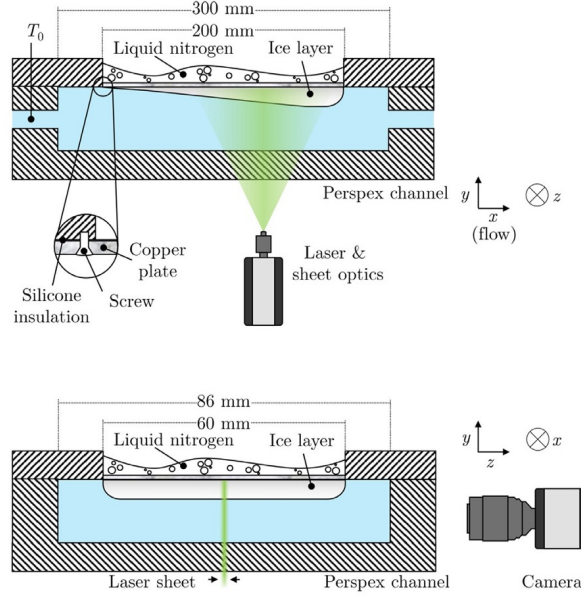


Figure 4.7: Test section and optics arrangement. Top: x-y view; bottom y-z view [14].

The heat flux on top of the copper plate is estimated with

$$q''_{\text{out}} = h_{\text{LN}_2}(T_{\text{boil}} - T_w) \quad (4.8)$$

The wall temperature  $T_w$  and the liquid nitrogen heat coefficient  $h_{\text{LN}_2}$  are determined from measurements of the temperature drop in the wall when the channel is left empty (no water is flowing through) and liquid nitrogen is poured on top. More details on this procedure are found in [14]. The resulting calculated heat flux, including measurement error, is  $q''_{\text{out}} = 20 \pm 1$  kW/m<sup>2</sup>.

The experiments resulted in quasi-linear ice growth  $\frac{dX_{\text{ice}}}{dt}$  and an accelerated velocity profile for various flow conditions. A dependence on inlet temperature and velocity is found for  $\frac{dX_{\text{ice}}}{dt}$  and the time-lag period  $\tau$ : the time it takes before ice starts to form. These results are tried to be reproduced by an LB simulation.

### Numerical conditions

The two-dimensional DDF FMLB model build so far will simulate the experiment explained above. The enthalpy-based method with a combined transient-source term is implemented to deal with phase change. The immersed boundary method is chosen to impose the no-slip boundary condition on the moving phase interface. The no-slip boundary conditions on the top and bottom wall are realised with the bounce-back scheme. The inlet velocity and temperature are imposed by (3.39) and (3.40). The outflow can either be modelled by the Neumann boundary or convective boundary condition. The most optimal choice is found during the numerical study. Adiabatic conditions  $q = 0$  are assumed for the bottom wall. Most care should be taken in how the constant heat removal is translated to a suitable boundary condition on the top wall. To estimate the temperature in the wall correctly, a heat balance over a computational cell in the copper plate is

set up like Figure 4.8. The wall temperature is assumed to be uniform along  $y$  because  $\lambda_{Cu} \gg \lambda_{ice}$ . The wall temperature cannot be assumed uniform along  $x$  as  $q''_{in}$  is locally dependent. The heat balance is solved by a finite difference scheme. Depending on whether the copper plate is in contact with ice ( $f_l(i, N) = 0$ ) or water ( $f_l(i, N) = 1$ ), the equation to be solved is

$$\rho_w C_{p,w} \Delta x d \frac{T_{i,w}^{n+1} - T_{i,w}^n}{\Delta t} = \Delta x q''_{in} - \Delta x q''_{out} - d \lambda_{Cu} \frac{T_{i,w}^n - T_{i-1,w}^n}{\Delta x} + d \lambda_{Cu} \frac{T_{i+1,w}^n - T_{i,w}^n}{\Delta x} \quad (4.9)$$

$$q''_{in} = \begin{cases} -\lambda_{ice} \frac{\partial T}{\partial y} \Big|_{y=N} & f_{l,N} = 0 \\ h(x) (T_{bulk}(x) - T_{i,w}) & f_{l,N} > 0 \end{cases} \quad (4.10)$$

As liquid nitrogen is poured *on top of the channel*, mixed forced and free convection effects are present and the known Nusselt relation cannot be applied to find  $h(x)$ . Instead,  $h(x) = h = 5.1 \cdot 10^2 \text{ W/m}^2/\text{K}$  is found experimentally in [14] and is applied to the current model to accurately impose the boundary. For the unique moment that ice has just started to form and  $f_l(i, N)$  is between 0 and 1, the assumed boundary condition might be incorrect as there will be mixed convection and conduction effects present in the computational cell near the wall. As this is the case during a short time of the simulation, it is expected that it will not effect the results for ice growth  $\frac{dX_{ice}}{dt}$  significantly. However, it might effect the results for  $\tau$  which will be discussed in the next section.

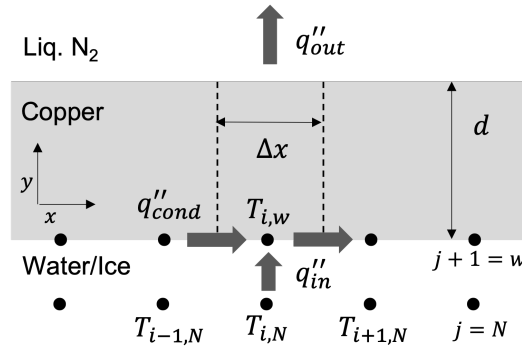


Figure 4.8: Schematic overview of the finite difference scheme representing the thermal boundary condition on the wall.

The input parameters that are constant for every simulation run are summarised in Table 4.5. Adaptive mesh refinement will ensure accurate tracking of the ice layer while keeping the computation time in an acceptable range. The inlet temperature  $T_0$  and the average inlet velocity  $u_{av}$  are varied within the range of the experimental values in [14]. The inlet velocity profile is assumed to be parabolic such that  $u_{max} = 1.5u_{av}$ , like Poiseuille flow. The maximum LB velocity is set to 0.01 as during simulations it was found that instabilities rose above 0.05. It is expected fluid is accelerated by the converging cross-sectional area thus to be in the stable limit, 0.01 is chosen. No explicit numbers for  $u_{av}$  are given, however they can be deduced from the flow rate as  $u_{av} = Q_0/A$  with  $A$  the cross-sectional area of the channel. The thermophysical properties of water, ice and copper are now a function of temperature to approach the experimental conditions in the best possible way. Their dependencies are given in Appendix A

Table 4.5: Physical and numerical parameter definition for forced laminar flow between parallel plates cooled by a constant heat flux

Variable	Description	Value
H	Height of the channel	6 mm
n	Level of refinement	4
$q_{out}$	Heat flux on top of the channel	-20 kW/m <sup>2</sup>
$u_{max, LB}$	Maximum velocity in LB units to ensure stability	0.01
$u_{max, in}$	Maximum inlet velocity	[0.6, 1.2, 2.4] cm/s
$\rho_w$	Density copper wall	8960 kg/m <sup>3</sup>
$d$	Wall thickness	1 mm

Ice growth will be monitored by updating  $f_l$  in each time step. From that,  $\tau$  and  $\frac{dX_{ice}}{dt}$  can be determined. Results for different flow conditions are given in the next section and compared with the experimental results.

### Comparison of results

The Prandtl number is  $Pr \sim 10$  in water, and because the collision steps in the DDF FMLB model depend on  $\nu$  and  $\alpha$ , the thermal model takes  $\sim 10$  longer to converge. The choice in outflow boundary condition can help to improve convergence. The velocity and temperature profile resulting from the Neumann and convective outflow boundary condition are compared in Figure 4.9 for different convergence time steps. The convective boundary condition will converge the temperature profile faster and closer to the initial temperature. A possible explanation could be that the Neumann boundary condition assumes  $\partial T/\partial x \approx 0$ , an approximation not completely valid when the temperature profile is still converging. The convective boundary condition assumes that the material derivative near the domain exit is unchanged, something that can be assumed for flow properties that are converging. The streaming step in the LB scheme will always cause conditions imposed at the outlet to reflect back in the domain, explaining the dimple in the middle of the temperature profiles during the converging process. During simulations it was found that the convective outflow boundary condition will implicate the ice formation at the exit. For that, the coarse grid will obey a convective type while the fine grid a Neumann type of outflow condition. A minimum of  $N_t = 35000$  time steps are needed to fully converge the temperature such that it will not affect the simulation of ice growth.

Solidification will be initialised when the water is sub-cooled to a temperature of 271.15 K [24]. To simulate the time-lag period  $\tau$  correctly, the same is assumed in the LB model. To cover the whole domain while keeping computation time acceptable, the number of course grid points along  $y$  is set to  $N_{y,c} = 5$  followed by a layer of fine grid points  $N_{y,f} = 4$  near the wall to compensate for inaccuracies due to large grid spacing.  $N_x$  is chosen such that it covers the whole length of the copper plate:  $W = 200 \text{ mm} = \Delta x_c N_{x,c} \rightarrow N_{x,c} = 200$ . The simulation is initialised for a range of combinations of  $T_0$  and  $u_{\max,\text{in}}$  and stopped once somewhere near the edge freezing starts and  $f_l$  drops below 1. The experimental data has an absolute error of  $\pm 3 \text{ s}$  coming from uncertainties in setting  $t = 0$  when the liquid nitrogen is poured on top of the copper plate. Figure 4.10 gives a comparison between the time-lag period followed from the current LB simulation and the experimental data.

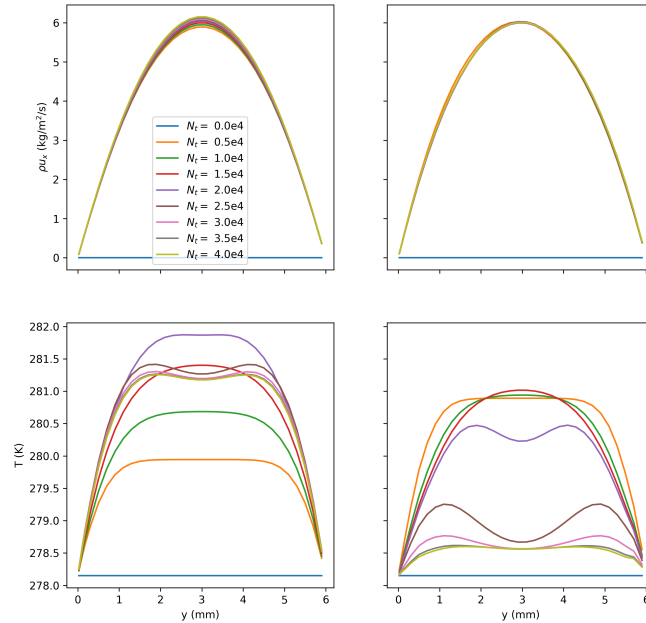


Figure 4.9: Velocity profiles (top) and temperature profiles (bottom) at the domain exit for different convergence time steps  $N_t$  and different outflow boundary conditions: (left) Neumann & (right) convective.

The values obtained by the LB simulation follow a similar curve with respect to the experimental data: increasing with inlet temperature  $T_0$ . The inlet velocity does not appear to significantly affect the observed trend and this agrees well with the experimental findings. The  $\tau$  curve found by the LB model is consistently lower than the measured values. Taking into account the error bars, the minimum deviation between the

experimental data and the simulated curve in terms of the RMSE and RRMSE is 4.9 s and 21% respectively. This discrepancy can have various reasons:

- The definition of  $\tau$  in the numerical model is now based on the **first event of  $f_l \neq 1$**  near the wall. The liquid fraction  $f_l$  is a measure to show how far the phase change process is in a computational cell. When  $f_l$  drops below 1, it reveals that the freezing process has started but not exactly where and if ice has started to form in that cell. A better condition on the liquid fraction to determine  $\tau$  would be  $f_l < 0.5$  or  $f_l = 0$ , but is deliberately not chosen as the thermal boundary condition is uncertain in that case. If the boundary condition could be determined accurately here, the adjusted conditions on  $f_l$  would increase  $\tau$  and thereby represent the experimental findings better.
- Besides the measurement uncertainty of 3 s linked to the moment liquid nitrogen is poured into the cavity, the **laser sheet position** will also influence experimental results. The time-lag period is determined when ice starts to form in the laser sheet sight. However, in the current model  $\tau$  is triggered when anywhere in the domain  $f_l \neq 1$ . This will decrease  $\tau$  with respect to measured data.
- The process of **nucleation** is not directly modelled by the present model. It forms a barrier to solidification initialisation and is taken somewhat into account by setting the freezing temperature to 271.15 K. This modification will not fully capture the actual physical process and will therefore lead to a lower  $\tau$  compared to the measurements.

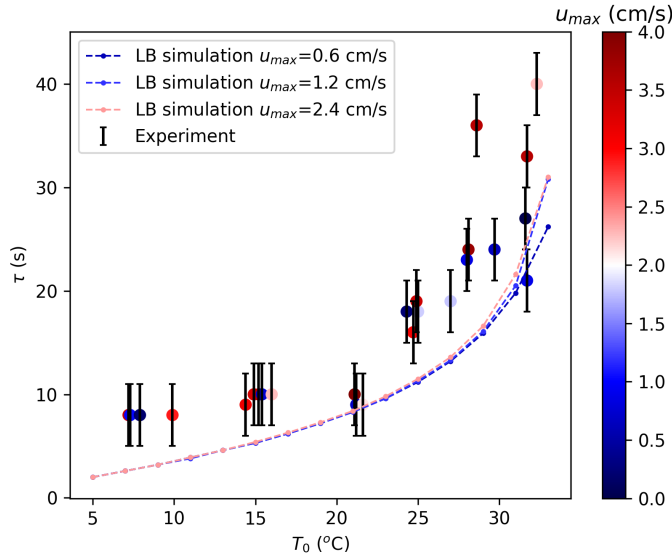


Figure 4.10: Time-lag period for various inlet water temperatures and maximum inlet velocities. The data points with errorbars are retrieved from [14]. The dotted line connects the values for  $\tau$  found by the current DDF FMLB model. The color of the data points is related to the maximum inlet velocity.

It should be noted that finding  $\tau$  through the present model is highly dependent on the definition of the temperature on the wall. The finite difference scheme determining  $T_w$  is related to  $h$  which is measured in advance and does not follow from the model directly. Moreover, because of its order of accuracy, the boundary condition is prone to truncation errors. To further proof the LB model is correct, more advanced simulations are run to find the ice growth rates  $\frac{dX_{ice}}{dt}$  and compare them to the experimental values.

A finer mesh is needed to accurately track the ice front:  $N_y = 30$ . Dimensions will not directly be taken from the experiment now, as the domain would become fairly large. For that, the dimensions along  $x$  are shortened and  $W = \Delta x N_x = \Delta x 200 = 40$  mm. An isolation layer of 2 mm at the start is added as part of the domain. The ice layer should be approximately uniform to accurately determine the ice grow rate. During simulations it is found that decreasing the channel length did not effect the ice profile uniformity and ice growth can be tracked closer to the entrance region at  $x_m = 20$  mm than was done in the experimental set-up.

After initialisation, the heat removal is imposed by (4.9). Again, the value for  $h(x)$  is taken from the experiment. This is justified as the boundary condition in (4.10), when the computational cell near the wall is

filled with ice ( $f_{i,N} = 0$ ), will determine the accuracy of the simulated ice growth. The boundary condition when this cell is (partially) filled with water ( $f_{i,N} > 0$ ), only influences the time when freezing starts but not the eventual ice grow rate. To calculate the heat flux towards the wall  $q''_{in}$  as accurate as possible, the  $\partial T/\partial y$  term is directly derived from the second term in solution vector  $\beta_k^\pm$  to avoid truncation error. Second, the thermal conductivity of ice  $\lambda_{ice}$  is made dependent on temperature. The ice growth is tracked halfway the channel at  $x_m = 20$  mm by summing the number of grid points where  $f_i = 0$  along  $y$  in time. The adaptive mesh refinement techniques will ensure high resolution in the location of the ice front. The discrete nature of tracking the ice layer with  $f_i$  will result in a stepwise increase of the ice thickness. In order to determine  $\frac{dX_{ice}}{dt}$  accurately, a minimum of 4 steps is desired. The ice growth  $\frac{dX_{ice}}{dt}$  can then be estimated by fitting a linear function through the values for ice layer thickness versus time. This procedure is performed for the three given maximum inlet velocities in combination with inlet temperatures ranging from  $T_0 = 5$  to  $30$  °C in steps of  $5$  °C. Examples of the determination of the ice grow rates are given in Appendix B. The ice grow rates for all combinations of inlet velocity and temperature are compared to experimental values in Figure 4.11.

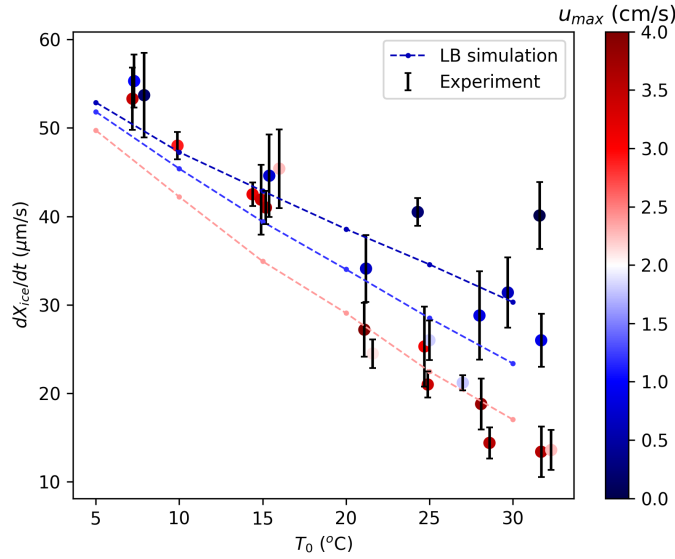


Figure 4.11: Ice growth rate  $\frac{dX_{ice}}{dt}$  for different inlet temperatures  $T_0$  and maximum inlet velocities  $u_{max,in}$ . The experimental values are given as data points with their error bars. The color corresponds to the maximum inlet velocity. The lines resemble the ice growth calculated from the LB solutions for ice thickness (Figure B.1).

From Figure B.1 it can be concluded that the model can capture the linearity in ice growth also found by [14]. The linearity in the curves is contradictory as the increasing ice thickness is expected to form an insulation layer to the cold wall, thus slowing down the ice layer growth. However, as the copper plate is continuously cooled by a constant heat flux, the wall temperature keeps decreasing resulting in an increasing temperature difference between the bulk liquid and the wall. It is this increasing temperature difference that will compensate for the growing resistance to heat transfer. These effects balance each other resulting in linear ice growth.

Both the experimental and numerical values for  $\frac{dX_{ice}}{dt}$  decrease with increasing  $T_0$ . For higher  $T_0$ , the ice surface will be in contact with higher temperatures, complicating fast solidification rates. The experimental data also suggest there is an inlet velocity dependence, becoming more significant with increasing  $T_0$ . The LB results give similar dependence on the inlet velocity as the dotted lines deviate from each other for higher  $T_0$ . Normally, higher velocity improves heat transfer and would thus lead to faster ice growth. However, there is also a faster inflow of hot water. As the ice growth decreases with increasing  $u_{max,in}$ , the characteristic freezing time in a single element is apparently smaller than the time fluid takes to flow through that element.

Qualitatively, the model shows similar dependencies on inlet temperature and velocity. The performance of the LB model is judged quantitatively by the RMSE and the RRMSE of the individual flow cases. All measured data points corresponding to an inlet velocity closest to one if the three tested cases  $u_{max,in} = 0.6, 1.2, 2.4$  cm/s are included in the calculation. Taking into account the uncertainties in the measured data, the minimum RMSE averaged over all flow cases is  $5.8 \mu\text{m/s}$ . The RRMSE per varying inlet velocity is 12%, 19% and

8.3% respectively. The RMSE is  $2.9 \mu\text{m/s}$  higher than in simulations performed by [14]. However, their simulations rely on the experimentally measured  $h_{\text{LN2}}$  and  $h$  where our model calculates the ice growth without externally measured inputs. The RRMSEs fall within the range of RRMSEs found in their simulations. As the deviation is less than 20% in every case it can be concluded that the model can predict the experimental results accurately. Most measured data points correspond to an inlet velocity closest to  $u_{\text{max,in}} = 2.4 \text{ cm/s}$ , resulting in the lowest RRMSE. The RRMSEs of the other flow cases could therefore be improved by measuring a wider range of inlet velocities and temperatures. Moreover, the uncertainties in the measured data only represent measurement errors in space and time and not the uncertainty coming from assuming linearity in the ice growth plots. There are multiple ways to define the gradient in these plots and therefore comes with a standard deviation. However, this deviation has not been included in the measurement errors. The assumed amplification of the measurement uncertainties could further decrease the RMSEs strengthening the agreement between the developed DDF FMLB model and the experimental results<sup>1</sup>. Still, there is room for improvement. Differences from trends found by ice growth measurements and their possible explanations are:

- The predicted ice grow rates in the first velocity case of  $u_{\text{max,in}} = 0.6 \text{ cm/s}$  deviate from the observed trend in the high inlet temperature measurement data. The lower predicted values can be explained with the principle of **free convection**. Free convection is intrinsically present in the freezing dynamics captured by the performed measurements and becomes more dominant with increasing Richardson number:  $Ri = Gr_H / Re_H^2$  comparing buoyancy to convective forces. In the high temperature and low velocity limit,  $Ri \gg 1$  and free convection cannot be neglected. In the current model, free convection is accounted for by the Boussinesq approximation [31]. However, it cannot capture the three dimensional effect of streamwise convection rolls modifying the velocity profiles along  $z$  [66]. The PIV measurements were taken at the centre of the section ( $z = 0 \text{ mm}$ ) so the presence of such rolls could not be detected. It is therefore not known whether these rolls are formed under freezing conditions in laminar flow. They could explain the higher measured ice grow rates in the low velocity limit as the free convection processes improve heat transfer rate.
- In the low inlet temperature region, the predicted ice grow rates are lower than the experimentally found data in all velocity cases. This could have two possible explanations: (1) the presence of **small disturbances** like plate roughness, dust or bubbles in the channel could speed up the freezing process as heat transfer is improved<sup>1</sup>. This effect will become more significant in the low  $T_0$  region as temperatures will be closer to the freezing temperature and a small boost in heat transfer could make notable difference in ice growth; (2) the profiles in Figure 4.9 indicate that the **temperature is not fully converging** to the inlet temperature. A small deviation in fluid temperature has bigger impact on freezing dynamics for low  $T_0$  than for high  $T_0$ .
- Above discrepancies could also partially be linked to experimental or numerical uncertainties in the **heat flux imposition** in (4.9). *Experimental*: so far, the heat removal has been assumed to be constant and uniform along the entire copper plate. However, time and space fluctuations in heat flux, caused by continuously refilling the top section with liquid nitrogen, are probable. This claim is further justified as an inconsistency was found by [14] in the trend of  $h_{\text{LN2}}$  compared to literature, indicating that the heat flux was not completely constant during the experiments after all. *Numerical*: In the numerical definition of the wall temperature in (4.9), the flux into the copper wall  $q''_{\text{in}}$  is taken into account. Neglecting this contribution to the changing wall temperature, would lead to a too fast drop of  $T_w$  in time. However, the model might overestimate the heat flux entering the copper wall as axial leakage might be present or a surface resistance might be felt, resulting in a slower estimated wall temperature drop.

<sup>1</sup>In correspondence with C.N. Markides, professor at Imperial College and supervisor of the experiment presented here.

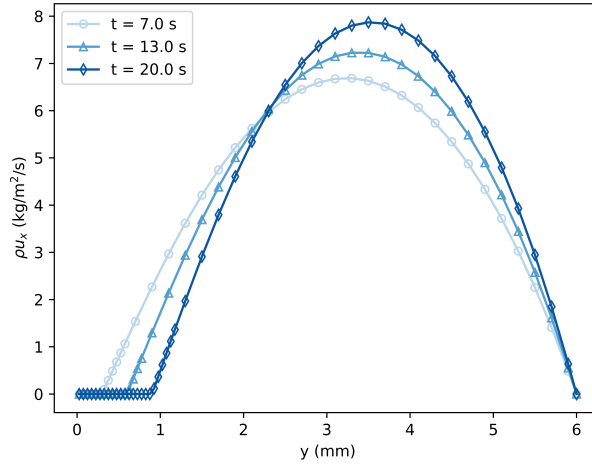


Figure 4.12: Mass flux profile tracked in time at  $x_m = 20$  mm, for  $T_0 = 5$  °C and  $u_{\max, \text{in}} = 0.6$  cm/s.

Another strong agreement between simulated and experimental results, proving the performance of the immersed boundary scheme, comes from the evolving velocity profiles under freezing. In [14], the velocity profiles are derived from PIV measurements and show that as soon as freezing is initiated, the available cross-sectional area decreases and  $u_{\max}$  increases. The profiles keep their axial symmetry, indicating that the kinematic viscosity locally dependent on temperature has little effect. Similar results are found by the current LB model (Figure 4.12). The mass flux is zero within the ice layer and is accelerated from the decreasing cross-sectional area. Also, the profiles seem to be symmetric around the centreline of the available flow area.

In order to further proof that the model can deal with a range of laminar flow cases with the presence of transient freezing, another thermal boundary is examined in the following section: the isothermally cooled wall.

### 4.2.3. Isothermal wall

The general set-up for developed flow through parallel plates that are isothermally cooled, looks like Figure 4.13. The fluid enters the cooled section with a uniform temperature  $T_0 > T_f$ . From  $x = 0$ , the wall temperature is constant and below the freezing temperature. Liquid is cooled flowing between the plates and an ice layer will form at the edges. The increasing thickness of the ice will narrow the flow area and therefore accelerate the fluid. Analytical as well as experimental results have been found for the transient ice growth. Both will be discussed and compared to the LB simulation here.

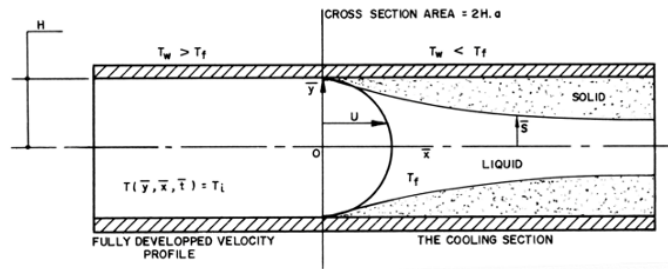


Figure 4.13: Schematic overview of the entrance of developed flow through cooled parallel plates [26].

### Analytical solution

An analytical solution for transient freezing under forced laminar flow through parallel plates is proposed in [23]. For given dimensionless time

$$\tau = FoSte = \frac{t\alpha_s}{H^2} \frac{C_{p,s}(T_f - T_w)}{L} \quad (4.11)$$

the solution for the distance between the channel centerline and the ice interface  $\tilde{\delta} = 1 - \frac{\delta}{H}$  is

$$\frac{\tau}{1 - \delta_s} = \frac{1}{2} (\tilde{\delta}^2 - 1) + (\delta_s - 1) \left[ (\tilde{\delta} - 1) + \delta_s \ln \left( \frac{\tilde{\delta} - \delta_s}{1 - \delta_s} \right) \right] \quad (4.12)$$

with  $\delta_s = \frac{f(\xi)}{f(\xi) - B}$  the steady state solution. For a fully developed velocity profile,  $f(\xi)$  is given by

$$f(\xi) = \left( \frac{\partial \theta}{\partial \tilde{y}} \right)_{y=\tilde{\delta}} = \sum_{n=0}^{\infty} c_n y'_{n(1)} \exp \left( -\frac{2}{3} \lambda_n^2 \xi \right) \quad (4.13)$$

where  $\partial \theta / \partial \tilde{y}$  is the dimensionless temperature gradient at the ice surface. Constants  $c_n y'_{n(1)}$  and  $\lambda_n$  can be found in [67].  $B = \frac{\lambda_s}{\lambda_l} \frac{T_f - T_w}{T_0 - T_f}$  is a freezing parameter. For given  $\tau = \tau_1$ ,  $\tilde{\delta}$  is found as function of  $\xi$  with (4.12). The solution to

$$\frac{d\xi}{d\tilde{x}} = \frac{1}{\tilde{\delta}}, \quad \tilde{x} = \frac{x}{H} \frac{1}{RePr} = 0, \xi = 0, \tau = \tau_1, \quad (4.14)$$

is

$$\tilde{x} = \xi \tilde{\delta} \quad (4.15)$$

and gives  $\tilde{\delta}$  as function of  $\tilde{x}$ .

### Experiment

Preliminary experimental measurements of a similar case are performed by Kaaks [27]. The experimental set-up deviates somewhat from the one assumed in Figure 4.13 when deriving the analytical solution. The original channel is cut in half and surrounded by Perspex plates. The coldplate is made of aluminium. The channel height and length are 5 and 150 cm respectively. The bottom is cooled by pumping cooling liquid (JULABO Thermal G) in counter current through 11 channels inside the aluminium wall. The resulting temperature drop in the wall is tracked in space and time by 8 thermocouples, placed 20 cm from each other in the wall. Water is pumped from a buffer vessel through the test section. In front of the channel there is a settling chamber with a combination of honeycomb grids and turbulence reduction screens to laminarise the flow and to flatten the velocity profile. Thermocouples are also present in the buffer vessel, at the inlet and outlet of the channel. Hollow glass microspheres are added to the water as tracers to perform particle image velocimetry (PIV) measurements. A lasersheet is pointing at the test section such that its light is scattered by the tracers and can be captured by a camera near the channel entrance.

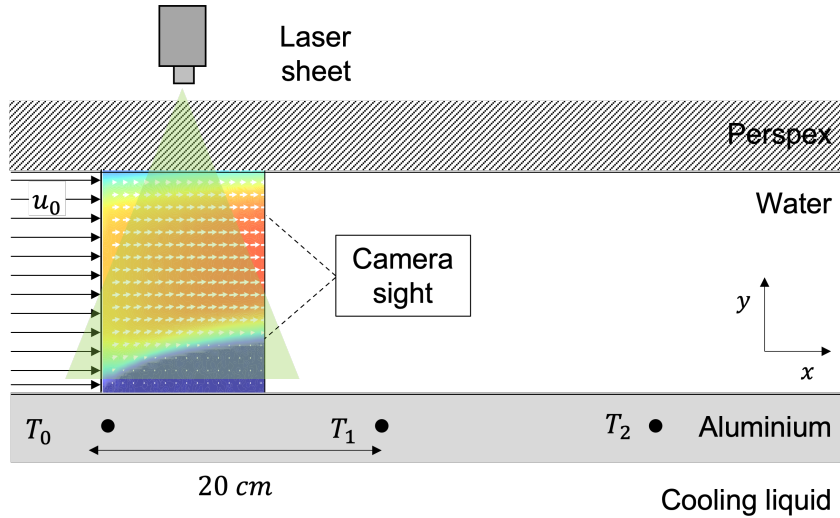


Figure 4.14: Schematic overview of the side view of the experimental set-up. The positions of the thermocouples in the aluminium wall, the simplified velocity profile and the approximate sight of the PIV camera and laser sheet are included.

Special care is taken in initialising the laminar flow and the temperature in the wall. In the previous analytical approach and also later in the numerical approach, the wall temperature can easily be assumed uniform

and  $T_w < T_f$  from  $t = 0$ . This condition is not as straightforward to achieve in the given experimental study and is approximated in the following manner: Initially, the water is pumped through the test section with a higher flow rate (1.3 L/s) and temperature (18 °C) than eventually desired. The cooling liquid will start to flow through the bottom wall. The high flow speed and temperature will ensure solidification is not initiated yet. During initialisation, the temperature in the buffer vessel is slowly cooled to the desired inlet temperature (5 °C). Once the inlet and wall temperature approach their desired values, the flow rate is dropped to 0.03 L/s, such that the flow is slowed down and reaches its desired inlet speed of 1.7 cm/s. This pre-cooling procedure takes approximately 3-4 hours. Sub-cooling due to nucleation processes is then needed to initialise freezing. The time at which this happens is set to  $t = 0$ . Hereafter, the temperature transiently drops to the desired wall temperature  $T_w = -8$  °C. Figure 4.15 illustrates the initialisation process with the temperatures measured in time by the first two thermocouples in the wall and the ones corresponding to the buffer vessel, the inlet and the outlet.

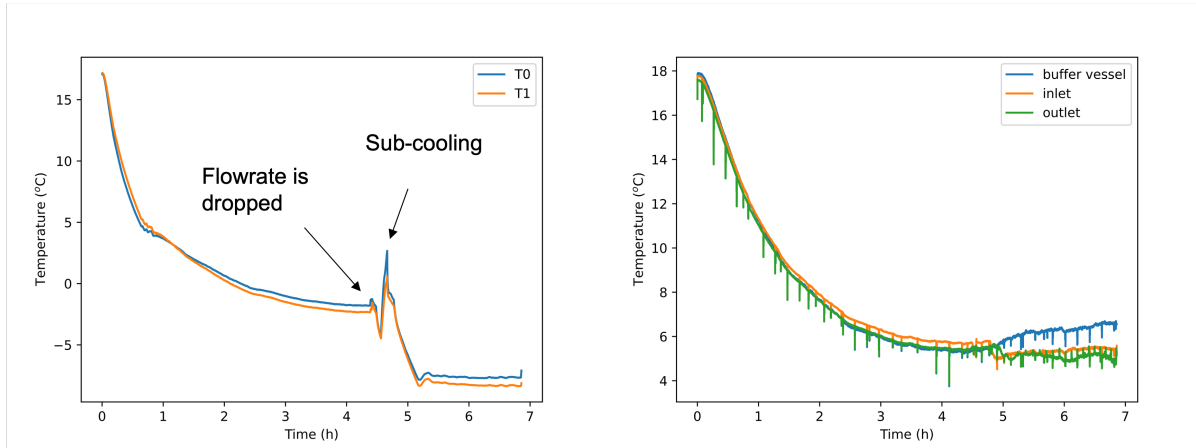


Figure 4.15: Preliminary time measurements of (left) the wall temperature in the first two thermocouples  $T_0$  and  $T_1$  and (right) the temperature in the buffer vessel, at the inlet and outlet of the channel [27].

After initialisation, the PIV measurements are started. The tracing of the particles leads to a velocity profile in the channel section covered by the laser and camera. The ice layer profile can be derived from the resulting streamplot as the velocity is zero here. Figure 4.16a is an example of the velocity and ice profile measured by the PIV method. In the next section, the preliminary results of the described experiment are tried to be obtained through simulations with the developed DDF FMLB model under similar conditions.

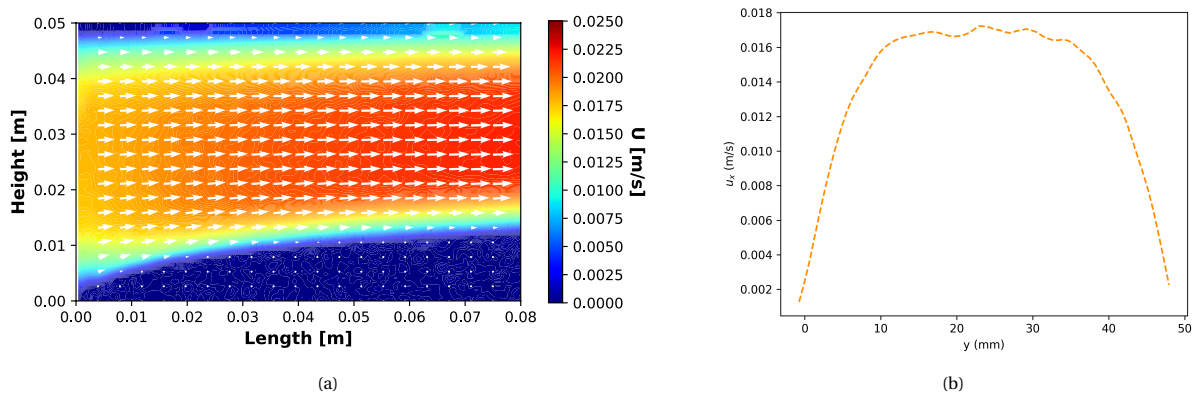


Figure 4.16: Preliminary result for the PIV measurements of the velocity profile in (a) the first 8 cm of the channel after 60 minutes of cooling and (b) the inlet at  $t = 0$  when no ice has started to form yet [27].

### Numerical model and results

The parameters that define the problem are in Table 4.6. The DDF FMLB model contains the combined transient-source term enthalpy method to deal with phase change and the enthalpy-porosity method to im-

pose a momentum sink in the ice layer. The inlet velocity and temperature are imposed with (3.39) and (3.40). The distribution functions at the outlet obey the same outlet conditions as for the previous constant heat flux case. Bounce-back boundary conditions ensure zero velocity at the wall and the anti-bounce back scheme of (3.38) ensures a uniform wall temperature  $T_w$  once the velocity profile is fully converged. The ice layer can be tracked similarly to the Stefan problem and the previous experimental test case. Again the adaptive mesh refinement technique is applied. The thermophysical properties of water and ice are again a function of temperature to approach the experimental conditions in the best possible way. Their dependencies are given in Appendix A.

Table 4.6: Physical and numerical parameter definition for forced laminar flow between cooled parallel plates

Variable	Description	Value
$W \times H$	Width and height of the channel	$8 \times 5$ cm
$N_x \times N_y$	Number of grid points	$120 \times 75$
$n$	Level of refinement	4
$A_{\text{mush}}$	Mushy constant	$10^7$ kg/m <sup>3</sup> /s
$T_0$	Initial temperature	278.15 K
$u_{\text{max,in}}$	Maximum velocity defining the Poiseuille profile	1.7 cm/s
$u_{\text{max,LB}}$	Maximum velocity in LB units to ensure stability	0.01

First, the analytical solution is laid next to the simulated and experimental ice profile for times  $t = 5$  and 10 min. For the analytical and simulated problem, the wall temperature is assumed to be uniform and constant during the runtime. This condition is not achieved during the experiment (see Figure 4.15). The mean temperatures measured in the first thermocouple until the corresponding times are given as input parameter  $T_w = 271.9$  K and 271.05 K to the analytical problem and LB simulation. The inlet velocity is assumed to be parabolic and fully developed. The analytical, numerical and experimental dimensionless ice thickness  $\frac{\delta}{H}$  as function of  $\tilde{x}$  are compared in Figure 4.17. The best fit with the analytical solution is found when the specific heat in (4.11) is replaced by an average value for water and ice:  $C_{p,av} = \frac{C_{p,s} + C_{p,l}}{2}$ . This comes from the fact that the Stefan number  $Ste$  is a measure of phase change rate. The change in ice layer thickness happens at the melting front: a moving single grid point where  $T = T_f$  and  $f_l$  lies between 0 and 1. As water and ice are both present here, the averaged specific heat gives better agreement with the analytical expression. Note that a different value than the predefined  $C_{p,ref}$  is incorporated here. This reference specific heat is introduced to capture the difference in sensible heat between the boundaries of the mushy layer  $T_l$  and  $T_s$  in non-eutectic materials. In water,  $T_l$  and  $T_s$  coincide to a single temperature  $T_f$  and  $C_{p,ref}$  is not applicable.

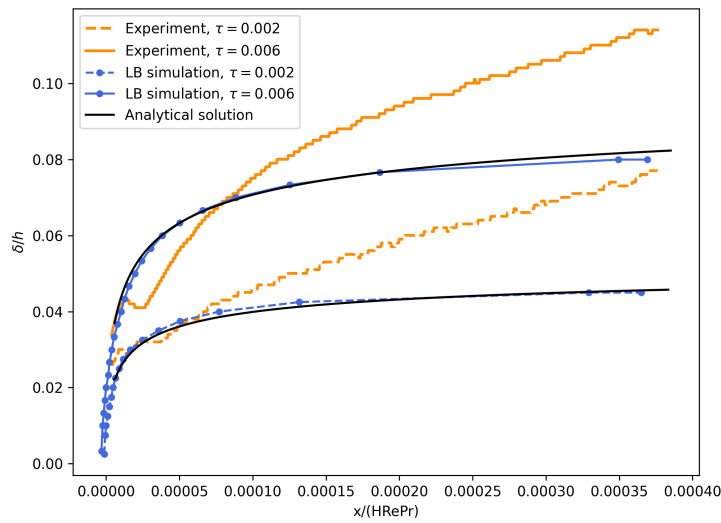


Figure 4.17: Comparison between analytical, experimental and numerical results for different dimensionless times  $\tau$ .

Table 4.7: The RMSE and RRMSE comparing the LB simulation to the analytical solution and experimental results for different dimensionless times  $\tau$ .

Metric	Analytical solution		Experimental result	
	$\tau = 0.002$	$\tau = 0.006$	$\tau = 0.002$	$\tau = 0.006$
RMSE	0.0009	0.003	0.018	0.021
RRMSE (%)	3.3	7.5	30	23

There is strong agreement between the analytical solution and the simulated ice profile. Most importantly, they converge to the same ice thickness after the entry region and are approximately flat. The quantitative deviation is again calculated by the RMSE and RRMSE, given in 4.7 for both dimensionless times. The metrics in the first column are dominated by discrepancies at the outlet (more prominent for higher  $\tau$ ). Neumann conditions are assumed at the outlet which result in a flat ice profile near the end of the channel. The analytical profile shows a small gradient at the outlet which is neglected in choosing the Neumann condition in the fine grid.

From Figure 4.17 and deviation metrics in the right column of Table 4.7 it is concluded that the analytical solution and simulated ice front do not agree well with the experimental findings. The measured ice profile is increasing along  $x$  and does not approach a constant value within the given domain. The discrepancy can most likely be related to the definition of the thermal boundary. The analytical and numerical approach assume a uniform constant wall temperature below the freezing point, a condition that is not realised in the experiment described above (see Figure 4.15). Another difference in experimental conditions comes from the velocity profile. The analytical and numerical approach assume Poiseuille flow, while the experimental set-up flattens the velocity profile. Taking into account these modifications, the numerical study is performed again to see whether results more similar to the experimental study can be obtained.

The wall temperature will become a function of space and time  $T_w \rightarrow T_w(x, t)$ . A linear interpolation is performed between temperatures measured by the first two thermocouples to estimate the profile along  $x$ . The measured temperature is tracked per second so interpolation between two successive seconds will give  $T_w(x, t)$  correctly for each time step  $\Delta t$ . The velocity in Figure 4.16b measured at the channel entrance when no ice has started to form yet, is given as inlet velocity to the LB simulation. All other parameters are kept the same as in Table 4.6. However, from Figure 4.18 it can be concluded that these adjustments do not have the wished effect on the simulated ice profile. The RMSE and RRMSE have improved with respect to imposing a uniform wall temperature but are not yet optimal.

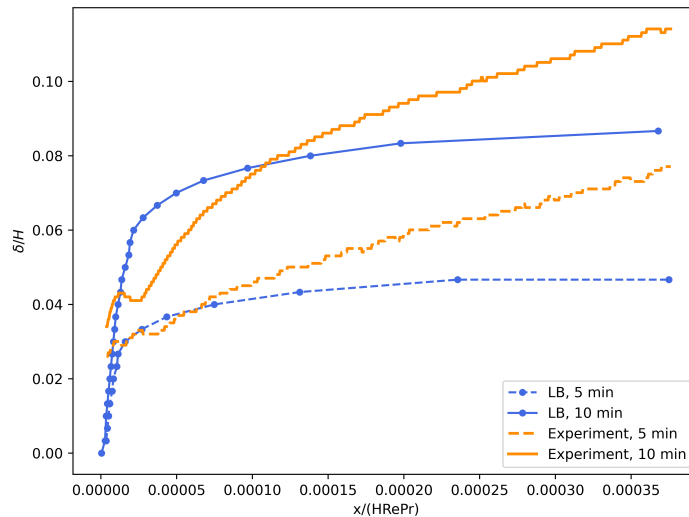


Figure 4.18: Comparison experimental and numerical results for adjusted thermal boundary and inlet velocity for different times.

Table 4.8: The RMSE and RRMSE comparing the LB simulation to the experimental results for different times.

Metric	Experimental result	
	5 min	10 min
RMSE	0.016	0.017
RRMSE (%)	26	22

The discrepancy between the simulated ice profile and the experimentally found layer may have various reasons. Either (1) the model cannot fully capture the freezing dynamics intrinsically present during the experiment or (2) the experimental set-up is not able to represent the benchmark case of uniform cooling. Arguments for both will be discussed here:

1. As we have seen in the previous section about cooling through a constant heat flux, the ice growth is influenced by the longitudinal velocity stream along the ice surface. A larger flow slows down the ice growth. The discrepancy between the numerical and experimental study might come from a **difference between the simulated and measured velocity profiles**. In Figure 4.19 the velocity profile retrieved from the LB model has a stronger acceleration at the ice surface, and thus a larger flow rate, than was measured during experiments. This could be the cause of the flattened ice profile along  $x$ . It is not well understood if this difference is the result of numerical or measurement errors.
2. The agreement between the analytical solution and the simulated ice profile is a strong argument for the second claim. Ismail and Padilha [26] found similar curves in their study to ice layer growth under super-cooling. The profiles showed a steep upward curve at the channel entrance after which the profile stayed approximately flat. Weigand and Ruß [68] compared the transient ice profiles for *convectively* and isothermally cooled plates analytically. Their profiles resulting from **convectively cooled** plates look very similar to the presented measurements. It would therefore make sense that the experiment agrees well with a convective thermal boundary definition as the aluminum wall is cooled by cooling liquid flowing through the wall. In a follow-up benchmark study, the wall temperature should be imposed by

$$T_w = T_f + \frac{(T_f - T_\infty)(H - \delta)}{\delta - H - \lambda_s/h} \quad (4.16)$$

where  $T_\infty$  and  $h$  are the temperature and heat transfer coefficient in the cooling liquid. The type of convection (counter-current, co-current, natural) is not specified in [68] and must thus be intrinsically present in  $h$ . To correctly estimate  $h$ , it should either be found iteratively by trying multiple values of  $h$  in the analytical solution of [68] and see which best fit the measured ice profiles, or be found experimentally. In general it can be said that the LB simulations are **sensitive to the definition of the temperature on the wall**. As the spatial resolution in the measured wall temperature is extremely low, it is uncertain whether the wall temperature is approximately uniform in the first 8 cm or that the wall temperature profile along  $x$  looks completely different. Moreover, as the thermocouples are placed in the middle of the aluminum wall, it is uncertain what the temperature will be at the contact surface. Especially in the first half hour, the wall temperature is close to the freezing temperature. Therefore small errors in measuring  $T_w$  or in the definition of  $T_w$  at the contact surface could already lead to significant differences in the formed ice layer. A solution might be to work with **lower wall temperatures** as was done in the super-cooling case of [26] to decrease the impact of errors in the wall temperature. Another possibility is to benchmark the model only for **long measurement times** (>60 min) as the measured wall temperature is further away from the freezing temperature then, although it is not certain if the model will definitely converge to the measured profile there. However, this is not a desirable solution as it would increase computation time to the order of days. A third solution could be to measure the ice thickness **further away from the channel entrance**. Measurements might converge to an approximately uniform profile here approaching the analytical and numerical solutions. Also, when the ice profile is uniform, a better estimation on the ice thickness growth versus time can be made, serving as an extra way to benchmark simulations (just as was done by finding  $dX_{ice}/dt$  in 4.2.2).

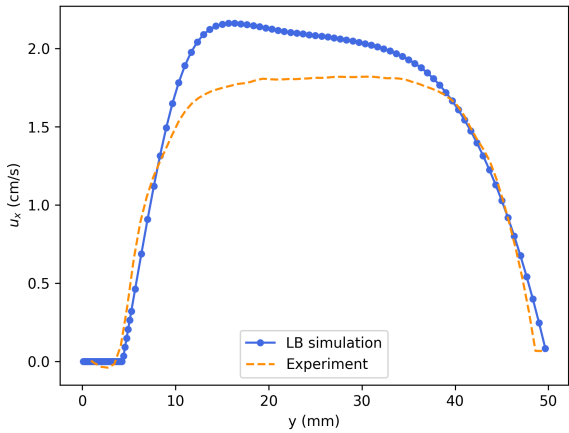


Figure 4.19: Velocity profile along  $y$  at  $x = 6.6$  cm and  $t = 10$  min found by LB simulation (solid line) and experiment (dotted line).

# 5

## Molten salt: Non-eutectic vs. Eutectic

Phase change processes in eutectic mixtures are practically the same as those of pure substances. However, molten salts are typically non-eutectic of nature, described by a pseudo-binary system. A small portion of uranium fluoride  $UF_4$  (2-3%) is dissolved in the eutectic  $LiF$ - $ThF_4$  (77.5% - 22.5%) mixture. The phase-diagram in Figure 5.1 visualises this composition. The addition of  $UF_4$  will move the system away from its eutectic point. The two intersections with the vertical line represent the liquidus and solidus temperatures  $T_l$  and  $T_s$ . For a temperature  $T > T_l$ , there is only liquid solution. Lowering the temperature to  $T_s < T < T_l$ , we enter the mushy region  $\epsilon = T_l - T_s$ . Here,  $LiF$  will solidify, while  $Li_3(Th,U)F_7$  stays melted such that two phases coexist. Dropping the temperature further to  $T < T_s$ , also the  $Li_3(Th,U)F_7$  composition will solidify, making the substance completely solid.

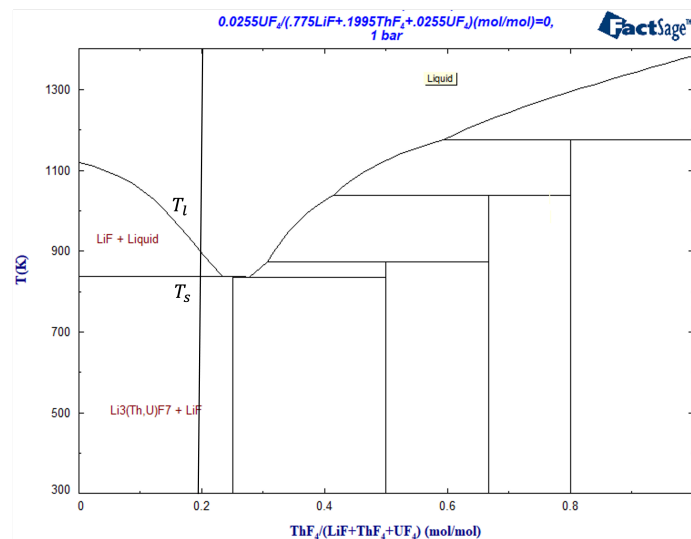


Figure 5.1: Visualization of  $LiF$ - $ThF_4$ - $UF_4$  (77.5-19.95-2.55%) as a pseudo-binary system [69]

The consistency of the molten salt in the mushy region will be comparable to ice slurry and the flow will become non-Newtonian of nature. Adjustments to the build DDF FMLB model should be made as it has only dealt with eutectic solutions in which this mushy region does not exist. These adjustments are explained and verified in 5.1. Hereafter, the effect of the mushy layer on thermal flow properties is tested by comparing the velocity, temperature and ice profile, the pressure drop and the Nusselt relation under freezing for non-eutectic and eutectic molten salts in 5.2.

### 5.1. Mushy layer treatment

The mushy region will be generated automatically when  $\epsilon > 0$  is imposed. Once the cooling starts, a layer where the liquid fraction lies between 0 and 1 will naturally rise for calculated temperatures between  $T_s$  and

$T_l$ . It is expected that the presence of the solid particles in the mushy region will slow down the suspension. In 3.2.3 two methods were introduced that were able to ensure a no-slip condition on the moving phase interface. They have been proven to work for sharp (i.e. one computational cell thick) solid-liquid interfaces. The enthalpy-porosity method has been used multiple times to simulate mushy regions [56, 70]. However, to the best of our knowledge, no literature is found on applying the immersed boundary scheme on non-eutectic materials. Since the modification on its collision operation is highly dependent on  $f_l$ , there is reason to believe this method will also be applicable to deal with momentum sink in the mushy region. Both methods will be tested and compared throughout the rest of this section.

Not only the flow profile is affected. Section 2.2.2 suggested that special care should be taken in defining the thermophysical properties inside the mushy region. As the thermal diffusivity and kinematic viscosity determine the translation between solution vectors  $\alpha_k^\pm$  and  $\beta_k^\pm$  through  $G$  and  $\bar{G}$  in DDF FMLB models, estimations of their behaviour in the mushy region should be made precisely. The analogy of [70] is followed to find the thermal diffusivity in the mushy region. The suggestion of [56] to modify the viscosity is also adopted. Both methods and their implementation in the present DDF FMLB model will be explained and derived here.

Thermal conductivity  $\lambda_{m,\gamma}$  in movable ice slurry is dependent on shear rate  $\dot{\gamma}$  and larger than values determined for non-movable slurries  $\lambda_m$ . Slurries that are in motion combine mixture convection with a micro-convection effect due to the presence of solid particles, intensifying the heat transfer process. The resulting thermal conductivity can be defined as

$$\frac{\lambda_{m,\gamma}}{\lambda_m} = \begin{cases} 1 + 3(1 - f_l)Pe^{1.5} & Pe < 0.67 \\ 1 + 1.8(1 - f_l)Pe^{0.8} & 0.67 \leq Pe \leq 250 \\ 1 + 3(1 - f_l)Pe^{1/11} & Pe > 250 \end{cases} \quad (5.1)$$

where  $\lambda_m$  is determined by the Maxwell-Tareff dependence [71]

$$\lambda_m = \lambda_l \left[ \frac{2\lambda_l + \lambda_s - 2(1 - f_l)(\lambda_l - \lambda_s)}{2\lambda_l + \lambda_s + (1 - f_l)(\lambda_l - \lambda_s)} \right]. \quad (5.2)$$

The Peclet number for movable ice slurry depends on average ice crystal diameter  $d_s$ , thermal diffusivity of the carrier fluid  $\alpha_l$  and shear rate  $\dot{\gamma}$ . The last follows from the rate of strain tensor  $E$ :

$$Pe = \dot{\gamma} \frac{d_s^2}{\alpha_l} \quad (5.3)$$

$$\dot{\gamma} = \sqrt{2E_{ij}E_{ji}} \quad (5.4)$$

$$E_{ij} = \frac{1}{2} (\partial_i u_j + \partial_j u_i) \quad (5.5)$$

The gradients in this tensor are retrieved from terms  $\alpha_{3,4,5}$  in the solution vector. Once the local thermal conductivity in the moving slurry is found following the procedure above, the thermal diffusivity  $\alpha_m = \frac{\lambda_{m,\gamma}}{C_{p,m}\rho_m}$  can be implemented in LB units in  $\bar{G}$ . The specific heat and density in the mushy zone are calculated by a weighted mean over the properties of the two phases:

$$C_{p,m}\rho_m = f_l C_{p,l}\rho_l + (1 - f_l) C_{p,s}\rho_s. \quad (5.6)$$

The viscosity in moving ice slurry in [70] is assumed to be that of a Herschell–Buckley liquid with consistency index and yield shear stress highly dependent on material properties. We are looking for a more general procedure and therefore the equations suggested in [72] are applied to find the kinematic viscosity  $\nu_m$  in the mushy region:

$$\nu_m = \begin{cases} \nu_l (1 + 2.5(1 - f_l) + 14.4(1 - f_l)^2) & f_l > 0.8 \\ \nu_l (1 + 2.5(1 - f_l) + 10.05(1 - f_l)^2 + 0.00273e^{16.6(1 - f_l)}) & f_l < 0.8 \end{cases} \quad (5.7)$$

In order to verify the above parameter implementation, results for heat transfer coefficients as function of liquid fraction in ice slurry are compared with literature. In the next sections, the experiment of ice slurry flow through a channel heated from both sides and the numerical model with equivalent conditions are explained. Hereafter, results are given and discussed.

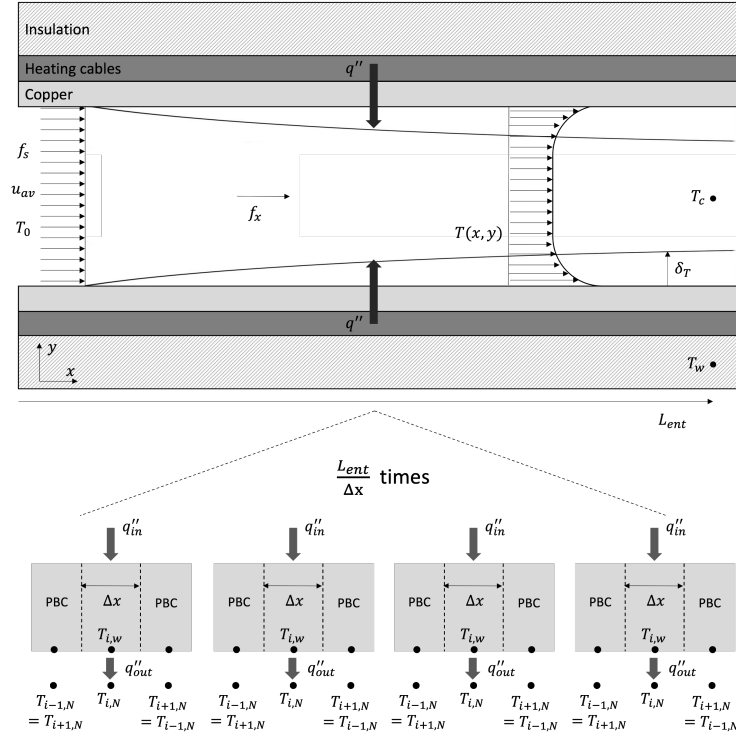


Figure 5.2: Schematic overview of (top) ice slurry flow containing ice fraction  $f_s$  at inlet temperature  $T_0$ , pushed through a rectangular duct by body force  $f_x$  resulting in average velocity  $u_{av}$ . The walls are heated by a heat flux generated through heating cables. The temperature profile and definition of  $\delta_T$  is also given. The wall and core temperature measurements are taken at  $L_{ent}$  with thermocouples  $T_w$  and  $T_c$ . The translation to a numerical model is visualised by repetition of the top part of the channel (bottom).

### Experiment

Nieżgoda-Żelasko performed several experiments [70, 73] on heat transfer in ice slurry flows. The objective of these studies was to find the heat transfer coefficient as function of velocity, ice fraction and pipe geometry. The ice slurry is created by dissolving 10.6% ethanol in water. The resulting mixture will not melt or freeze at a single temperature as pure water would but follows a phase change trajectory. Between  $T_l$  and  $T_s$ , the substance becomes an ice slurry where solid particles coexist with the liquid carrier fluid. Ice slurries of different ice fractions  $f_s$  are prepared and flowed through a test section which is heated with a constant heat flux  $q''$ . The received heat induces ice melting, a temperature increase in the substance and mixing of the solution. During the experiments, the mean temperature of the medium has increased with a maximum of 0.6 K corresponding to a 3% change in ice fraction. For that, the effect of mixing is neglected. The heat transfer coefficient is found by

$$h = \frac{q''}{T_w - T_c} \quad (5.8)$$

where  $T_w$  and  $T_c$  are measured by thermocouples in the wall and core of the test section. Measurements are performed for varying flow parameters:

- copper tubes (dimensions:  $d_i = 0.01, 0.016, 0.02$  m,  $L = 4.6$  m); rectangular tubes (dimensions:  $0.0078 \times 0.0265 \times 3.0$  m,  $0.003 \times 0.0358 \times 2.0$  m)
- mean flow velocities  $0.1 \leq u_{av} \leq 4.5$  m/s
- heat flux  $q'' = 2000, 5000, 8000$  W/m<sup>2</sup>
- ice fractions  $0 \leq f_s \leq 30\%$ , with an average ice crystal size (width-length) of  $d_s = 0.1\text{--}0.15$  mm.

The measurements range from the laminar to the turbulent region. Only the results for laminar flow are analysed here. The found dependence of  $h$  on  $f_s$  is an increasing one and is more distinct in the laminar region.

### Numerical model

Measurements were taken at thermal entry length  $L_{ent}$ , where the heat transfer coefficient is assumed to be practically constant and the flow is hydrodynamically fully developed. Developed thermal flow can efficiently be simulated by assuming periodic boundary conditions (PBC) at the beginning and end of the domain. The system size along  $x$  can therefore be reduced to a single node. A constant heat flux is imposed on the top and bottom wall. As solid particles coexist with the carrier liquid, both conductive and convective heat transfer processes are present. The flux boundary condition like proposed in 4.2.2 is therefore not completely correct in this case, although a similar approach can be followed. The heat flux  $q''_{in}$  is generated in the heating cables. The heat flux moving away from the wall  $q''_{out}$  comes from mixed convection and conduction effects caused by the presence of moving particles. The overall thermal conductivity is thereby enhanced according to (5.1). For that, the adjusted finite difference scheme to estimate the wall temperature is

$$\rho_w C_{p,w} \Delta x d \frac{T_{i,w}^{n+1} - T_{i,w}^n}{\Delta t} = q''_{in} + \lambda_{m,\gamma} \left. \frac{\partial T}{\partial y} \right|_{y=N} \quad (5.9)$$

The  $\frac{\partial T}{\partial y}$  can again directly be derived from the third term in solution vector  $\beta_k^\pm$ . It is likely the  $T_w$  found through this procedure will deviate from the actual wall temperature due to made assumptions and approximations. The finite difference scheme comes with truncation errors, the heat flux away from the wall is based on an estimation of the conductivity and axial conduction is not taken into account because of the one-dimensionality of the domain. The procedure is sufficient to impose an estimated wall temperature but using (5.8) with the estimated  $T_w$  to find  $h$  would become unreliable. A different approach to estimate the heat transfer coefficient is through the thermal boundary layer  $\delta_T$  where flow is characterised by its temperature gradient. Heat transfer inside the thermal boundary layer is dominated by conduction. The heat transfer coefficient can thus be estimated by

$$h = \frac{-\lambda_{m,\gamma} \partial T / \partial y|_{y=N}}{T_w - T_0} \approx \frac{\lambda_{m,\gamma}}{\delta_T}. \quad (5.10)$$

The thermal boundary layer will be measured from temperature profile plots. Deviations from the measured heat transfer coefficients can now be fully related to measurement errors in  $\delta_T$ . Uncertainties in the estimated  $T_w$  of (5.9) are much harder to define and therefore it is preferred to find  $h$  through  $\delta_T$ .

Flow is induced by a body force  $f_x$  which is adjusted to ice fraction  $f_s = 1 - f_l$  to consistently reach an average velocity of  $u_{av}$  through every simulation; i.e. slurry containing large ice fraction needs more force to be moved. It is not known beforehand what body force is needed to reach the desired velocity and is thus found on a trial and error basis. Both the immersed boundary and enthalpy-porosity method will be tested to deal with slug flow in slurry ice. The liquidus temperature  $T_l$  for a 10.6% ethanol solution is known. The numerical solidus temperature  $T_s$  will each time be determined from (2.14) such that the liquid fraction corresponds to the experimental parameter  $f_l = 1 - f_s$  with  $T = T_0$ :

$$T_s = \frac{T_0 - f_l T_l}{1 - f_l}. \quad (5.11)$$

The corresponding enthalpies are then calculated with

$$H_s = C_{p,s} T_s \quad (5.12)$$

$$H_l = H_s + C_{p,ref} (T_l - T_s) + L. \quad (5.13)$$

It is important to note that the *reference specific heat*  $C_{p,ref}$  only affects the definition of  $H_l$  and of the boundary condition (3.38). The *local specific heat* to determine  $\alpha_m$  will be correlated to phase and temperature through the weighted mean of (5.6). The specific heat in the fully liquid carrier fluid ( $C_{p,cl}$ ) and solid ( $C_{p,s}$ ) region are a function of temperature and can be found in Appendix A. The thermal diffusivity and kinematic viscosity are defined locally by the procedure explained before. Other physical properties and numerical parameters are summarised in Table 5.1.

Table 5.1: Physical and numerical parameter definition for ice slurry flow between parallel plates

Variable	Description	Value
$H$	Height of the channel	7.8 mm
$N_y$	Number of grid points	15
$u_{av}$	Average velocity	0.25 m/s
$C_u$	Velocity conversion factor	5
$q_{in}$	Heat flux into the domain	8 kW/m <sup>2</sup>
$T_0$	Inlet temperature	267 K
$T_l$	Liquidus temperature	268.39 K
$L_{ent}$	Thermal entry length	1.5 m
$d$	Wall thickness	3 mm
$\rho_{car}$	Density carrier liquid	981.84 kg/m <sup>3</sup>

Approximately 50000 iterations are needed to fully converge the velocity profile such that it becomes stationary. After initialisation of the velocity profile, the walls are heated by imposing (5.9) and another  $\frac{L_{ent}}{\Delta x}$  iterations are needed to exactly match the location where measurements are taken (visualised in the bottom of Figure 5.2). This procedure to efficiently cover the entire domain is justified by (1) the given condition that the ice fraction will not vary more than 3% along  $x$ , (2) the fully developed flow profile and (3) the assumption that the thermal boundary layer is smoothly increasing along  $x$ . Local shear rate will give the thermal conductivity in the thermal boundary layer through (5.1) and plots of the temperature profile will determine the thickness of  $\delta_T$ , following the definition given in the top of Figure 5.2. Together they will lead to the heat transfer coefficient  $h$  with (5.10).

### Comparison of results

Both the immersed boundary and enthalpy-porosity method are tested for ice fractions  $f_s$  ranging from 5 to 25%. Recommendations of [74] are followed to define values for: (1) the mushy constant  $A_{mush} = 10^7$  kg/m<sup>3</sup>/s, introduced in (3.33) and (2) the small constant  $\varepsilon = 0.001$  in (3.29). The body force  $f_x$  is found iteratively on a trial and error basis to ensure an average velocity of  $u_{av} = 0.25$  m/s in every case of  $f_s$ . The resulting values are summarised in Table 5.2. The temperature profiles at the thermal entry length and the fully developed velocity profiles are given for both methods in Figure 5.4. The widths of the thermal boundary layers are determined from the temperature profile plots and are given in Table 5.2 as well. As the temperature profile is discretised in space, determining the position of  $\delta_T$  comes with an error equal to the width of a computational cell. The resulting heat transfer coefficients are visualised in Figure 5.3. A couple of remarks can be made on the results:

- The methods give similar heat transfer coefficients in the low ice friction region. For higher ice fractions (>15%) the results start to deviate as the thermal conductivities are lower for the immersed boundary scheme than for the enthalpy-porosity method. This is attributed to the differences in velocity profiles. The thermal conductivity of moving ice slurry is dependent on shear rate. Shear rate is related to the velocity gradient and in Figure 5.4 the profiles for the immersed boundary method are indeed less steep. Nonetheless, **both methods show strong agreement with experimental data**. The weighted mean of simulation results by the enthalpy-porosity and immersed boundary scheme deviate 8.2% and 5.8% respectively from the weighted mean of the experimental heat transfer coefficients, an improvement with respect to [75] where the deviation between simulated  $h$  and measurements rose up to 22%.
- The simulations can **well capture the non-linear relationship between  $f_s$  and  $h$** . This non-linearity is expected as, especially at high ice fractions  $f_s > 10\%$ , ice slurry behaves like a Bingham's fluid in which particles do not mix well. Heat transfer processes will not be further improved by the mixed conduction and convection effects caused by the coexistence of solid particles with the carrier fluid, explaining the decreasing trend near higher ice fractions in Figure 5.3<sup>1</sup>.

<sup>1</sup>In correspondence with Beata Niezgodna-Żelasko, responsible for experiments published in [70, 73]

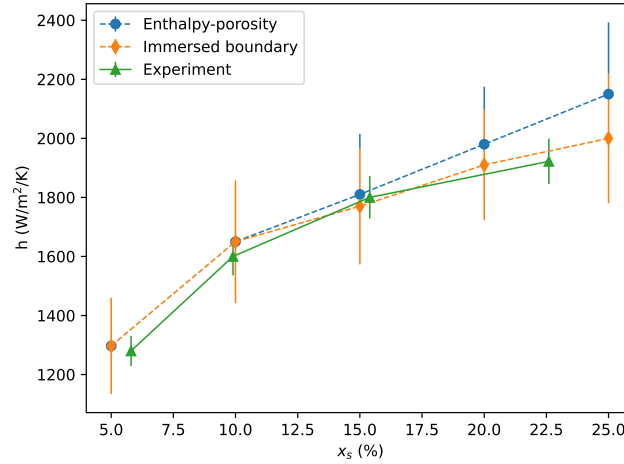


Figure 5.3: Heat transfer coefficient as function of ice fraction calculated by the enthalpy-porosity and the immersed boundary method. The experimental values found by [73] are also given as reference.

Table 5.2: Numerical results for the enthalpy-porosity and immersed boundary method

Enthalpy-porosity				Immersed boundary		
$f_s$ (%)	$f_x$ (kN/m <sup>2</sup> )	$\lambda_{m,u \neq 0}$ (W/m/K)	$\delta_T$ (mm)	$f_x$ (kN/m <sup>2</sup> )	$\lambda_{m,u \neq 0}$ (W/m/K)	$\delta_T$ (mm)
5	2.1	0.59	$0.46 \pm 0.07$	3.2	0.59	$0.46 \pm 0.07$
10	6.3	0.75	$0.46 \pm 0.07$	5.3	0.75	$0.46 \pm 0.07$
15	12.6	0.94	$0.52 \pm 0.07$	6.3	0.92	$0.52 \pm 0.07$
20	21.0	1.16	$0.59 \pm 0.07$	6.7	1.12	$0.59 \pm 0.07$
25	31.5	1.4	$0.65 \pm 0.07$	6.9	1.3	$0.65 \pm 0.07$

- The enthalpy-porosity velocity profiles approach the parabola shape for low ice fraction and the point at which the velocity is cut off moves to the middle with decreasing  $f_s$ . The velocity profiles obtained by the immersed boundary method do not seem to change significantly for different ice fractions. The cut off point stays approximately the same and the profiles are not converging to a parabola shape for decreasing ice fraction. This could indicate that the enthalpy-porosity method might better capture the non-Newtonian behaviour of the ice slurry. However, **no direct conclusion can be drawn on which method performs better** based on these qualitative arguments. Further study is needed to quantitatively compare the velocity profiles obtained by the enthalpy-porosity and immersed boundary method to experimental or analytical solutions of non-Newtonian fluids.

It can be concluded that the adjustments on thermal diffusivity and kinematic viscosity have resulted in correct simulation of heat transfer process in the mushy region for low ice fraction. No benchmark case is tested for higher ice fraction so it is uncertain whether the model will also be correct in that part of the mushy region. Looking at the trend in Figure 5.3 it is expected heat transfer might too be over estimated.

Based on no significant difference in efficiency and a first indication that the enthalpy-porosity method could outperform the immersed boundary scheme in treatment of the non-Newtonian behaviour present in the mushy region, the enthalpy-porosity method will be applied in the numerical model for simulating molten salt flow.

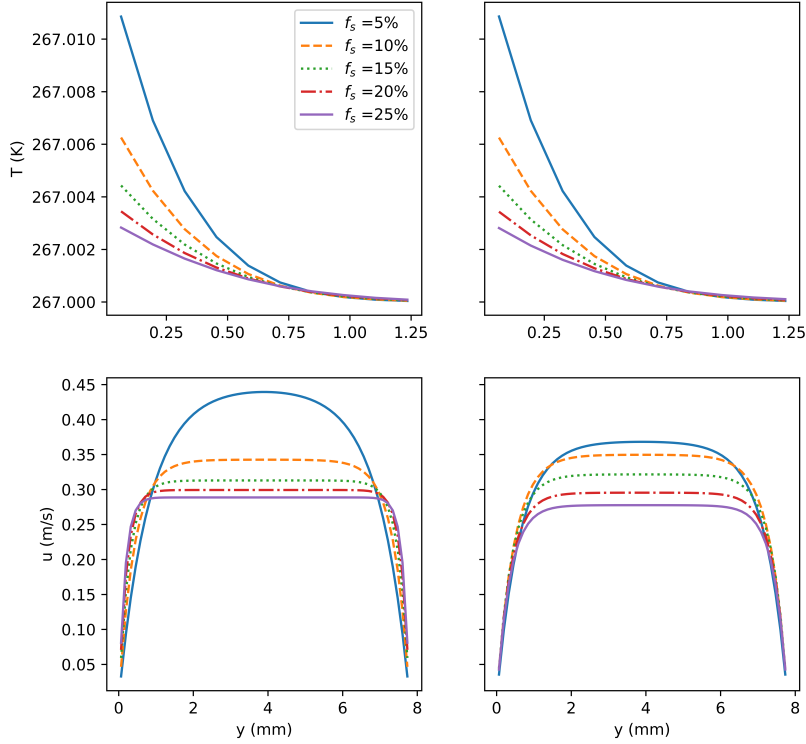


Figure 5.4: Top: temperature profile along  $y$  near the wall for different ice fractions. Bottom: velocity profiles along  $y$  for different ice fractions. Left: enthalpy-porosity method. Right: immersed boundary method.

## 5.2. Effect of mushy layer on thermal flow properties

A DDF FMLB model containing the source-based enthalpy method to deal with phase change, the enthalpy-porosity method to impose a momentum sink in both the solid and mushy region, local thermophysical properties in the solid, mushy and liquid region and adaptive mesh refinement techniques has all the components to simulate freezing in molten salts both accurately and efficiently. Throughout this section, the described model will simulate laminar molten salt flow through a parallel plate geometry that is isothermally cooled from one side. Flow is induced by imposing a Poiseuille velocity profile with  $u_{\max}$  and temperature  $T_0$  at the inlet. The bottom plate is cooled by an isotherm wall with  $T_w < T_s$ . The outflow is modeled by the Neumann condition in the fine grid and by the convective condition in the coarse grid. Once grid points with  $f_l < 1$  come too close to the coarse-fine grid interface, adaptive mesh refinement is triggered. Data on thermophysical properties of molten salts is limited as high temperature and corrosive characteristics of molten fluorides, make experiments complicated. The available experiments are in general only performed on pure salts or binary mixtures at the eutectic composition. The model build so far is able to deal with locally dependent specific heat, thermal diffusivity and kinematic viscosity. However, better data on these properties must be found for non-eutectic molten salts, either experimentally or numerically, to make optimal use of this feature. The parameters that do have temperature dependence are given in Appendix A. Constant physical parameters and LB parameters defining the numerical set-up are summarised in Table 5.3 and are used throughout this section to find the effect on heat transfer mechanisms of non-eutectic salts compared to eutectic salts. The wall and inlet temperatures together with the inlet velocity are not given here as they will be varied to find their dependencies on the mushy layer.

Table 5.3: Physical and numerical parameter definition for non-eutectic and eutectic molten salt flow between parallel plates

Variable	Description	Value
$W \times H$	Length and height of the channel	$33 \times 10$ mm
$N_x \times N_y$	Number of grid points	$100 \times 30$
$n$	Level of refinement	4
$A_{\text{mush}}$	Mushy constant	$10^8$ kg/m <sup>3</sup> /s
$T_l$	Liquidus temperature	838 K [76]
$T_s$	Solidus temperature	825 K [76]
$T_f$	Freezing temperature	827 K [77]
$L$	Latent heat (non-eutectic / eutectic)	179 / 111 kJ/kg [76][77]
$\rho$	Density	3500 kg/m <sup>3</sup> [76]
$C_{p,l/s}$	Specific heat (liquid / solid)	276 / 198 J/kg [76][78]
$\lambda_l$	Thermal conductivity (liquid)	1.1 W/m/K [79]
$\alpha_l$	Thermal diffusivity	1.2 mm <sup>2</sup> /s

The following study will search for the effect of the presence of a mushy layer on heat transfer processes. Previous research has been performed on the evolution of the mushy zone, however not in the presence of a convective flow [30, 56, 35]. The composition of the non-eutectic salt has been described in the introduction of this chapter. The eutectic salt assumed in this study is the binary system LiF-Th4 (75%-25%). To only test the effect of the mushy region, the thermophysical properties are kept constant for the non-eutectic and eutectic salt. The difference will come from the assumption of a liquidus and solidus temperature in the non-eutectic case, and a freezing temperature in the eutectic case. Consequently, the latent heat is also modified as it will require more heat removal to go from liquid to solid composition in non-eutectic salts.

Figure 5.5 gives an impression of where differences in thermal flow properties between non-eutectic and eutectic mixtures come from. The liquid fraction for different times is given in the first 8 mm of the domain under cooling with  $T_w = 790$  K in a channel where  $T_0 = 842$  K and the molten salt flows with  $u_{\text{max,in}} = 2.0$  cm/s. The mushy zone is clearly visible in 5.5 as there are multiple layers present where  $0 < f_l < 1$ . Both the solid region as the mushy zone width are increasing with time. The salt augmentation in the eutectic case has a thickness similar to the solid region in the non-eutectic case for all times. Also the discrete nature of tracking the phase interface with  $f_l$  is visible by the stepwise increase of the solid salt layer along  $x$ .

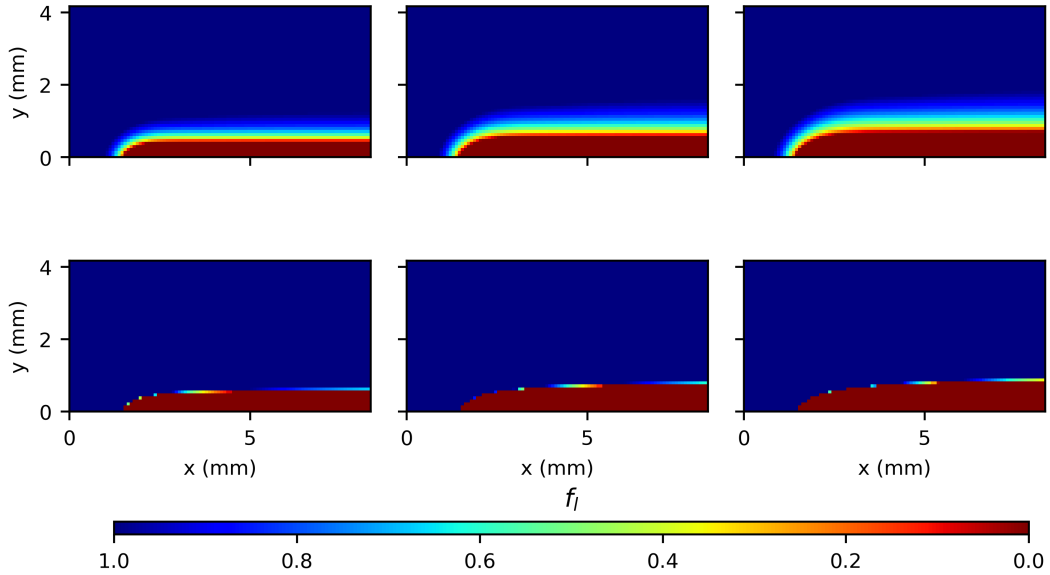


Figure 5.5: The local liquid fraction  $f_l$  in the first 8 mm of the domain for different times  $t = 10, 20, 30$  s. The results of the non-eutectic salt are in the top figure and eutectic in the bottom. The inlet velocity, inlet and wall temperature are  $u_{\text{max,in}} = 2$  cm/s,  $T_0 = 842$  K and  $T_w = 790$  K for both cases.

### 5.2.1. Velocity & temperature dependence

Figure 5.6 gives the temperature and velocity distributions along  $y$  at the center of the channel  $x = W/2$ . With time, the ice layer expands causing the profiles to shift to the right. The effect of the presence of a mushy layer is visible in both the temperature as the velocity profile:

- In the top left figure, the **temperature** gradually passes the phase interface, whereas in the eutectic salt (top right), there is a sharp transition in the temperature profile on the phase interface, similar to the Stefan problem. The temperature gradient  $\partial T/\partial y$  in the mushy region appears to be steeper than in the liquid region of the eutectic salt. From section 5.1 it followed that the thermal conductivity in moving ice slurries is larger than its value in the carrier fluid without the presence of solid particles. Together with the steeper temperature gradient it indicates that the heat flux is higher than it would be in the absence of a mushy layer.
- A larger part of the domain along  $y$  is covered by a region where the **velocity**  $u \sim 0$  in the non-eutectic salt compared to the eutectic salt. This is a results of the drag coming from the partly frozen molten salt. The momentum sink appears to already be significant in the low liquid region (right above the fully frozen layer). In the higher liquid region, the velocity gradually increases, rather than a sharp transition in the absence of a mushy layer. The presence of a mushy layer also seems to have significant effect on fluid acceleration. The maximum velocity in non-eutectic flow increases with  $\sim 10\%$  compared to eutectic flows since the region where  $f_l < 1$ , takes up more space here than in eutectic transient freezing.

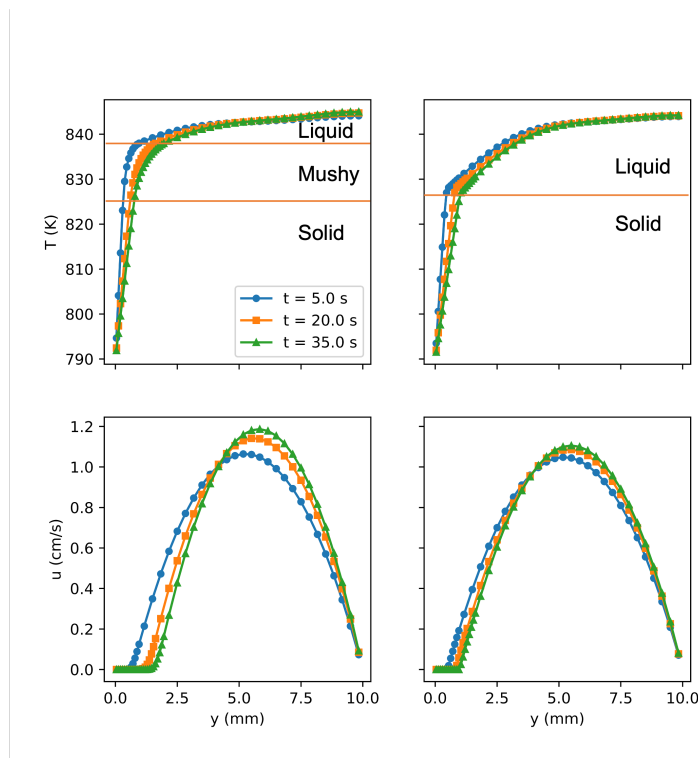


Figure 5.6: The temperature (top) and velocity (bottom) profile of non-eutectic (left) and eutectic (right) molten salts for different times at  $x = W/2$ .  $T_w = 790$  K,  $T_0 = 842$  K and  $u_{\max, \text{in}} = 1$  cm/s. The horizontal lines in the top figures represent the solidus and liquidus temperatures for non-eutectic and freezing temperature for eutectic composition.

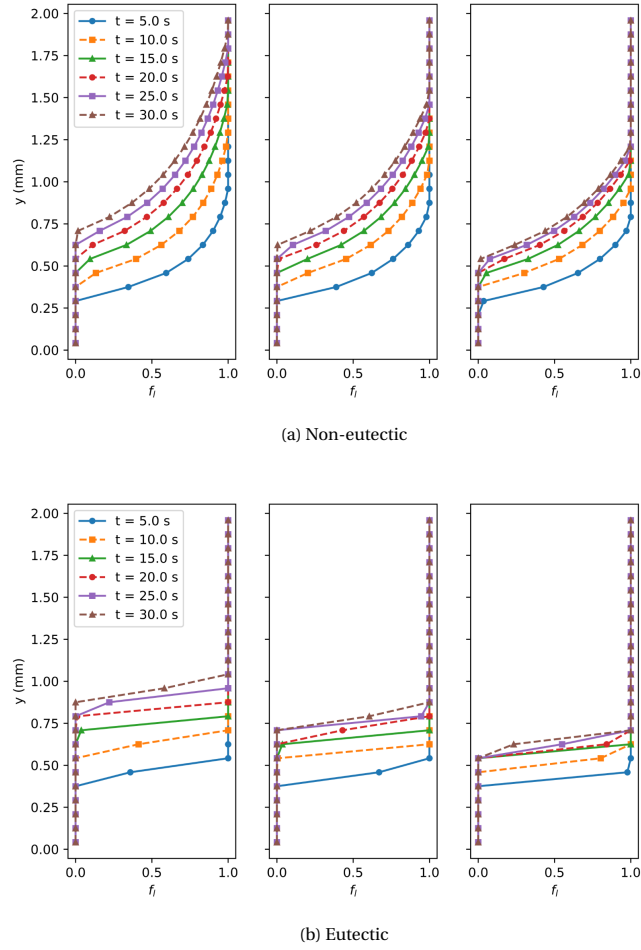


Figure 5.7: The liquid fraction  $f_l$  at  $x = W/2$  in terms of channel height at different inlet velocity magnitudes  $u_{\max, \text{in}} = 1, 2, 3$  cm/s. The inlet velocity increases from left to right. The results of the non-eutectic salt are in the top figure and eutectic in the bottom. The inlet and wall temperature are  $T_0 = 842$  K and  $T_w = 790$  K everywhere.

Figure 5.6 shows the effect of the existence of a mushy layer on velocity and temperature. We are also interested in the influence of velocity and temperature on the evolution of the mushy layer. Figure 5.7 compares the influence of changing velocity magnitude on the position and evolution of the mushy layer in non-eutectic and eutectic salts halfway in the channel.

- For short times ( $t \leq 10$  s), and thus for little ice growth, the **velocity** does not influence the position of the ice front. For both the non-eutectic as eutectic salts, the channel height at which the solid region ends, remains the same under increasing velocity. The effect of the velocity on ice front position starts to become noticeable from  $t \geq 15$  s. This position decreases with increasing velocity meaning that the ice growth is slowed down for larger inlet Reynolds numbers. A similar effect was found in the case of transient freezing of water under constant heat removal and for a clarification of this dependence the reader is referred back to 4.2.2. As the lines are moving closer together with increasing time, a steady-state is reached faster in the high velocity case. The eutectic composition reaches the steady-state condition faster than the non-eutectic salt composition. Steady-state conditions are achieved when fluxes at the phase change interface balance each other out. In eutectic freezing, this means that the flux from the bulk liquid to the solid salt interface is equal to the flux inside the solid region. For non-eutectic freezing, the steady-state condition is met when the heat flux from the bulk liquid towards the mushy zone equals the flux in the mushy region. The heat flux in the mushy zone is dependent on the thermal conductivity which changes dynamically when dealing with ice slurries as we have seen in 5.1. Apparently, this dynamically changing heat flux in the mushy region complicates the convergence to a steady-state situation.

A second velocity influence is on the width of the mushy layer. As eutectic salts have no mushy region, this effect only plays a role in non-eutectic salts. The width of the mushy layer decreases with  $\sim 30 - 40\%$ , depending on time, when increasing the velocity from 1 cm/s to 3 cm/s. The mushy layer will cover a larger part of the domain when lowering the velocity.

Similar plots are generated for varying inlet temperature  $T_0$  and wall temperature  $T_w$  and can be found in Figure B.2 and Figure B.3 in Appendix B. The main findings are:

- The position and width of the mushy layer are also dependent on **inlet temperature**. Again, the influence of  $T_0$  becomes noticeable for longer times. The position of the ice front decreases a maximum of 10% and 17% for the non-eutectic and eutectic salt respectively. The inlet temperature thus has a stronger effect on slowing down ice growth in eutectic salts. The spacing between different times does not become visibly smaller so no conclusion can be drawn about the effect of inlet temperature on the time steady-state is reached. It is expected that higher inlet temperatures will cause faster convergence to steady-state freezing but further research is needed to verify this claim. The mushy layer width reduces with  $\sim 20\%$  to  $30\%$ , depending on time, when the inlet temperature is increased from 842 K to 852 K. The high liquid region is in contact with higher temperatures and therefore it takes longer to further cool down and expand the mushy layer.
- Compared to the inlet temperature, decreasing the **wall temperature** has a stronger effect on the evolution of the mushy layer. The position of the ice front is affected already for short times and decreases with  $\sim 60\%$  for non-eutectic and  $\sim 40 - 50\%$  for eutectic salts. This means that, different from velocity and inlet temperature, the wall temperature influences non-eutectic salts more significantly. As the lines are moving closer together with increasing time, a steady-state is reached faster in the high wall temperature case. The mushy layer widths are slightly increasing with increasing wall temperature (10-20%). The fluid in contact with the top of the mushy layer is approximately constant in every case as the inlet temperature remains the same. The wall temperature determines the cooling rate and therefore how much ice is formed. The layer where  $f_l = 0$  becomes smaller for higher wall temperatures and the region where  $0 < f_l < 1$  thus becomes bigger.

### 5.2.2. Pressure drop

During the process of freezing, the water is cooled and the ice layer becomes thicker. The ice growth will increase the pressure of the molten salt flowing through the channels. A comparison between non-eutectic and eutectic salts for the pressure and the ice thickness in the channel center  $x = W/2$  are given in Figure 5.8 for different times. In LB models, pressure is closely related to density. A reference pressure/density ( $P_0/\rho_0$ ) is always assumed. This reference pressure is not necessary directly related to a physical quantity [31]. For that, the pressure difference  $\Delta P$  relative to this reference pressure  $P_0$  is given. There is a small  $\partial P/\partial y$  gradient thus the average is taken along  $y$ . The sign of  $\Delta P$  is negative because it is applied in the opposite direction of the flow.

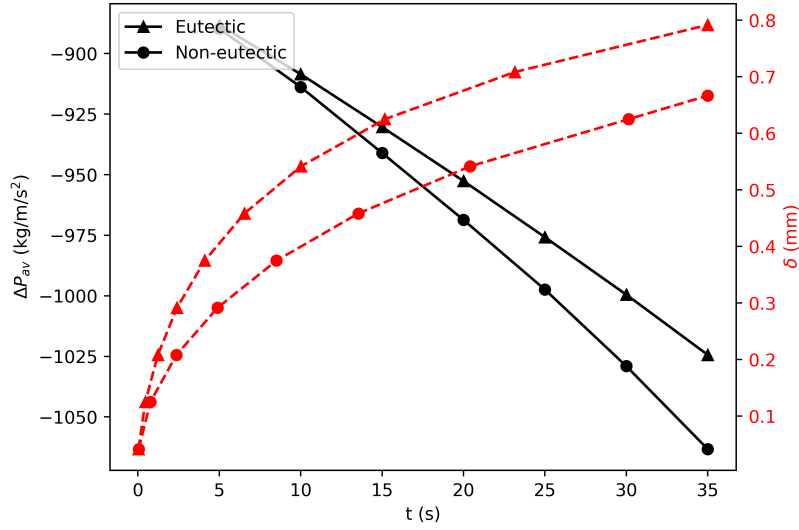


Figure 5.8: The black, solid lines give the pressure drop in time while the red dotted lines resemble the fully solid layer thickness growing in time. The triangles denote eutectic salts while the circles are related to non-eutectic salts.

The thickness of the ice layer is defined as the distance over which molten salt is completely solid. That means the mushy layer is not taken into account when tracking the ice layer thickness in time. The solid region grows more slowly in non-eutectic salts. From that it is expected that the available cross-sectional area is bigger and the pressure drop will be smaller. However, the pressure appears to drop in a faster rate in non-eutectic transient freezing than in eutectic freezing. That means that the mushy layer has a significant effect on the pressure drop caused by the viscous forces acting in the mushy region. This phenomenon could also be clarified with Figure 5.6 where it was found that the velocity in the presence of a mushy layer is higher.

### 5.2.3. Nusselt relation

The local Nusselt number in a channel of freezing liquid can be determined by modifying (4.3). The hydraulic diameter under the presence of a solidified salt layer  $\delta(x)$  is now  $D(x) = 2(H - \delta(x))$ . Figure 5.6 justifies the assumption of a linear temperature distribution in the solid region, thus the heat flux through the solid salt is estimated by

$$q''(x) = -\lambda_s \frac{T_w - T_s}{\delta(x)} \quad (5.14)$$

with thermal conductivity  $\lambda_s$  of the solid region, solidus temperature  $T_s$  given in Table 5.3 and varying wall temperature  $T_w$ . Under quasi-steady state conditions,  $q''(x)$  is assumed to be equal to the overall heat flux from the molten salt to the phase interface  $h(x)(T_{\text{bulk}}(x) - T_s)$ . From that, the heat transfer coefficient  $h(x)$  is estimated and the  $Nu(x)$  can be calculated. For laminar flow in the entrance region, it is common to find the Nusselt number as a function of  $\tilde{x} = \frac{x\alpha}{D(x)^2 U}$  (also known as the Graetz number,  $Gz$ ), locally dependent on the hydraulic diameter  $D(x)$ . To find the dependence on  $\tilde{x}$ , local Nusselt numbers for several flow cases (varying  $T_w$ ,  $T_0$  and  $u_{\text{in}}$ ) are calculated and optimal fits for  $Nu(\tilde{x})$  are determined. The values for coefficients  $a$ ,  $b$  and  $c$  in (5.15) should minimise the difference between the fit and the simulated data.

$$Nu = a \cdot \tilde{x}^{-b} + c \quad (5.15)$$

The solution to the Graetz problem (4.5) is normally dependent on  $b = 1/3$ . During simulations of freezing in non-eutectic and eutectic compositions it is examined if results will deviate from this original coefficient  $b$ . The predefined assumptions on  $a$  and  $c$  are:

- Lee [80] found that under steady-state conditions, the Nusselt relation approaches the Graetz solution in the entrance region. From the bottom figure of 5.5 it can be stated that the *solid salt profile* stays approximately the same under the transient increase of *solid salt thickness*. From that it is expected that,

also under transient freezing, the Nusselt relation in eutectic salts will approach the Graetz solution. This led to the assumption that for **eutectic salts,  $a = 1.56$  is related to the coefficient determining the Graetz solution** and is half the value introduced in (4.5) (the wall is cooled from one instead of two sides). As the Graetz problem is not solved in the presence of a mushy layer (where non-Newtonian behaviour might be present), this assumption cannot be made for non-eutectic freezing. In that case, the optimal coefficient  $a$  must follow from fitting the non-eutectic data.

- The solution to the Graetz problem does not normally contain an offset term  $c$ . This solution was found under steady-state conditions without the presence of a mushy layer. However, we are dealing with *non-eutectic* and eutectic *transient* freezing, and therefore the Nusselt number might shift over time resulting in a **variable offset**. If the eutectic simulations reach a **steady state,  $c$  should be 0**. During simulations, similar magnitudes of  $Nu$  for non-eutectic and eutectic salts are found thus the optimal value for  $c$  in eutectic calculation can be given as input to (5.15) in fitting the non-eutectic Nusselt number.

The optimal values  $a$  and  $b$  in non-eutectic and  $b$  and  $c$  in eutectic freezing are given for various flow cases in Table B.1. Figure 5.9 compares the Nusselt numbers for a single flow case, at different times and thus for increasing solidified salt layer, and illustrates the difference in heat transfer process between non-eutectic and eutectic salts. The other flow cases are visualised in Figure B.4.

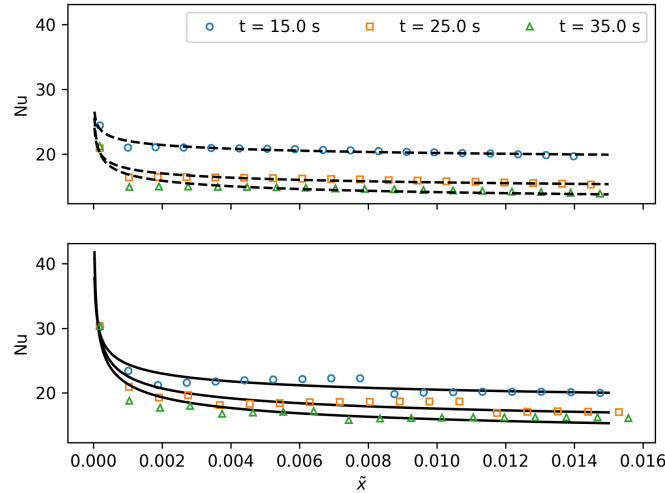


Figure 5.9: The Nusselt number as function of  $\bar{x}$  for different times. The black lines represent the fitted function in the non-eutectic (dotted) and eutectic (solid) case. The data points are related to the locally calculated values of the Nusselt number by the LB model.  $T_w = 790$  K,  $T_0 = 842$  K and  $u_{\max, \text{in}} = 1.0$  cm/s.

Figure 5.9 and the decreasing trend in coefficients  $a$  and  $c$  in Table B.1 indicate that the Nusselt number decreases with increasing ice thickness. Figure 5.6 suggests that the heat flux through the solid region is decreasing when the ice thickness increases. The increase in  $\delta$  also decreases the hydraulic diameter. The decrease in bulk temperature apparently cannot fully compensate this effect as the Nusselt number is decreasing with increasing ice thickness. The Nusselt number will continue to decrease until an approximate steady state solution is reached and the heat removal at the wall is compensated by heat transfer from the liquid to the phase interface. To the writers knowledge, no literature study has been committed to the *transient* behaviour of Nusselt relations under freezing. However, *steady-state* solutions have been found [22, 22] and can thus be compared to the approximate steady state solutions of Figures B.4f and B.4h. A super heat number is introduced by Lee [80]  $Su = \lambda_l / \lambda_s (T_0 - T_f) / (T_f - T_w)$ , where high  $Su$  will result in smaller solidification rate. It was found that the Nusselt number increases with decreasing  $Su$  (increasing ice thickness). The eutectic studies of Figures B.4f and B.4h with super heat numbers  $Su = \lambda_l / \lambda_s 0.9$  and  $Su = \lambda_l / \lambda_s 1.5$  respectively, are well suited for comparison. Their solutions have reached steady-state and the values for larger  $Su$  are indeed smaller, agreeing with the findings of Lee. The explanation for this phenomena relates to the increased

convective heat transfer coefficient due to the acceleration of the fluid flow under converging cross-sectional area.

The Figures in B.4 indicate that the Nusselt number for freezing in non-eutectic laminar flow is approximately the same as for eutectic flow near the end of the channel. This is remarkable as the heat flux towards the phase interface is higher when a mushy layer is present. Figure 5.10 shows the difference in heat fluxes between non-eutectic and eutectic freezing. The non-eutectic heat flux is significantly higher ( $\sim 40\text{--}60\%$ ) in every time step. From (4.3) it is expected that the Nusselt number would also become higher in the non-eutectic cases. Apparently, another term in (4.3) compensates for the difference in heat flux. The other variables depending on  $x$  are the hydraulic diameter  $D(x)$  and the bulk temperature  $T_{\text{bulk}}(x)$ . In 5.8, the fully solid region appears to be smaller in the non-eutectic flow which will enlarge  $D(x)$ . For that, the compensation must come from the bulk temperature. The difference in bulk temperature along  $x$  for freezing in non-eutectic and eutectic salt flow is given in Figure 5.11. Both temperatures stay under  $T_0$  and are decreasing in time, as expected. However, the bulk temperature is increasing along  $x$  in the presence of a mushy layer whereas it is decreasing in the absence of it. A clarification of this phenomenon is that the mushy region forms some kind of insulation between the solidified salt layer and the liquid molten salt. As the mushy layer is increasing along  $x$ , the fluid is better isolated from direct contact with the cold solid region and will therefore be warmer than at the channel entrance. The higher bulk temperature will compensate for the higher heat flux, resulting in similar Nusselt numbers for the non-eutectic and eutectic freezing under laminar flow.

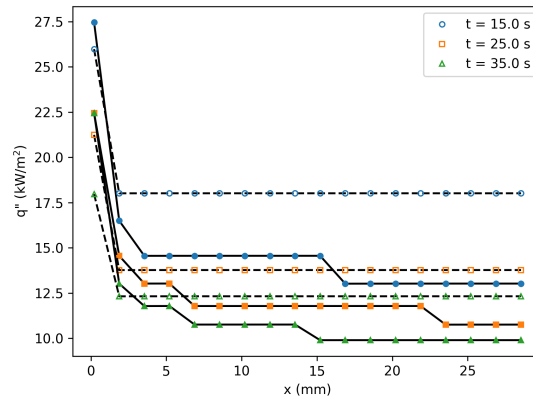


Figure 5.10: Heat flux along  $x$  for different times and thus for increasing salt layer thickness. The dotted lines with empty figures are the heat fluxes for non-eutectic salts and the solid lines with solid figures for eutectic salts.  $T_w = 790\text{ K}$ ,  $T_0 = 842\text{ K}$  and  $u_{\text{max,in}} = 1.0\text{ cm/s}$ .

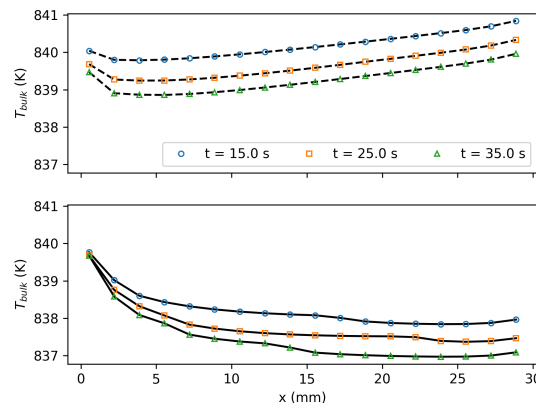


Figure 5.11: Bulk temperature along  $x$  for different times and thus for increasing salt layer thickness. The dotted lines with empty figures are the heat fluxes for non-eutectic salts and the solid lines with solid figures for eutectic salts.  $T_w = 790\text{ K}$ ,  $T_0 = 842\text{ K}$  and  $u_{\text{max,in}} = 1.0\text{ cm/s}$ .

The Nusselt number without the presence of phase change is normally dependent on  $\tilde{x}^{-1/3}$  in the entry region. The dependence on  $\tilde{x}$  is reflected through coefficient  $b$  in the current study. The weighted mean and standard deviation of  $b$  over the different test cases in Table B.1 is  $b = 0.21 \pm 0.05$  and  $b = 0.32 \pm 0.02$  for freezing in non-eutectic and eutectic laminar salt respectively. Eutectic freezing approaches the  $b = 1/3$  dependence, agreeing with findings by Lee. The non-eutectic coefficients are somewhat lower than  $b = 1/3$ . It indicates that the presence of a mushy layer modifies the  $\tilde{x}^{-1/3}$  dependence commonly present in thermal laminar channel flow. The presence of a mushy layer flattens the Nusselt relation in the entrance region. No correlation is found between the thickness of the mushy layer and coefficient  $b$ . It might indicate that thickness of the mushy layer does not influence the  $\tilde{x}$  dependence but more data must be generated to further support that claim.

The non-eutectic value for  $a = 1.2 \pm 0.3$ , weighted over the cases that steady state is not reached yet (i.e.  $c \neq 0$ ) and  $t = 35$  s, approaches the, in eutectic salts assumed,  $a = 1.56$ . This supports the claim that the Nusselt numbers in the presence and absence of a mushy layer are indeed similar. The non-eutectic coefficients  $a$  in cases where eutectic steady-state conditions are reached (i.e.  $c = 0$ ), do not coincide with the assumed value of  $a = 1.56$ . Earlier it was found that steady-state is reached sooner in eutectic than non-eutectic freezing. This could be the explanation for the discrepancy as  $c$  is set to 0 in (5.15), while it might be larger than zero in the non-eutectic case when unsteady conditions still apply. It is desired that the found Nusselt relations will be compared to experimental results in the future.

The current study gives a first indication of the relationship between  $Nu$  and  $\tilde{x}$  under the presence of a mushy layer. This relation can be used to estimate transient solid salt growth in convectively flowing non-eutectic salt mixtures by setting up thermal energy balances over the solid and mushy + liquid regions. The following equations can then reduce the problem to a one-dimensional problem

$$\frac{\partial T_{\text{liq}}}{\partial t} + \frac{Q_0}{A(\delta)} \frac{\partial T_{\text{liq}}}{\partial x} = -\frac{h(x)(T_{\text{liq}} - T_s)}{A(\delta)\rho_l C_{p,ref}} \quad (5.16)$$

$$\rho_s \left[ \Delta H + C_{p,ref}(T_{\text{liq}} - T_s) + C_{p,s} \frac{(T_s - T_w)}{2} \right] \frac{\partial \delta}{\partial t} = -h(x)(T_{\text{liq}} - T_s) + \lambda_s \frac{(T_s - T_w)}{\delta} \quad (5.17)$$

$$A(\delta) = A - \delta \quad (5.18)$$

Following the example of [14], this set of equations can be solved by a first order difference scheme. The change in molten salt temperature  $T_{\text{liq}}$  along  $x$  is determined by axial flow rate  $Q_0$ , available cross-sectional area  $A$  and heat transfer to the phase interface  $h(x)(T_{\text{liq}} - T_s)$ . The Nusselt relation as function of  $\tilde{x}$  is related to  $h(x)$ . As  $\tilde{x}$  is dependent on  $D(x) = 2(H - \delta(x))$  the estimation of  $\delta(x)$  of the previous time step will give  $Nu$  and thus  $h$  as function of  $x$  for varying ice thickness. The resulting  $T_{\text{liq}}$  is implemented in (5.17), balancing heat fluxes at the solid-mushy region interface, to estimate the local salt augmentation thickness of the next time step. The terms on the left hand side represent contributions to the energy required to solidify the molten salt: the enthalpy of fusion  $\Delta H$ , the change in sensible heat in the liquid + mushy region and the change in internal energy of the solidified salt due to a mass increase. The performance of above procedure must be tested by comparing its estimations on transient salt augmentation growth to more elaborate two-dimensional simulations. If they do, it could greatly decrease computation time while maintaining accurate predictions.

# 6

## Conclusion and Recommendations

Nuclear reactors are an important factor in stabilising energy grids. The Gen IV molten salt fast reactor (MSFR) must contribute to safer and more sustainable nuclear power generation. Understanding the freezing phenomena in MSFRs will play a crucial role in the prediction of safety risks. This research aimed to develop tools to accurately predict transient freezing in cooled laminar molten salt flow and to give insights in the effect on thermal flow properties. To this end, a combined fluid dynamic and phase change model was developed and validated through experimental studies. Subsequently, it is implemented to find differences in freezing processes of eutectic and non-eutectic molten salts.

### 6.1. Simulation of experimental freezing studies

A double distribution function filter-matrix lattice Boltzmann (DDF FMLB) model is build to simulate thermal flow. It is validated by the well defined velocity profile in Poiseuille flow and the known Nusselt relation in laminar flow between heated parallel plates. To deal with phase change, two forms of implementing the source-based enthalpy method are tested in the Stefan problem. No significant difference in accuracy and efficiency between the combined transient-source term and iterative scheme is found. The transient-source term scheme is chosen to be included in the build DDF FMLB because of its expected better efficiency in more complex freezing cases. When the described model must simulate transient freezing under laminar flow, it should deal with the no-slip boundary condition on the moving phase interface. For that, the immersed boundary scheme and the enthalpy-porosity method are implemented. They work similarly in the experimental benchmark studies for transient freezing in water, however differences are found when a mushy layer is present. During simulations it is discovered that a maximum lattice Boltzmann velocity of  $u_{\max, LB} = 0.01$  should be incorporated to maintain stability and that convective boundary conditions can better converge temperature and thus have smaller effect on the rate of solidification.

Simulations of the time-lag period and ice grow rates in a channel cooled from the top by constant heat flux are compared to measurements from an experimental study done by [14]. The simulation can well capture the trends found by measurements. The time-lag curve is increasing with inlet temperature with a minimum deviation of 21% between simulated and experimentally values. The linearity in ice grow rates found by measurements is well reflected in the numerical ice layer thickness as function of time. The ice grow rate is decreasing for increasing inlet temperature and velocity, a trend found both by simulation and experimental measurements. Three inlet velocity cases are tested that deviate from measurements by 12%, 19% and 8.3% respectively. It can be concluded that the lattice Boltzmann (LB) model can make reasonably accurate qualitative and quantitative predictions on freezing processes in channel flow cooled by constant heat removal.

The case of an isothermally cooled wall is also studied. Analytical and experimental findings [23, 27] are compared to the ice profile retrieved from an LB simulation. Under fully converged Poiseuille flow and a uniform wall temperature below the freezing temperature, the simulated profile matches the analytical solution well, with an averaged deviation of less than 8%. The inlet velocity and wall temperature are adjusted to resemble experimental conditions most precisely. However, no good agreement with the measured ice profile is found as the deviation exceeds 20%. The strong resemblance to the analytical solution excludes the

conclusion that the model is incorrect for isothermally cooled laminar flow between plates. Improvements on the model and experiment must be made to accurately use these measurements as benchmark case. The recommended adjustments are discussed in 6.3.

In order to correctly simulate the freezing process of molten salts under convective flow, a mushy zone is imposed. The substance of coexisting solid particles with liquid salt is non-Newtonian of nature and its thermophysical properties are defined differently than in the solid or liquid region. Implementations of these modifications to the original model are tested on an experimental study of heat transfer coefficients in ice slurry [73]. The non-linearity in the relationship between the heat transfer coefficient and the ice fraction is well reflected in the numerical findings. The average deviation to the experimentally found coefficients is 8.2%, significantly improving the study performed by [75] where deviations rose up to 22% in the high ice fraction limit. The immersed boundary and enthalpy-porosity methods led to similar heat transfer coefficients but differences in flow profile indicated that the enthalpy-porosity method might better capture the non-Newtonian behaviour of the substance in the mushy zone. However, a quantitative comparison of the immersed boundary and enthalpy-porosity scheme to known velocity profiles in non-Newtonian fluids must further confirm this claim.

## 6.2. Effect of mushy layer on thermal flow properties

Above studies led to a well-grounded simulation of freezing in molten salt flow. Molten salts are typically non-eutectic of nature coming with the presence of a mushy layer during solidification process. The effect of the mushy zone evolution on velocity, temperature, pressure and heat transfer is compared to eutectic freezing. The temperature profile in the mushy layer follows a steeper curve than it would in liquid, indicating that the heat flux is higher at the solid-mushy interface than at the solid-liquid interface in eutectic freezing. The momentum sink caused by the mushy layer decreases the cross-sectional area available for flow in a faster rate thus accelerating the velocity more than in eutectic salts. Velocity and temperature themselves influence the evolution of the mushy layer as well. It is found at a lower position along  $y$  with decreased width for increasing inlet velocity, inlet and wall temperature. The first two have a stronger effect on eutectic salts whereas the last influences non-eutectic salts more significantly. The solid region grows at a slower rate in non-eutectic freezing. However, the presence of the mushy layer on top increases the pressure drop in the channel compared to distinct solid and liquid regions.

Most importantly, the heat transfer processes in molten salts under convective freezing must be understood to make accurate predictions on the ice grow rate and thus on the risk of pipe blockage. For that, the Nusselt relation in the presence and absence of a mushy layer is determined as function of transiently growing solidified salt thickness. These Nusselt numbers have similar magnitudes past the entrance region where the solid salt profiles are approximately flat. This is remarkable as the heat fluxes through the mushy layer are found to be higher than fluxes over the liquid-solid interface. A higher bulk temperature in non-eutectic flow compensates for this difference resulting in the similarity. At the entrance their dependencies on  $\tilde{x}^{-b}$  are different:  $b = 0.21 \pm 0.05$  for non-eutectic freezing where  $b = 0.32 \pm 0.02$  for eutectic freezing. These dependencies give a first indication of an empirical formula of the Nusselt relation in molten salt freezing processes which can be used to reduce the problem to a one-dimensional problem with the aim of efficient and accurate prediction of the transient augmented salt growth.

## 6.3. Recommendations

- The numerically found ice profile did not fully agree with measured profiles in the isothermally cooling experiment. This could either be linked to deviations seen in the simulated velocity profile compared to the measurements, or to incorrectness in the thermal boundary definition. It is expected that the last is more likely to have caused the discrepancy between the lattice Boltzmann model and experimental findings. To use this benchmark case in the future it is recommended that a **convective cooling boundary** is imposed to see if the formed ice profiles better match the measured data. The measurement data can be made less sensitive to errors in the wall temperature definition by either imposing **super-cooling** or take measurements **further away from the channel entrance**.
- As input parameters for the DDF LB model are highly dependent on kinematic viscosity and thermal diffusivity, accurate **measurements on molten salt properties** are needed to ensure precise prediction of transient freezing processes. Especially thermal diffusivity lacks experimental data found in litera-

ture. The model is build in such a way that it can deal with local dependencies on temperature. It is therefore desired that the thermophysical properties are measured for a wide range of temperatures.

- First indications on the **Nusselt relation** of freezing under laminar flow of pseudo-binary system LiF-ThF-UF<sub>4</sub> and binary system LiF-ThF<sub>4</sub> is given and compared. To get a better prediction on the coefficients present in the fitted Nusselt relations, more flow cases and other (pseudo-)binary systems must be tested numerically. It is desired that the found dependence on  $\bar{x}^{-0.21 \pm 0.05}$  in the presence of a mushy layer is validated by an experimental study. To get a complete picture, also turbulent Nusselt relations should be derived.
- The MSFR is designed in such a way that molten salt flow can be either laminar or turbulent. The presented study only focused on laminar flow. It is therefore recommended that the current model is **extended to three dimensions**. This comes at the cost of efficiency and **more advanced adaptive grid refinement techniques** must be implemented in which the mushy layer solely is defined by a moving fine grid, surrounded by course grid cells. Moreover, as the lattice Boltzmann field of research is rapidly expanding and innovating, new and more efficient models are consistently developed. The filter-matrix model might not be most suitable for three-dimensional problems and newer methods like the Cumulant or Karlin-Bosch-Chikatamarla LBM [41] have the potential to solve turbulent flows with higher accuracy, stability or efficiency.

# A

## Thermophysical dependences

### A.1. Kinematic viscosity

#### A.1.1. Water

Data on the Prandtl number  $Pr$  of water is retrieved from [81] and linear interpolation is used to find estimations for local temperatures. The relation  $\nu = \alpha \cdot Pr$  is used to find the kinematic viscosity.

#### A.1.2. Molten salt

$$\nu = (0.13919 \pm 1.4 \cdot 10^{-3}) \cdot e^{(2148.3 \pm 0.9)(K/T)} \quad [76]$$

### A.2. Thermal diffusivity

#### A.2.1. Water

Data on thermal diffusivity  $\alpha$  of liquid water and ice is retrieved from [81] and linear interpolation is used to find estimations for local temperatures.

#### A.2.2. Molten salt

Data on thermal diffusivity  $\alpha$  of solid molten salt is retrieved from [78] and linear interpolation is used to find estimations for local temperatures.

### A.3. Thermal conductivity

#### A.3.1. Water

Data on thermal conductivity  $\lambda$  of liquid water and ice is retrieved from [81] and linear interpolation is used to find estimations for local temperatures.

#### A.3.2. Copper

Data on thermal conductivity  $\lambda$  of copper is retrieved from [81] and linear interpolation is used to find estimations for local temperatures.

### A.4. Specific heat

#### A.4.1. Water

Data on specific heat  $C_p$  of liquid water and ice is retrieved from [81] and linear interpolation is used to find estimations for local temperatures.

#### A.4.2. Carrier liquid 10.6% ethanol

$$C_{p,cl} = 7705.1 - 21.598T + 0.0344T^2 \quad [70]$$

**A.4.3. Copper**

Data on specific heat  $C_p$  of copper is retrieved from [81] and linear interpolation is used to find estimations for local temperatures.

# B

## Figures & Data

### B.1. Linearity in ice growth under constant heat removal

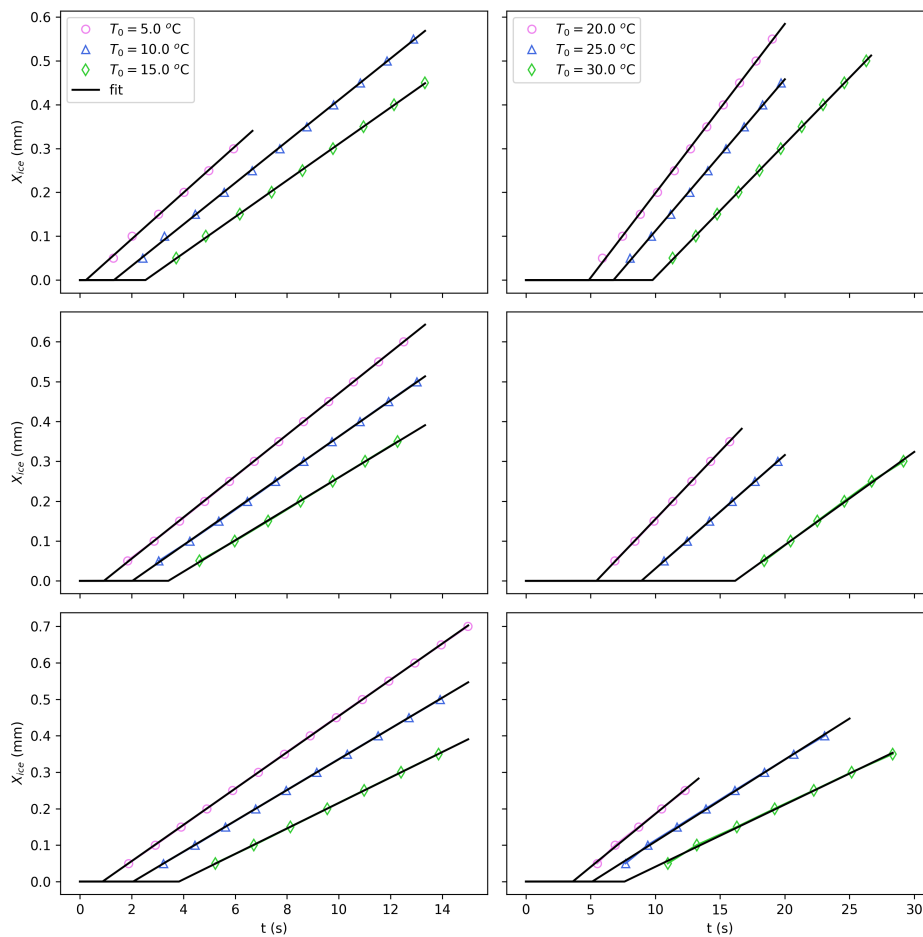
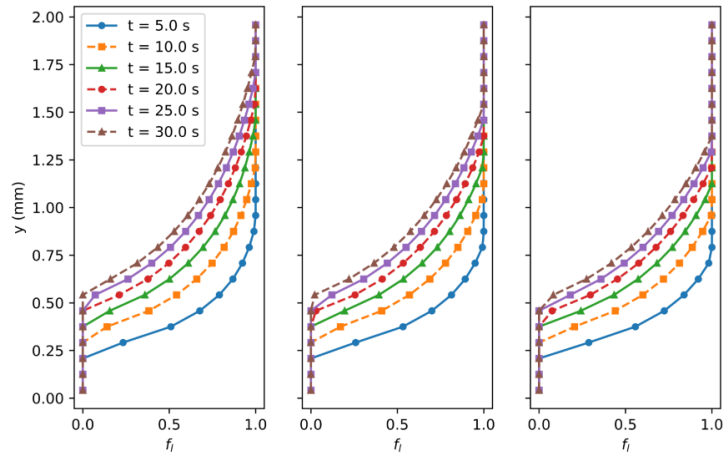
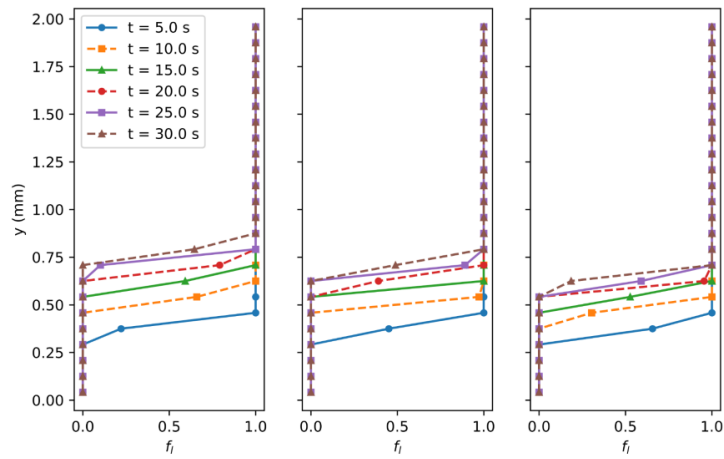


Figure B.1: Linearity in ice layer thickness as function of time for various flow cases. From top to bottom the rows represent the individual inlet velocities  $u_{\max, \text{in}} = 0.6, 1.2, 2.4$  cm/s. The position of the ice layer is denoted with the empty figures for different inlet temperatures  $T_0$ . The black lines represent the linear fits.

## B.2. Mushy zone versus inlet and wall temperature



(a) Non-eutectic



(b) Eutectic

Figure B.2: The liquid fraction  $f_l$  at  $x = W/2$  in terms of channel height at different inlet temperatures  $T_0 = 842, 847, 852$  K. The inlet temperature increases from left to right. The results of the non-eutectic salt are in the top figure and eutectic in the bottom. The inlet velocity and wall temperature are  $u_{\max, \text{in}} = 2.0$  cm/s and  $T_w = 800$  K everywhere.

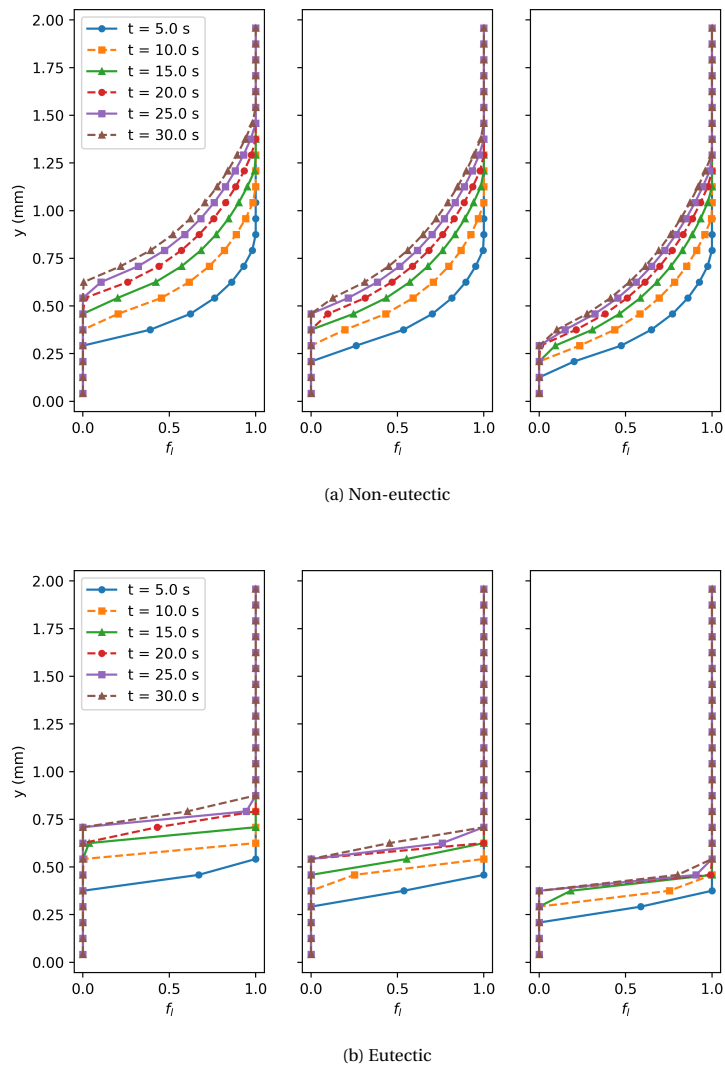


Figure B.3: The liquid fraction  $f_l$  at  $x = W/2$  in terms of channel height at different wall temperatures  $T_w = 790, 800, 810$  K. The wall temperature increases from left to right. The results of the non-eutectic salt are in the top figure and eutectic in the bottom. The inlet velocity and inlet temperature are  $u_{\max, \text{in}} = 2.0$  cm/s and  $T_w = 842$  K everywhere.

### B.3. Nusselt relation for various flow cases

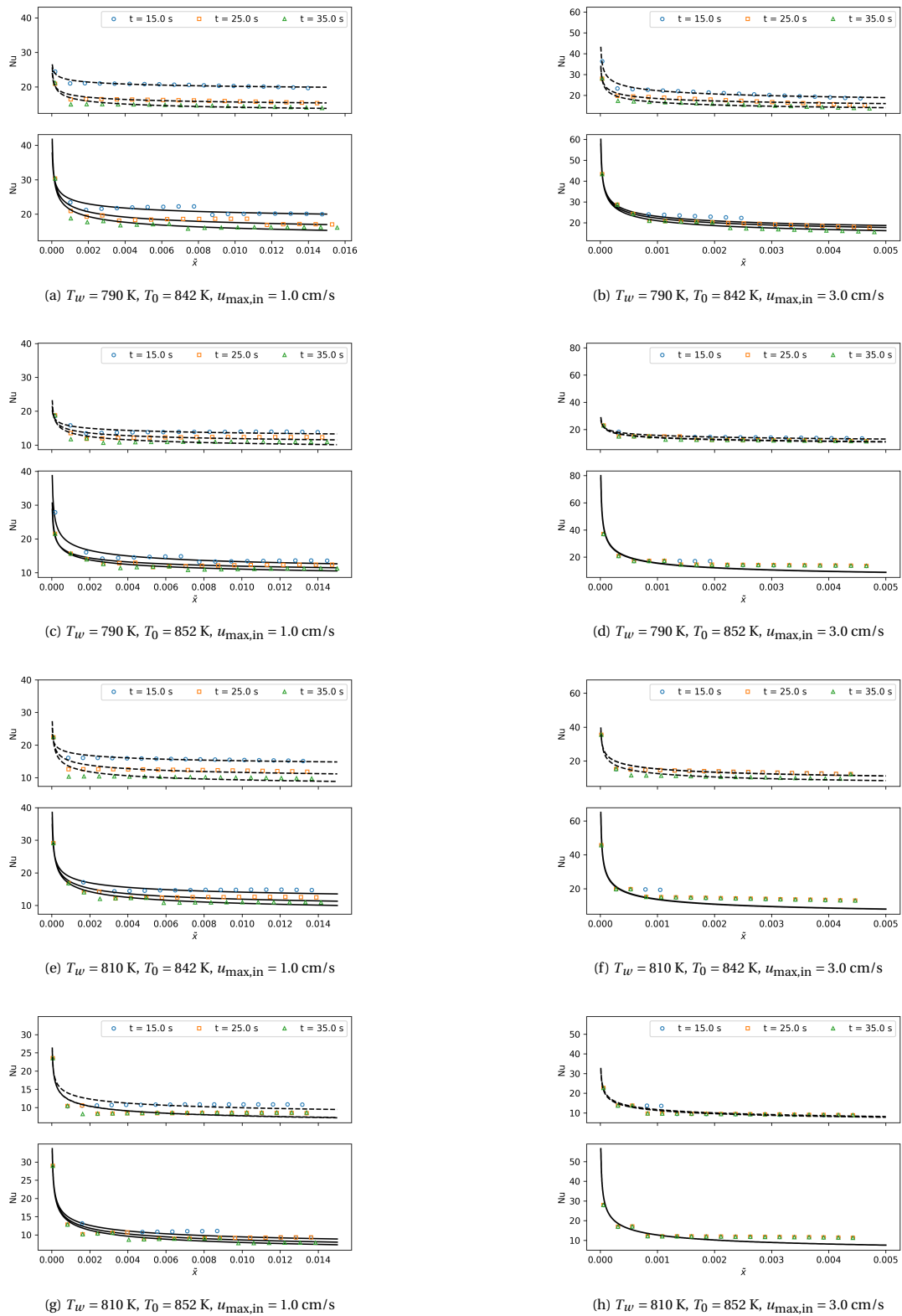


Figure B.4: Nusselt number as function of  $\bar{x} = x\alpha/D^2U$  for various flow cases

## B.4. Coefficients that optimise the Nusselt equation fit

Table B.1: Coefficients that optimise the Nusselt equation (5.15) for different times in the non-eutectic and eutectic case. The parameters for  $T_w$ ,  $T_0$  and  $u_{\max, \text{in}}$  are varied.

Parameters	t (s)	Non-eutectic		Eutectic	
		a	b	b	c
$T_w = 790 \text{ K}$	15	1.7±0.1	0.24±0.01	0.274±0.004	14.7±0.3
$T_0 = 842 \text{ K}$	25	1.2±0.1	0.25±0.01	0.283±0.004	11.7±0.3
$u = 1.0 \text{ cm/s}$	35	1.2±0.1	0.26±0.01	0.288±0.003	10.1±0.3
$T_w = 810 \text{ K}$	15	2.5±0.2	0.22±0.01	0.297±0.004	7.6±0.5
$T_0 = 842 \text{ K}$	25	1.7±0.2	0.27±0.01	0.303±0.003	5.3±0.4
$u = 1.0 \text{ cm/s}$	35	1.2±0.2	0.30±0.01	0.306±0.002	4.0±0.3
$T_w = 790 \text{ K}$	15	1.9±0.1	0.24±0.01	0.288±0.003	11.6±0.4
$T_0 = 842 \text{ K}$	25	1.6±0.1	0.23±0.01	0.289±0.001	10.5±0.2
$u = 3.0 \text{ cm/s}$	35	1.4±0.1	0.26±0.01	0.292±0.002	9.0±0.3
$T_w = 810 \text{ K}$	15	6.3±0.4	0.12±0.01	0.33±0.01	-
$T_0 = 842 \text{ K}$	25	6.4±0.4	0.12±0.01	0.33±0.01	-
$u = 3.0 \text{ cm/s}$	35	3.3±0.4	0.19±0.01	0.33±0.01	-
$T_w = 790 \text{ K}$	15	1.7±0.1	0.25±0.01	0.271±0.003	7.9±0.2
$T_0 = 852 \text{ K}$	25	1.6±0.2	0.26±0.01	0.276±0.003	6.2±0.3
$u = 1.0 \text{ cm/s}$	35	1.4±0.2	0.28±0.01	0.279±0.002	5.3±0.2
$T_w = 810 \text{ K}$	15	2.5±0.4	0.21±0.02	0.30±0.01	3.2±0.4
$T_0 = 852 \text{ K}$	25	1.5±0.2	0.28±0.02	0.30±0.01	2.2±0.5
$u = 1.0 \text{ cm/s}$	35	1.9±0.3	0.26±0.02	0.305±0.005	1.4±0.4
$T_w = 790 \text{ K}$	15	6.5±0.4	0.13±0.01	0.33±0.02	-
$T_0 = 852 \text{ K}$	25	4.4±0.3	0.17±0.01	0.33±0.01	-
$u = 3.0 \text{ cm/s}$	35	4.3±0.3	0.17±0.01	0.33±0.01	-
$T_w = 810 \text{ K}$	15	2.2±0.2	0.25±0.01	0.31±0.01	-
$T_0 = 852 \text{ K}$	25	2.1±0.2	0.25±0.02	0.31±0.01	-
$u = 3.0 \text{ cm/s}$	35	2.5±0.2	0.25±0.02	0.31±0.01	-

# C

## Numerical model

This QR code links to a gitlab page where all python codes of the developed numerical models can be found.



# Bibliography

- [1] IPCC. Summary for policymakers. In *Climate Change 2021: The Physical Science Basis. Contribution of Working Group I to the Sixth Assessment Report of the Intergovernmental Panel on Climate Change*, pages 3–32. Cambridge University Press, Cambridge, United Kingdom and New York, NY, USA, 2021. doi: 10.1017/9781009157896.001.
- [2] Pathak, A.M. et al. Technical Summary. In *Climate Change 2021: The Physical Science Basis. Contribution of Working Group I to the Sixth Assessment Report of the Intergovernmental Panel on Climate Change*, pages 33–144. Cambridge University Press, Cambridge, United Kingdom and New York, NY, USA, 2022. doi: 10.1017/9781009157896.002.
- [3] EIA. International energy outlook 2021 narrative, 2021.
- [4] Gen IV International Forum. [https://www.gen-4.org/gif/jcms/c\\_9260/public](https://www.gen-4.org/gif/jcms/c_9260/public). (Accessed: 02-06-2022).
- [5] SAMOSAFER. Project. <https://samosafer.eu/project/>. (Accessed: 02-06-2022).
- [6] Allibert, M. et al. *Molten salt fast reactors*. 2016. ISBN 9780081001622. doi: 10.1016/B978-0-08-100149-3.00007-0.
- [7] Kloosterman, J. L. Safety assessment of the molten salt fast reactor (SAMOFAR). *Molten Salt Reactors and Thorium Energy*, pages 565–570, 2017. doi: 10.1016/B978-0-08-101126-3.00020-8.
- [8] Ronco, A.D., Cammi, A. and Lorenzi, S. Preliminary analysis and design of the heat exchangers for the molten salt fast reactor. *Nuclear Engineering and Technology*, 52(1):51–58, 2020. doi: <https://doi.org/10.1016/j.net.2019.07.013>.
- [9] Merle, E. [https://www.gen-4.org/gif/upload/docs/application/pdf/2017-05/07\\_elsa\\_merle\\_france.pdf](https://www.gen-4.org/gif/upload/docs/application/pdf/2017-05/07_elsa_merle_france.pdf), 2017. (Accessed: 02-06-2022).
- [10] Wang, L., Sundén, B. and Manglik, R.M. *Plate heat exchangers: design, applications and performance*, volume 11. WITPress, 2007.
- [11] Figley, J.T. Numerical modeling and performance analysis of printed circuit heat exchanger for very high-temperature reactors. Master's thesis, The Ohio State University, 2009.
- [12] Wang, Y., Alvarado, J. and Terrell, W. Thermal and flow characteristics of helical coils with reversed loops. *International Journal of Heat and Mass Transfer*, 126:670–680, 11 2018. doi: 10.1016/j.ijheatmasstransfer.2018.02.110.
- [13] Le Brun, N., Hewitt, G.F. and Markides, C.N. Transient freezing of molten salts in pipe-flow systems: Application to the direct reactor auxiliary cooling system (DRACS). *Applied Energy*, 186(0):56–67, 2017. ISSN 03062619. doi: 10.1016/j.apenergy.2016.09.099.
- [14] Voulgaropoulos, V. et al. Transient freezing of water between two parallel plates: A combined experimental and modelling study. *International Journal of Heat and Mass Transfer*, 153:119596, jun 2020. ISSN 00179310. doi: 10.1016/j.ijheatmasstransfer.2020.119596.
- [15] Zerkle, R.D. and Sunderland, J.E. The effect of liquid solidification in a tube upon laminar-flow heat transfer and pressure drop. *Journal of Heat Transfer*, 90(2):183–189, 1968. ISSN 15288943. doi: 10.1115/1.3597471.
- [16] Lee, D.G. and Zerkle, R.D. The Effect of Liquid Solidification in a Parallel Plate Channel Upon Laminar-Flow Heat Transfer and Pressure Drop. *Journal of Heat Transfer*, 91(4):583–585, nov 1969. ISSN 0022-1481. doi: 10.1115/1.3580246.

- [17] Depew, C.A. and Zenter, R.C. Laminar flow heat transfer and pressure drop with freezing at the wall. *Int. J. Heat mass transfer*, 12:1710–1714, 1969. doi: [https://doi.org/10.1016/0017-9310\(69\)90104-5](https://doi.org/10.1016/0017-9310(69)90104-5).
- [18] Mulligan, J.C. and Jones, D.D. Experiments on heat transfer and pressure drop in a horizontal tube with internal solidification. *International Journal of Heat and Mass Transfer*, 19(2):213–219, 1976. ISSN 00179310. doi: 10.1016/0017-9310(76)90115-0.
- [19] Liu, H. and Hwang, G.J. An experiment on liquid solidification in thermal entrance region of a circular tube. *Letters in Heat and Mass Transfer*, 4(6):437–444, 1977. ISSN 00944548. doi: 10.1016/0094-4548(77)90103-5.
- [20] Özisik, M.N. and Mulligan, J.C. Transient Freezing of Liquids in Forced Flow Inside Circular Tubes. *Journal of Heat Transfer*, 91(3):385–389, aug 1969. ISSN 0022-1481. doi: 10.1115/1.3580190.
- [21] Sproston, J.L. Two-dimensional solidification in pipes of rectangular section. *International Journal of Heat and Mass Transfer*, 24(9):1493–1501, 1981. ISSN 00179310. doi: 10.1016/0017-9310(81)90216-7.
- [22] Kikuchi, Y., Shigemasa, Y. and Ogata, T. Steady-State Freezing of Liquids in Laminar Flow Between Two Parallel Plates. *Journal of Nuclear Science and Technology*, 23(11):979–991, 1986. ISSN 00223131. doi: 10.3327/jnst.23.979.
- [23] Weigand, B. and Beer, H. Transient freezing of liquids in forced laminar flow inside a parallel plate channel. *Wärme- und Stoffübertragung*, 27(2):77–84, 1992. ISSN 00429929. doi: 10.1007/BF01590122.
- [24] Savino, J.M. and Siegel, R. Experimental and Analytical Study of the Transient Solidification of a Warm Liquid Flowing Over a Chilled Flat Plate. (June):1–64, 1967.
- [25] Seki, N., Fukusako, S. and Younan, G.W. A transition phenomenon of ice formation in water flow between two horizontal parallel plates. *Wärme - und Stoffübertragung*, 18(2):117–128, 1984. ISSN 1432-1181. doi: 10.1007/BF01006607.
- [26] Ismail, K.A.R. and Padilha, A. A study on transient ice formation of laminar flow inside externally super-cooled rectangular duct. *Applied Thermal Engineering*, 20(18):1709–1730, 2000. ISSN 1359-4311. doi: [https://doi.org/10.1016/S1359-4311\(99\)00093-9](https://doi.org/10.1016/S1359-4311(99)00093-9).
- [27] Kaaks, B. *Melting and Solidification Phenomena of Salt in a Molten Salt Nuclear Reactor*. Ph.d. thesis, Delft University of Technology, 2022. Unpublished preliminary results.
- [28] Tano, M., Rubiolo, P. and Doche, O. Progress in modeling solidification in molten salt coolants. *Modelling and Simulation in Materials Science and Engineering*, 25(7), August 2017. doi: 10.1088/1361-651x/aa8345.
- [29] Lu, J., Ding, J. and Yang, J. Solidification and melting behaviors and characteristics of molten salt in cold filling pipe. *International Journal of Heat and Mass Transfer*, 53(9):1628–1635, 2010. doi: <https://doi.org/10.1016/j.ijheatmasstransfer.2010.01.033>.
- [30] Mahdaoui, M. et al. Laminar flow in circular tube with internal solidification of a binary mixture. *Energy*, 78:713–719, 2014. ISSN 0360-5442. doi: <https://doi.org/10.1016/j.energy.2014.10.062>.
- [31] Krüger, T. et al. *The Lattice Boltzmann Method*. Springer, 2017.
- [32] Wei, S. and Güceri, S.I. Solidification in developing pipe flows. *International Journal of Heat and Fluid Flow*, 9(2):225–232, 1988. ISSN 0142-727X. doi: [https://doi.org/10.1016/0142-727X\(88\)90076-8](https://doi.org/10.1016/0142-727X(88)90076-8).
- [33] Sadeghipour, M.S. and Alborzi, K. Axial conduction in the transient laminar freezing of liquids in convectively cooled tubes. *Numerical Heat Transfer, Part A: Applications*, 25(4):427–439, 1994. doi: 10.1080/10407789408955958.
- [34] Conde, R. et al. Numerical model for two-phase solidification problem in a pipe. *Applied Thermal Engineering*, 24(17):2501–2509, 2004. ISSN 1359-4311. doi: <https://doi.org/10.1016/j.applthermaleng.2004.04.010>.

- [35] Fallahnezhad, N. and Nazif, H.R. Numerical Solution of Transient Freezing Equations of a Laminar Water Flow in a Channel with Constant Wall Temperature in the Absence of Gravity. *Microgravity Science and Technology*, 32(3):493–505, 2020. ISSN 1875-0494. doi: 10.1007/s12217-019-09748-0.
- [36] Huber, C. et al. Lattice Boltzmann model for melting with natural convection. *International Journal of Heat and Fluid Flow*, 29(5):1469–1480, 2008. ISSN 0142-727X. doi: <https://doi.org/10.1016/j.ijheatfluidflow.2008.05.002>.
- [37] Jourabian, M., Farhadi, M. and Darzi, A.A.R. Simulation of natural convection melting in an inclined cavity using lattice Boltzmann method. *Scientia Iranica*, 19(4):1066–1073, 2012. ISSN 1026-3098. doi: <https://doi.org/10.1016/j.scient.2012.06.014>.
- [38] Liu, Q. and He, Y.L. Double multiple-relaxation-time lattice Boltzmann model for solid-liquid phase change with natural convection in porous media. *Physica A: Statistical Mechanics and its Applications*, 438:94–106, 2015. ISSN 03784371. doi: 10.1016/j.physa.2015.06.018.
- [39] Gao, D. and Chen, Z. Lattice Boltzmann simulation of natural convection dominated melting in a rectangular cavity filled with porous media. *International Journal of Thermal Sciences*, 50(4):493–501, 2011. ISSN 1290-0729. doi: <https://doi.org/10.1016/j.ijthermalsci.2010.11.010>.
- [40] Chatterjee, D. and Chakraborty, S. A hybrid lattice Boltzmann model for solid-liquid phase transition in presence of fluid flow. *Physics Letters A*, 351(4):359–367, 2006. ISSN 0375-9601. doi: <https://doi.org/10.1016/j.physleta.2005.11.014>.
- [41] Sharma, K.V., Straka, R. and Tavares, F.W. Current status of Lattice Boltzmann Methods applied to aerodynamic, aeroacoustic, and thermal flows. *Progress in Aerospace Sciences*, 115(January 2019):100616, 2020. ISSN 03760421. doi: 10.1016/j.paerosci.2020.100616.
- [42] Li, Q. et al. Lattice Boltzmann methods for multiphase flow and phase-change heat transfer. *Progress in Energy and Combustion Science*, 52:62–105, feb 2016. ISSN 03601285. doi: 10.1016/j.pecs.2015.10.001.
- [43] Li, J. *Fluid Mechanics Based on Continuum Assumption*, pages 1–23. Springer International Publishing, 2020. ISBN 978-3-030-26466-6. doi: 10.1007/978-3-030-26466-6\_1.
- [44] Hirsch, C. Chapter 1 - The Basic Equations of Fluid Dynamics. In Charles Hirsch, editor, *Numerical Computation of Internal and External Flows (Second Edition)*, pages 27–64. Butterworth-Heinemann, Oxford, second edition edition, 2007. ISBN 978-0-7506-6594-0. doi: <https://doi.org/10.1016/B978-075066594-0/50041-2>.
- [45] Akker, van den H.E.A. and Mudde, R. *Fysische transport verschijnselen I*. Delft University Press, 1996. ISBN 90-407-1204-2.
- [46] Huang, R., Wu, H. and Cheng, P. A new lattice Boltzmann model for solid-liquid phase change. *International Journal of Heat and Mass Transfer*, 59(1):295–301, 2013.
- [47] Jiaung, W.S., Ho, J.R. and Kuo, C. P. Lattice Boltzmann method for the heat conduction problem with phase change. *Numerical Heat Transfer, Part B: Fundamentals*, 39(2):167–187, 2001. ISSN 10407790. doi: 10.1080/10407790150503495.
- [48] Somers, J.A. Direct simulation of fluid flow with cellular automata and the lattice-Boltzmann equation. *Applied Scientific Research*, 51(1):127–133, 1993. ISSN 1573-1987. doi: 10.1007/BF01082526.
- [49] Zhuo, C., Zhong, C. and Cao, J. Filter-matrix lattice Boltzmann model for incompressible thermal flows. *Physical Review E*, 85(4):046703, apr 2012. ISSN 1539-3755. doi: 10.1103/PhysRevE.85.046703.
- [50] Alexander, F.J., Chen, S. and Sterling, J.D. Lattice boltzmann thermohydrodynamics. *Phys. Rev. E*, 47: R2249–R2252, Apr 1993. doi: 10.1103/PhysRevE.47.R2249.
- [51] Chakraborty, S. and Chatterjee, D. An enthalpy-based hybrid lattice-Boltzmann method for modelling solid-liquid phase transition in the presence of convective transport. *Journal of Fluid Mechanics*, 592: 155–175, 2007. doi: 10.1017/S0022112007008555.

- [52] Winden, van J.H.S. Developing a hybrid lattice boltzmann finite difference mode for phase change in the molten salt reactor. Master's thesis, Delft University of Technology, 2021.
- [53] Eggels, J.G.M. and Somers, J.A. Numerical simulation of free convective flow using the lattice-Boltzmann scheme. *International Journal of Heat and Fluid Flow*, 16(5):357–364, 1995. ISSN 0142727X. doi: 10.1016/0142-727X(95)00052-R.
- [54] Chatterjee, D. Lattice Boltzmann simulation of incompressible transport phenomena in macroscopic solidification processes. *Numerical Heat Transfer, Part B: Fundamentals*, 58(1):55–72, 2010. doi: 10.1080/10407790.2010.508439.
- [55] Cook, B.K., Noble, D.R. and Williams, J.R. A direct simulation method for particle-fluid systems. *Engineering Computations (Swansea, Wales)*, 21(2-4):151–168, 2004. ISSN 02644401. doi: 10.1108/02644400410519721.
- [56] Zhao, P. et al. Modeling the mushy zone during the melting process under Neumann boundary condition using the improved enthalpy-porosity method. *Numerical Heat Transfer; Part A: Applications*, 78(8):423–442, 2020. ISSN 15210634. doi: 10.1080/10407782.2020.1793540. URL <https://doi.org/10.1080/10407782.2020.1793540>.
- [57] Ziskind, G. Modeling of heat transfer in phase change materials for thermal energy storage systems. In Luisa F Cabeza, editor, *Advances in Thermal Energy Storage Systems (Second Edition)*, Woodhead Publishing Series in Energy, chapter 12, pages 359–379. Woodhead Publishing, second edition edition, 2021. ISBN 978-0-12-819885-8. doi: <https://doi.org/10.1016/B978-0-12-819885-8.00012-7>.
- [58] Zhang, T. et al. General bounce-back scheme for concentration boundary condition in the lattice-Boltzmann method. *Physical Review E - Statistical, Nonlinear, and Soft Matter Physics*, 85(1):1–14, 2012. ISSN 15393755. doi: 10.1103/PhysRevE.85.016701.
- [59] Sohankar, A., Norberg, C. and Davidson, L. Low-Reynolds-number flow around a square cylinder at incidence: Study of blockage, onset of vortex shedding and outlet boundary condition. *International Journal for Numerical Methods in Fluids*, 26(1):39–56, 1998. ISSN 02712091.
- [60] Lou, Q., Guo, Z. and Shi, B. Evaluation of outflow boundary conditions for two-phase lattice Boltzmann equation. *Physical Review E - Statistical, Nonlinear, and Soft Matter Physics*, 87(6):1–16, 2013. ISSN 15393755. doi: 10.1103/PhysRevE.87.063301.
- [61] Rohde, M. et al. A generic, mass conservative local grid refinement technique for lattice-Boltzmann schemes. *International Journal for Numerical Methods in Fluids*, 51(4):439–468, jun 2006. ISSN 0271-2091. doi: 10.1002/fld.1140.
- [62] Yuan, H.Z., Wang, Y. and Shu, C. An adaptive mesh refinement-multiphase lattice Boltzmann flux solver for simulation of complex binary fluid flows. *Physics of Fluids*, 29(12), 2017. ISSN 10897666. doi: 10.1063/1.5007232. URL <http://dx.doi.org/10.1063/1.5007232>.
- [63] Tosun, I. Evaluation of transfer coefficients: Engineering correlations. In Ismail Tosun, editor, *Modeling in Transport Phenomena (Second Edition)*, pages 59–115. Elsevier Science B.V., Amsterdam, second edition edition, 2007. ISBN 978-0-444-53021-9. doi: <https://doi.org/10.1016/B978-044453021-9/50005-1>.
- [64] A parallel plate heat exchanger with isothermal surfaces. <http://www.cchem.berkeley.edu/cbe150a/Parallel%20Plate%20Heat%20Transfer.pdf>, n.d. Berkeley University of California.
- [65] Chang, M.W. and Finlayson, B.A. On the proper boundary conditions for the thermal entry problem. *International Journal for Numerical Methods in Engineering*, 15(6):935–942, 1980.
- [66] Kuan-Cheng, C., Ouazzani, J. and Rosenberger, F. Mixed convection between horizontal plates-ii. fully developed flow. *International Journal of Heat and Mass Transfer*, 30:1655–1662, 1987. doi: 10.1016/0017-9310(87)90311-5.
- [67] Shah, R.K. and London, A.L. *Laminar flow forced convection in ducts. Advances in heat transfer*. Academic press, 1978.

- [68] Weigand, B. and Ruß, G. The freeze-shut of a convectively cooled parallel plate channel subjected to laminar internal liquid flow. *Wärme- und Stoffübertragung*, 28(1-2):17–25, 1993. ISSN 00429929. doi: 10.1007/BF01579617.
- [69] Bale, C.W., et al. FactSage Thermochemical Software and Databases - 2010 - 2016. *Chalphad*, 54:35–53, 2016. URL [www.factsage.com](http://www.factsage.com).
- [70] Niezgodna-Zelasko, B. Heat transfer of ice slurry flows in tubes. *International Journal of Refrigeration*, 29(3):437–450, 2006. ISSN 01407007. doi: 10.1016/j.ijrefrig.2005.09.017.
- [71] Dutkowski, K. and Kruzel, M. Experimental Investigation of the Apparent Thermal Conductivity of Microencapsulated Phase-Change-Material Slurry at the Phase-Transition Temperature. *Materials*, 14(15), 2021. ISSN 1996-1944. doi: 10.3390/ma14154124.
- [72] Lozhechnikova, A. Determination of Slurry's Viscosity using Case Based Reasoning Approach. *MSc Thesis*, 2011.
- [73] Niezgodna-Zelasko, B. and Zelasko, J. Melting of ice slurry under forced convection conditions in tubes. *Experimental Thermal and Fluid Science*, 32(8):1597–1608, 2008. ISSN 08941777. doi: 10.1016/j.expthermflusci.2008.05.002.
- [74] Jilte, R. D. et al. Battery thermal management system employing phase change material with cell-to-cell air cooling. *Applied Thermal Engineering*, 161:114199, 2019. ISSN 1359-4311. doi: <https://doi.org/10.1016/j.applthermaleng.2019.114199>.
- [75] Akhtar, S., Ali, H. and Park, C.W. Thermo-Fluidic Characteristics of Two-Phase Ice Slurry Flows Based on Comparative Numerical Methods. *Processes*, 7(12), 2019. doi: 10.3390/pr7120898.
- [76] Das, P. et al. Thermodynamic and Physical Properties of Molten LiF-ThF<sub>4</sub>-UF<sub>4</sub> Salts Mixture. *Journal of Fluorine Chemistry*, 226(May):109349, 2019. ISSN 00221139. doi: 10.1016/j.jfluchem.2019.109349.
- [77] Phapale, S. et al. *Determination of eutectic composition and heat capacities of fuel salt (LiF-ThF<sub>4</sub>-UF<sub>4</sub>) and blanket salt (LiF-ThF<sub>4</sub>) mixtures*. Bhabha Atomic Research Centre, India, 2015.
- [78] Mastromarino, S. *New measurement methods and physico-chemical properties of the MSFR salt*. PhD thesis, Delft University of Technology, 2022.
- [79] Gheribi, A. et al. Prediction of the thermophysical properties of molten salt fast reactor fuel from first-principles. *Molecular Physics*, 2014. doi: 10.1080/00268976.2014.897396.
- [80] Lee, J.S. *Freezing problem in pipe flows*. Ph.d. thesis, Iowa State University, 1993.
- [81] The Engineering Toolbox. Material properties. [https://www.engineeringtoolbox.com/material-properties-t\\_24.html](https://www.engineeringtoolbox.com/material-properties-t_24.html).